COMPUTATIONAL FLUID DYNAMICS OF FLUID TRANSPORT AND DEPOSITION OF PARTICLES UNDER UNSTEADY FLOW IN HUMAN FLUID SYSTEM
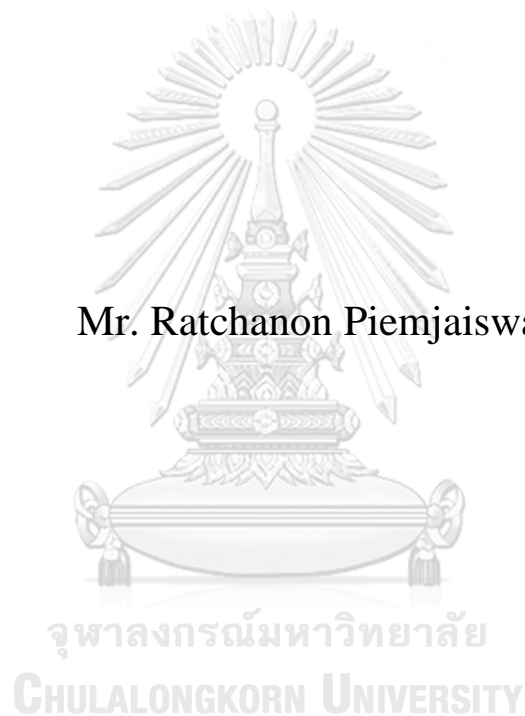
Mr. Ratchanon Piemjaiswang

จุฬาลงกรณ์มหาวิทยาลัย
CHULALONGKORN UNIVERSITY

A Dissertation Submitted in Partial Fulfillment of the Requirements
for the Degree of Doctor of Philosophy in Chemical Technology
Department of Chemical Technology
Faculty of Science
Chulalongkorn University
Academic Year 2018
Copyright of Chulalongkorn University

พลศาสตร์ของไหลเชิงคำนวณของการขนส่งของไหลและการพอกพูนของอนุภาคภายใต้การไหล
แบบไม่คงตัวภายในระบบของไหลของมนุษย์

นายรัชชานนท์ เปี่ยมใจสว่าง

วิทยานิพนธ์นี้เป็นส่วนหนึ่งของการศึกษาตามหลักสูตรปริญญาวิทยาศาสตรดุษฎีบัณฑิต
สาขาวิชาเคมีเทคนิค ภาควิชาเคมีเทคนิค
คณะวิทยาศาสตร์ จุฬาลงกรณ์มหาวิทยาลัย
ปีการศึกษา 2561

Thesis Title	COMPUTATIONAL FLUID DYNAMICS OF FLUID TRANSPORT AND DEPOSITION OF PARTICLES UNDER UNSTEADY FLOW IN HUMAN FLUID SYSTEM
By	Mr. Ratchanon Piemjaiswang
Field of Study	Chemical Technology
Thesis Advisor	Associate Professor BENJAPON CHALERMSINSUWAN, Ph.D.
Thesis Co Advisor	Professor PORNPOTE PIUMSOMBOON, Ph.D.
	Associate Professor Shuichi Shiratori, Ph.D.

Accepted by the Faculty of Science, Chulalongkorn University in Partial Fulfillment of the Requirement for the Doctor of Philosophy

.... Dean of the Faculty of Science
(Professor POLKIT SANGVANICH, Ph.D.)

DISSERTATION COMMITTEE

.... Chairman
(Associate Professor PRASERT REUBROYCHAROEN, Ph.D.)

.... Thesis Advisor
(Associate Professor BENJAPON CHALERMSINSUWAN, Ph.D.)

.... Thesis Co-Advisor
(Professor PORNPOTE PIUMSOMBOON, Ph.D.)

.... Thesis Co-Advisor
(Associate Professor Shuichi Shiratori, Ph.D.)

.... Examiner
(Professor Somkiat Ngamprasertsith, Ph.D.)

.... Examiner
(Professor SUTHILUK PATUMRAJ, Ph.D.)

.... External Examiner
(Associate Professor Terdthai Vatanatham, Ph.D.)

รัชชานนท์ เปี่ยมใจสว่าง : พลศาสตร์ของไหลเชิงคำนวณของการขนส่งของไหลและการพอกพูนของอนุภาค ภายใต้การไหลแบบไม่คงตัวภายในระบบของไหลของมนุษย์. (COMPUTATIONAL FLUID DYNAMICS OF FLUID TRANSPORT AND DEPOSITION OF PARTICLES UNDER UNSTEADY FLOW IN HUMAN FLUID SYSTEM) อ.ที่ปรึกษาหลัก : รศ. ดร.เบญจพล เฉลิมสินสุวรรณ, อ.ที่ปรึกษาร่วม : ศ. ดร.พรพจน์ เปี่ยม สมบูรณ์,รศ. ดร.ชูอิจิ ชิระโทริ

พลศาสตร์ของไหลเชิงคำนวณเป็นวิธีการทางคณิตศาสตร์ที่นิยมใช้ศึกษาพฤติกรรมการไหลของของไหล และมีการ ประยุกต์ใช้งานในหลายด้าน งานวิจัยนี้เป็นการประยุกต์ใช้พลศาสตร์ของไหลเชิงคำนวณการงานวิจัยทางด้านชีวการแพทย์ ซึ่งแบ่งงานวิจัย ออกเป็นสองส่วน ได้แก่ การศึกษาการเกาะติดของอนุภาคภายในระบบทางเดินหายใจ และการศึกษาการเกาะติดและการขนส่งอนุภาค ชีวเคมีภายในระบบหมุนเวียนโลหิต การศึกษาแบบจำลองพลศาสตร์ของไหลภายในระบบทางเดินหายใจทำการควบรวมแบบจำลองไฟฟ้า สถิต เพื่อนำมาใช้ศึกษาอิทธิพลของความถี่ในการหายใจต่อการเกาะติดของอนุภาคภายในหลอดลม และทำนายตำแหน่งการเกาะติดของ อนุภาค ผลการศึกษาสามารถช่วยให้การพัฒนาละอองยามีประสิทธิภาพมากขึ้น นอกจากนี้ยังมีการศึกษาคุณสมบัติและสัญฐานวิทยาของ ละอองยาที่มีผลต่อการเกาะติดเพื่อเป็นแนวทางในการออกแบบยาให้จำเพาะกับผู้ป่วยมากขึ้น

แบบจำลองทางคณิตศาสตร์ของปฏิกิริยาชีวเคมีได้ถูกพัฒนาเพื่อใช้ในการทำนายรูปแบบการสะสมของอนุภาคชีวเคมีของการ เกิดภาวะหลอดเลือดแข็ง งานวิจัยได้นำเสนอแบบจำลองแบบสามส่วน (Three-zone artery model) สำหรับการศึกษาการขนส่ง อนุภาคชีวเคมีภายในผนังหลอดเลือดซึ่งสามารถทำนายการเกิดภาวะหลอดเลือดแข็งได้ นอกจากนี้ทำการวิเคราะห์สมบัติของเลือดด้วยวิธี ทางสถิติ เพื่อหาปัจจัยที่ส่งผลการสะสมของชีวเคมีที่ผนังหลอดเลือด ผลการศึกษาสามารถใช้เป็นแนวทางในการช่วยเหลือแพทย์ในการ วินิจฉัยและทำนายการเกิดภาวะหลอดเลือดแข็งต่อไปในอนาคต

สาขาวิชา	เคมีเทคนิค	ลายมือชื่อนิสิต ....
ปีการศึกษา	2561	ลายมือชื่อ อ.ที่ปรึกษาหลัก ....
		ลายมือชื่อ อ.ที่ปรึกษาร่วม ....
		ลายมือชื่อ อ.ที่ปรึกษาร่วม ....

5972836423 : MAJOR CHEMICAL TECHNOLOGY
KEYWORD:　　CFD, atherosclerosis, human airway, circulating system, respiratory system, lesion growth

Ratchanon Piemjaiswang : COMPUTATIONAL FLUID DYNAMICS OF FLUID TRANSPORT AND DEPOSITION OF PARTICLES UNDER UNSTEADY FLOW IN HUMAN FLUID SYSTEM. Advisor: Assoc. Prof. BENJAPON CHALERMSINSUWAN, Ph.D. Co-advisor: Prof. PORNPOTE PIUMSOMBOON, Ph.D.,Assoc. Prof. Shuichi Shiratori, Ph.D.

Computational fluid dynamics has been widely used to investigate flow phenomena in many different applications. This study focuses on the development of computational fluid dynamic model in biomedical applications, including the flow within human respiratory system and the flow within human circulating system. For the model of respiratory system, electrostatic charge model was coupled, and the effect of breathing frequency was investigated. The accomplishment of the study will gain better understanding of the hydrodynamics when applying the electrostatic field, and will use to identify the potential aerosol deposition location. The aerosol properties and morphologies were also considered their effect on the hydrodynamics of the particles. This will be a guideline for the pharmacist to design a specific type of aerosol for the patient.

The mathematical models for biochemical interaction were implemented for the study of early stage atherosclerotic lesion growth. The three-zone artery model was proposed as a framework for species transport in arterial wall. The species concentration inside the intima layer was examined as a sign of the early stage development of the plaque. The results showed compromise locations where the accumulation of the plaque occurs. The flow parameters were investigated statistically to identify the significant factors affecting the species concentration. The benefit of the study will yield the better understanding of the dominant factors controlling atherosclerosis growth, which then helps the physicians or technicians to deal more efficient future applications of the precision medicine.

จุฬาลงกรณ์มหาวิทยาลัย
CHULALONGKORN UNIVERSITY

Field of Study:	Chemical Technology	Student's Signature ....
Academic Year:	2018	Advisor's Signature ....
		Co-advisor's Signature ....
		Co-advisor's Signature ....

ACKNOWLEDGEMENTS

TABLE OF CONTENTS

จุฬาลงกรณ์มหาวิทยาลัย

CHULALONGKORN UNIVERSITY

LIST OF FIGURES

LIST OF TABLES

NOMENCLATURES

A	Area
B	Magnetic flux density
Cf	Skin friction coefficient
D	Electric displacement vector
E	Electric field
F	Force acting on the particle under magnetic field
$F_{qs\alpha}$	Electrostatic force
f	Breathing frequency
g	Gravitational acceleration
I	Unit tensor
k_s	Granular conductivity
n_i	Normal vector
OI	Oscillatory index
OSI	Oscillatory shear index
$OVFI$	Oscillatory velocity flow index
P	Induced polarization
P_s	Granular pressure
p	Pressure
Q	Flow rate
q	Electric charge
T	Assessment time
t	Time
u	Flow velocity along the wall
v	Velocity
v_g	Gas velocity
v_{ref}	Reference velocity

v_s Solid velocity

v '   Fluctuation velocity

WSS   Wall shear stress

Greek symbol

β_{gs} Drag force

χ_e Electric susceptibility

ϵ_0 Permittivity of vacuum

ϵ_m Permittivity of material

ε_g Gas volume fraction

ε_s Solid volume fraction

φ Scalar variable

γ Collisional energy dissipation

μ Dynamic viscosity

θ Granular temperature

ρ_c Charge density

ρ_g Gas density

ρ_{ref} Reference density

ρ_s Solid density

τ_g Gas stress tensor

τ_s Solid stress tensor

τ_w Wall shear stress

CHAPTER I
INTRODUCTION

Background

Fluid dynamics is the study of fluid motion to describe wide range quantities of fluid movement. It can be used in many applications, including calculation of forces and momentums on aircraft, determining the force or pressure drop through pipeline, or predicting flow behavior within human respiratory system. Nowadays, advance computing technology has been developed to handle millions of processing requests. Computational fluid dynamics (CFD) is rapidly becoming popular as the flow analysis technique involving fluid flow, heat transfer and mass transfer. CFD uses numerical analysis to solve, analyze and visualize the phenomena associated with the flow of fluid based on governing equations including conservation of momentum, conservation of mass, and conservation of energy. This technique is powerful which especially uses in industrial environments. There are several unique advantages of CFD in fluid system design such as the reduction of times and costs for the new design, and the ability to study the system under difficult or impossible environment to perform. By adding additional mathematical models, CFD can solve and predict realistic hydrodynamic behavior with more precise situations such as pulsation of the flow, and turbulences. This technique is robustly capable of evaluating and predicting the result in many complex scenarios. However, the development of the additional mathematical models to describe the physiological process has not been much involved by researchers.

The manufacturing industry is growing rapidly to serve the demands of human usage. The environmental problem is in much concern by many countries. The air pollution is rising which affects the quality of life and well-being of people around the world. This leads to many chronic diseases, such as asthma, cystic fibrosis, and chronic obstructive pulmonary disease (COPD). The best alternative way to treat these diseases is local therapies. To do a local therapy for these diseases, the inhalation of aerosol drug is introduced. The inhalation of the aerosol drug was designed to allow the use of small doses and to reduce the systemic side effects [1]. The particles or aerosol droplets need to be in sufficient size and mass to allow the inhalation air to carry them along the

airway. The effectiveness of an aerosol drug treatment was depended on how much of the medication will reach the intended location of deposition [2]. The major problem is the deposition of aerosol particles in unwanted region. Today, the development of aerosol drug delivery devices such as inhalers combined with the advancement of pharmaceutical science make it possible to control the initial flow condition with specific size and shape of the aerosols. The shape factor alters the performance characteristics of particles which are depended greatly on particle morphology. It is generally denoted as particle sphericity. To gain better understanding of how the inhaled air flow inside the respiratory tract, the aim of this study is to increase the precision and consistency of aerosol drug delivery by focusing on the development of the flow model with the integration of electrostatic charge to capture the effect of the elementary charge of nanomagnetosol. When the electrostatic charge on the aerosol exceeds its critical value, the electrostatic forces are arising due to the gradient of the electric potential. Since the aerosol particles are so small, the electrostatic forces are much greater than the drag forces. At this point, the aerosols were pushed toward the trachea wall or the center of the airway, depending on the particle charge [3]. With this property, the particles can be guided along the airway to the desired region using external magnetic field. Moreover, the morphology of the aerosol is also affected the flow field. The new design of aerosol drug is aimed to deliver the drug to the destination target as close as possible.

Another advantage of using CFD is to study blood flow within circulatory system. Atherosclerosis is a chronic disease that remains asymptomatic for decades. As the development of the lesions is continuously growing, the arteries enlarge at all plaque locations; therefore, there is no notable effect on blood flow. The signs and symptoms only show up after severe narrowing which obstruct the blood flow to the organ. Without sufficient understanding of the diseases, it is difficult to make an accurate prognosis. Fortunately, the understanding of the atherosclerosis has progressed using computational fluid dynamics. Recently, researchers studied the influence of flow pulsatility on the transport of blood-borne species. The pulsatility is identified to be an influence on the development of atherosclerosis lesion. The atherosclerosis growth model is developed for quickly computing the potential distribution of the lesions. The

oscillatory flow index and oscillatory kinetic energy index are also developed to represent the recirculating of the flow. To make the model more practical, the integration and development of various mathematical models must be made.

This study focuses on the development of computational fluid dynamic model in biomedical applications, including the flow within human respiratory system and the flow within human recirculating system. For the model of respiratory system, electrostatic charge model will be coupled, and the effect of particle shapes will be investigated. The accomplishment of the study will gain better understanding of the hydrodynamics when the electrostatic field was applied. The morphology of the aerosol drug is also considered as it affects the hydrodynamics of the particles. This will be a guideline for the pharmacist to design a specific type of aerosol for the patient.

For the model of blood vessel in the circulatory system, lesion growth model and the biochemical interaction will be coupled with the fluid flow model. It is necessary to predict temporal behaviors of the flow around atherosclerosis site, as well as the resultant stress distribution in the blood vessel. The benefit of the study will yield the better understanding of the dominant factors controlling atherosclerosis growth, which then help the physicians or technicians to deal more efficient with the subsequences for the leap forward of future applications of the precision medicine.

Objectives

1. To develop computation fluid dynamic model for unsteady flow in human fluid system.
2. To study the effect of parameters on fluid behavior and particle deposition location within human respiratory tract.
3. To study the effect of parameters on fluid behavior and atherosclerosis growth location within human blood circulating system.

Scope of dissertation

1. Human respiratory tract was simulated in three-dimensional spaces using computational fluid dynamics model derived from computed tomography scan of the trachea.

2. Human blood circulating system was simulated in three-dimensional spaces using computational fluid dynamics model derived from computed tomography scan of the coronary artery.

3. Parametric study of the flow parameters was investigated using statistical analysis technique.

CHAPTER II
THEORY AND LITERATURE REVIEW

Transport property of fluid

Fluid viscosity (μ)

Viscosity is the quantity of the fluid that measures the resistance to flow expressed by the force acting on the fluid per unit area [4]. To represent the generalized idea of fluid viscosity, Figure 2.1 illustrates the fluid flows in between two infinitely large plates, one is stationary, and one is moving in parallel at constant velocity (v).
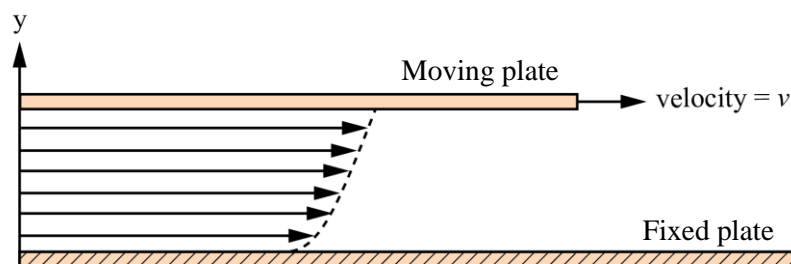
Figure 2.1 *Couette flow*

Let assume that the second plate is moving so slow that it does not cause a turbulence to the flow. It can be observed that each layer of the fluid moves at different velocity (Figure 2.1). Most fluids show that their velocities are not varied linearly from zero to the finite value (v) in accordance with its height from the first plate to the other. This behavior is due to the friction force between each layer resisting their motion.

According to the relation of the fluid viscosity for an incompressible and isotropic fluid, the newton's law of viscosity states that the shearing force per unit area is proportional to the negative of the velocity gradient, expressed by

$$\tau_{yx} = -\mu \frac{dv_x}{dy}$$

where, $\tau_{yx} = \frac{F}{A}$ is the force (F) acting in the x-direction on a unit area (A) normal to the y-direction, or shear stress, μ is flow viscosity, and $\frac{dv_x}{dy}$ is fluid velocity

gradient or rate of shear deformation. The types of fluid according to its viscous property can be classified into two types, the Newtonian fluid and the non-Newtonian fluid [5].

Newtonian

The Newtonian fluid is a fluid which the viscosity tensor is constant which means the strain rate does not depend on the fluid velocity. The Newtonian fluids are the simplest model to describe the fluid viscosity. No fluid is perfectly described by the Newtonian fluid, however many common fluids, such as water and air, can be assumed to be Newtonian in many typical cases of computational fluid dynamics studies. For the first part of this dissertation, the study of the airflow with in human respiratory system, air is also considered as the Newtonian flow.

Non-Newtonian

Unlike Newtonian fluid, the non-Newtonian fluid does not follow the Newton's law of viscosity. The viscosity of the fluid can change under forces as shown in Figure 2.2. The non-Newtonian fluids are mostly found responses to shear rate either more like solid or liquid which are categorized into two groups, dilatant and pseudoplastic. The dilatant fluids appear to increase its viscosity when the shear rate increases. It is so called shear thickening fluid. The common dilation fluids are the suspensions of corn starch in water. Another type, pseudoplastic, is referred as a shear thinning fluid. The pseudoplastic fluids are responded spontaneously with the change of shear rate. The examples of this type of fluids are wall paint, ketchup, blood, etc. The second part of this dissertation is considered the blood as the flow medium. The model describes the behavior of the blood will be expressed in the following section.
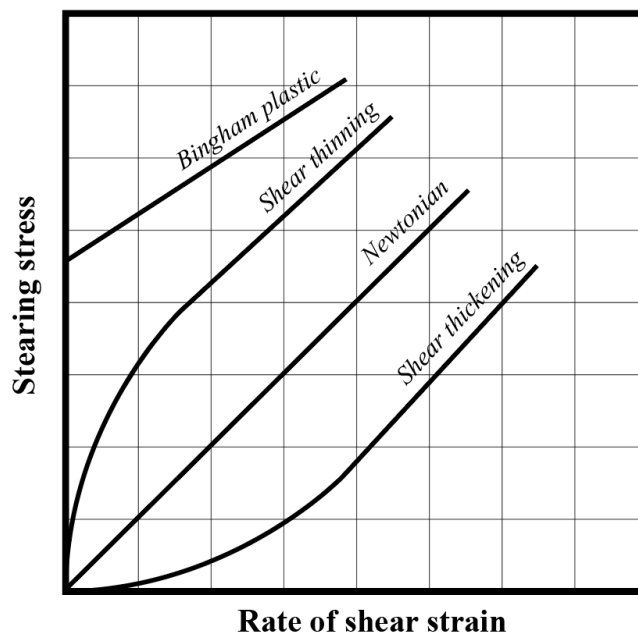
Figure 2.2 *Shearing stress curves for different types of fluid*

The respiratory system

Respiratory tract

The main function of respiratory system is to exchange oxygen gas between the surrounding and the inner body cells. The transportation in and out of the exchange gas are conveyed along the respiratory tract. The respiratory air passages include two functional zones, conductive zone and respiratory zone. The conduction zone consists of multiple parts including mouth, nose, pharynx, larynx, trachea, bronchi, and bronchioles. In this zone, the inhaled air is primarily transported from the atmosphere to the respiratory zone. Next, the respiratory zone is connected at the end of the conduction zone. The primary function of this zone is to exchange oxygen-rich inhaled gas with carbon dioxide. The ending of the respiratory tract is a closed-end which ended at the alveoli sag. The alveoli are the semi-permeability membrane which allow inhaled oxygen to diffuse into the capillaries. This dissertation is mainly focused on the transport of the air and particles in the lower part of the respiratory tract which is the trachea. On average, the total branches of the adult human trachea have 23 branches or generations. From the generation 0 to 16, the trachea simply acts as air conduits to the

downstream. The diameter of the first-generation bronchi is approximately 1.0 to 1.4 centimeters. The diameter of the latter generation is becoming narrower until it reaches 0.06 centimeters at the 16th generation.

Mechanics of breathing

The breathing mechanics involves conchae, epiglottis, trachea, bronchi, and bronchioles. The inhalation process starts with the contraction of the diaphragm which also moves it downward. The intercostal muscles help enlarge the chest cavity. This mechanism increases the space in the chest. The increasing of the chest volume caused the negative pressure, resulting in the air getting sucked in through nose and mouth. The air travels along the trachea into the lungs. Once it reaches the air sacs, the exchange between oxygen and carbon dioxide takes place. The exhalation process is the reverse of the inhalation. The diaphragm relaxes causing itself to move upward. The intercostal muscles are also relaxed. Putting it all together, they reduce the space of the chest cavity. The air gets push out of the lungs then out of the nose and mouth.

Aerosol drug design

The advancement of pharmaceutical technology leads to new method of drug administration. Aerosol drug therapy has been attracted by many researchers as it has many advantages for pulmonary diseases. The aerosol is a solid or liquid suspension in gas which clinically generates with atomizers, nebulizers, or inhalers. It requires lower doses of the drug to work effectively as the drug is targeted directly to the diseased site. This also reduces the risk of unwanted systemic side effects from the excessive drug. The effectiveness of the aerosol drug is depended on many factors such as the flow behavior, aerosol size distribution, or aerosol shape factor.

Particulate matter (PM)

Particulate matter or PM is a fine emission with a combination of different types of particles. It come from various sources such as human activity like coal-fired power plants, road transport, or from natural like pollutant in the atmosphere. These particulate matters can be defined into two groups classified by their

diameter: PM_{10} (coarse particulate matter) and $PM_{2.5}$ (fine particulate matter). The PM_{10} is the inhalable particles with the diameter greater than 10 micrometers and smaller. The $PM_{2.5}$ is finer than PM_{10} which the diameters are generally smaller than 2.5 micrometers. The particulate matters are so small which they can be inhaled by human and can cause serious pulmonary disease such as lung cancer, chronic lung disease, and lung infection. They can penetrate through the lungs and some smaller particles can get into the blood stream.

The cardiovascular system

The cardiovascular system is the blood transport system for the human to deliver nutrients, waste and other substance from and to the cell via blood vessels. The primary organs involving in this system is the blood vessel and heart, which develops rhythmic pressure differential to drive the blood flow. This produces movement of the blood with pulsatile behavior. The cardiovascular system is the closed-loop system which blood never leaves the blood vessel network.

Blood vessel

There are many types of blood vessel which vary in their composition and size. The oxygenated blood was carried in the arteries, and the deoxygenated blood was carried in the veins. The interconnected vessel which joins arteries and veins is called capillaries. Arteries is made-up of soft-tissue which carry blood away from the heart. The one closest to the heart is called aorta. The vessel has the size gradually decrease while it located further away from the heart, referred as arterioles (Illustrated in Figure 2.3). The oxygenated blood then delivers to the tissues via small vessel, referred as capillaries. The vessels which carry the deoxygenated blood back to the heart according to their size are called venules and veins, respectively.
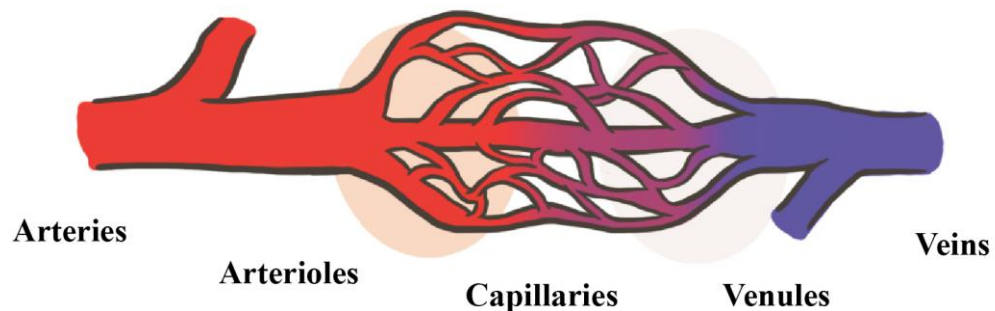
Figure 2.3 *Blood vessel schematics. (Color represents deoxygenation of blood within the vessels)*

There are two circuits of blood flow in the cardiovascular system, the pulmonary and the systemic. The pulmonary circuit carries blood between lungs and heart. The systemic circuit carries blood throughout the body. At first, the oxygenated blood from the lungs is carried along the pulmonary vein into the heart's left atrium. The heart pumps the blood through the aorta and gradually reduce their size onto arteries and arterioles. These vessels then deliver the blood to the organ's tissues which the mass transfer of substances such as oxygen, water, nutrient, and waste is occurred. The exchanged carbon dioxide returns to the heart's right ventricle through venules, veins, respectively. The largest veins connected to the heart referred as vena cava. The heart then pumps the blood into pulmonary artery for the carbon dioxide removal at the lungs.

Fluid composition

Blood is the heterogenous liquid that is transported within the cardiovascular system. Blood is composed of two main components: plasma and formed elements. Plasma, a clear fluid mixture, is mainly made up of water. Proteins, enzymes, lipids and other cellular by-product are held within the plasma. The formed elements are erythrocytes (red blood cells, RBCs), leukocytes (white blood cells, WBCs), and thrombocytes (platelets). These elements are cells except for the thrombocytes which are tiny fragments of cytoplasm from the bone marrow that enter the circulation. Leukocytes are categorized into 2 groups, the granulocytes (neutrophils, eosinophils, and basophils) and agranulocyte (lymphocytes, and monocytes). The erythrocytes make up 45% of the total blood

volume which is denser than plasma and leukocytes. It has a strong effect on the flow rheology which will be described in the constitutive equation.

The arterial anatomy

Blood transport, within the vessel which is a permeable membrane, consists of multiple layers. The inner layer is a hollow cavity where the blood flows is called lumen. The single cell barrier elastic membrane made up of endothelial cell is called endothelium. This layer acts like a first barrier from blood and other substances. The next layer is the tunica intima, commonly called, the intima. It makes the artery elastic which allows the artery to bend along the parts of the body. Next, tunica media, or media, is the elastic tissue made up of smooth muscle cells and collagen. Followed by the adventitia, the external barrier of the artery, this layer protects the artery from its surrounding.

Atherosclerosis

Atherosclerosis is the cardiovascular disease of the arterial wall which causes the blockage of the vessel. The blockage of the vessel is made up of plaque building up inside the artery. Plaque is the substance composed of fat, lipid, calcium, and others. The plaque hardens over time which will limit the oxygenated blood flow to the downstream cells. By lacking the oxygen, this leads to many serious issues including stroke, heart attack, etc. The previous studies also indicate that the disease is often found at the site where the flow has been disturbed such as flow bifurcation and curvature. The strong disturbance flow alters the flow pattern which is reported to be one of the influent factors of the atherosclerosis development.

Computational fluid dynamics

Computational fluid dynamics or CFD is one of the techniques that uses numerical analysis to solve fluid flow problems. It is a branch of fluid mechanics which helps researchers to have a better understanding of the flow phenomena using mathematics and computer science. The approach of the CFD based on the conservation law including conservation of momentum, mass, and energy. The additional equations can also be added into the calculation model for better representing of the problem. The

computation requires high-speed computer in order to perform the calculation on the complex problems. CFD can be applied to a wide range of problems such as industrial engineering, environmental engineering, chemical engineering, biomedical engineering, etc. The first stage of the technique is to convert the partial differential equations of the model into a set of algebraic equations. The second stage of the simulation requires an implementation of the discretized equations into an appropriated numerical solver. The step-by-step methodology of the CFD can be simply expressed as:

- The geometry of the problem is defined as a fluid volume using computer aided design software (CAD)

- The geometry then is divided into small control volume cells called mesh, or grid, this mesh will represent as a computational cell that stores information based on its space continuum. The mesh may divide uniformly or non-uniformly with a various combinations of mesh types, which are pyramidal, tetrahedral, or hexahedral.

- Once the mesh is generated, the physical models, including conservation of heat, mass, and momentum, species, and scalar transport, are specified. Then, the mathematical models are discretized numerically to become a simpler set of linear equations which are ready to solve in a high-speed computer.

- The solver needs boundary conditions at all bounded surface of fluid domain, for instance: inlet, outlet, wall, etc. in order to complete the calculation. For unsteady state calculation, the initial conditions of the fluid flow are also required.

- The discretized equations are iteratively solved with appropriate solver to obtain the results.

- The numerical result is post-processed to display in various type of presentation such as contour plot, XY plot, volume rendering plot, etc.

There are many major methods to discretize the governing equations such as finite difference method, finite volume method (FVM), and finite element method (FEM). The commonly used method for fluid dynamics analysis is finite volume method. In FVM, the discretized equations are computed on a meshed geometry. The word "volume" refers to a control volume which is a small volume containing a node point

on the mesh. The equations are assessed as fluxes entering and exiting each control volume on the basis that the flux in-and-out must be conserved.

In the next section, the detailed mathematical models using in this dissertation is defined and explained in detail.

Multiphase flow model

Multiphase flow is the flow with multiple fluids. The fluid phases can be different chemical species, such as air-aerosol particle, or represent different thermodynamic phases of the same species, such as steam-water. In multiphase flow, fluids are assumed to be mixed in a large-scale length, for example, the gas bubble in water steam, or the sand and air in a fluidized bed system. In these cases, it is necessary to solve the velocity, temperature, etc. individually for each phase. These fluids may interact or exchange phase with each other in the form of interfacial forces or heat and mass transfers.

Two distinct multiphase flow models are commonly used in computational fluid dynamics, Eulerian-Eulerian multiphase model (Euler-Euler) and Lagrangian multiphase flow model. The Euler-Euler approach treats each phase as interpenetrating continua by introducing volume fraction to the conservation equations. The volume fraction is assumed to be continuous functions of the space and time. Then, the equations are solved together to obtain the flow results. For the granular cases, the properties of fluid are obtained from kinetic theory of granular. On the other hand, the Lagrangian approach solves the fluid phase as a continuum just like Euler approach but the dispersed phase or the particle is solved by tracking them individually through the flow field to get their trajectories in specified intervals. As the volume fraction is not being used in the conservation equation of the fluid phase, the Lagrangian approach is limited to only small particle volume fraction. The advantages and disadvantages for both approaches are shown in Table 2.1

Table 2.1 *Multiphase model comparison*

Euler-Euler Approach	
Advantages	**Disadvantages**
Suitable for wide range of volume fraction	Limit knowledge of diffusion coefficient
Relatively cheaper for one additional set of equations	Lower accuracy for particle diameter in phase change application
Turbulence normally included	
Lagrangian Approach (Lagrangian Particle Tracking)	
Advantages	**Disadvantages**
Able to capture behavior and residence time of individual particles	Computational expensive regarding the number of tracked particles
Cheaper computational resources of wide range of particle sizes	Limited to low particle volume fraction
Better heat and mass transfer details	

Mathematical modeling

The principle of solving CFD problem is referred to Navier-Strokes equations which describe the motion of viscous fluid. The physical properties of the fluid are represented by mathematical equations. The fluid, including liquid and gas, has many major properties that define its characteristic, for instance, density, viscosity.

Continuity equation

The continuity equation defines the rate of mass entering and leaving the control volume. The differential form can be written as

$$\frac{\partial \rho}{\partial t} + \nabla \cdot (\rho v) = S_m \qquad (2.1)$$

where ρ is fluid density (kg/m³), t is time (s), v is fluid velocity (m/s), and S_m is a mass source added to the phase. For the 2D axisymmetric geometries, the continuity equation is given by

$$\frac{\partial \rho}{\partial t} + \frac{\partial}{\partial x}(\rho v_x) + \frac{\partial}{\partial r}(\rho v_r) + \frac{\rho v_r}{r} = S_m \qquad (2.2)$$

where x is the axial coordinate (m), r is the radial coordinate (m), v_x is the velocity in axial direction, and v_r is the velocity in radial direction.

The continuity equations for multiphases are given as

$$\frac{\partial}{\partial t}\left(\varepsilon_g\rho_g\right) + \nabla \cdot \left(\varepsilon_g\rho_g v_g\right) = \sum_{p=1}^{n}\left(\dot{m}_{sg} - \dot{m}_{gs}\right) + S_{mg} \quad (2.3)$$

$$\frac{\partial}{\partial t}\left(\varepsilon_s\rho_s\right) + \nabla \cdot \left(\varepsilon_s\rho_s v_s\right) = \sum_{p=1}^{n}\left(\dot{m}_{gs} - \dot{m}_{sg}\right) + S_{ms} \quad (2.4)$$

Where subscribe g and s represents the gas phase and solid phase, respectively. $\dot{m}_{sg}$ is the mass transfer from solid phase to gas phase, $\dot{m}_{gs}$ is the mass transfer from gas phase to solid phase, and ε is the volume fraction of the corresponded phase.

Momentum conservation equation

The momentum conservation equation is described by:

$$\frac{\partial}{\partial t}(\rho\vec{v}) + \nabla \cdot (\rho\vec{v}\vec{v}) = -\nabla p + \nabla \cdot (\bar{\bar{\tau}}) + \rho\vec{g} + \vec{F} \quad (2.5)$$

$$\bar{\bar{\tau}} = \mu[(\nabla\vec{v} + \nabla\vec{v}^T) - \frac{2}{3}\nabla \cdot \vec{v}I] \quad (2.6)$$

Where p is the pressure (kg/m-s), $\bar{\bar{\tau}}$ is the stress tensor, g is acceleration of gravity (m^2/s), F is the external force action on the control volume, μ is viscosity, v is the fluid velocity, and I is the unit tensor.

For the 2D axisymmetric geometries, the equations are given by

$$\frac{\partial}{\partial t}(\rho v_x) + \frac{1}{r}\frac{\partial}{\partial x}(r\rho v_x v_x) + \frac{1}{r}\frac{\partial}{\partial r}(r\rho v_r v_x) =$$

$$-\frac{\partial p}{\partial x} + \frac{1}{r}\frac{\partial}{\partial x}\left[r\mu\left(2\frac{\partial v_x}{\partial x} - \frac{2}{3}(\nabla \cdot \vec{v})\right)\right] + \frac{1}{r}\frac{\partial}{\partial r}\left[r\mu\left(\frac{\partial v_x}{\partial r} + \frac{\partial v_r}{\partial x}\right)\right] + F_x \quad (2.7)$$

$$\frac{\partial}{\partial t}(\rho v_r) + \frac{1}{r}\frac{\partial}{\partial x}(r\rho v_x v_r) + \frac{1}{r}\frac{\partial}{\partial r}(r\rho v_r v_r) =$$

$$-\frac{\partial p}{\partial r} + \frac{1}{r}\frac{\partial}{\partial x}\left[r\mu\left(\frac{\partial v_r}{\partial x} - \frac{\partial v_x}{\partial r}\right)\right] + \frac{1}{r}\frac{\partial}{\partial r}\left[r\mu\left(2\frac{\partial v_r}{\partial r} - \frac{2}{3}(\nabla \cdot \vec{v})\right)\right] - 2\mu\frac{v_r}{r^2} +$$

$$\frac{2}{3}\frac{\mu}{r}(\nabla \cdot \vec{v}) + \rho\frac{v_z^2}{r} + F_r \quad (2.8)$$

$$\nabla \cdot \vec{v} = \frac{\partial v_x}{\partial x} + \frac{\partial v_r}{\partial r} + \frac{v_r}{r} \quad (2.9)$$

where v_z is the swirl velocity.

The momentum equations for multiphases are given as

$$\frac{\partial}{\partial t}\left(\varepsilon_g\rho_g v_g\right) + \nabla \cdot \left(\varepsilon_g\rho_g v_g v_g\right) =$$

$$-\varepsilon_g\nabla p + \nabla \cdot \tau_g + \varepsilon_g\rho_g g + \sum_{s=1}^{n}\beta_{gs}(v_g - v_s) \quad (2.10)$$

$$\frac{\partial}{\partial t}(\varepsilon_s\rho_s v_s) + \nabla \cdot (\varepsilon_s\rho_s v_s v_s) =$$

$$-\varepsilon_s\nabla p + \nabla P_s + \nabla \cdot \tau_s + \varepsilon_s\rho_s g + \sum_{s=1}^{n}\beta_{gs}(v_g - v_s) + F_{qs\alpha} \quad (2.11)$$

$$\bar{\bar{\tau}} = \varepsilon\mu(\nabla\vec{v} + \nabla\vec{v}^T) + \varepsilon(\lambda - \frac{2}{3}\mu)\nabla \cdot \vec{v}I$$

β_{gs} is the gas-solid exchange coefficient. The subscript "s" and "g" are represented the solid and gas phase, respectively. v_s and v_g are the respective velocity vector field. P_s is the solid pressure, and ε is the volume fraction, and λ is the bulk viscosity of corresponded phase.

Fluctuation kinetic energy conservation equation

$$\frac{3}{2}\left[\frac{\partial}{\partial t}(\varepsilon_s\rho_s\theta_s) + \nabla \cdot (\varepsilon_s\rho_s v_s\theta_s)\right] =$$

$$(-p_sI + \tau_s) \cdot \nabla v_s + \nabla \cdot (K_s\nabla\theta_s) - \gamma_s + \phi_{gs} \quad (2.12)$$

$$\theta_s = \frac{1}{3}v_s v_s \quad (2.13)$$

where, I is the solid stress identity tensor (-)

            θ_s is the fluctuation kinetic energy (m^2/s^2)

            K_s is the diffusion coefficient (kg/m-s)

            γ_s is the collision dissipation of energy (kg/m-s^3)

Restitution coefficients

Restitution coefficient (COR or ε) describes the action of the particles when they collide to the wall (Figure 2.4). It defines as the fraction of final velocity to the initial velocity. The coefficient is related to the kinetic energy. Normally, the coefficient is in between 0 to 1 which almost always less than 1 as the kinetic energy is being dissipated due to rotational kinetic energy, plastic deformation, and heat. Physically, the value of 1 describes an elastic collision, while values less than 1 describe an inelastic collision. A perfectly inelastic collision has a coefficient of 0.

$$\varepsilon = \sqrt{\frac{KE_{after\ collision}}{KE_{before\ collision}}} \qquad (2.14)$$

$$\varepsilon = \frac{u_{after\ collision}}{u_{before\ collision}} \qquad (2.15)$$

where, $KE = \frac{1}{2}mu^2$ is the kinetic energy, and u is the particle velocity.

Perpendicular Restitution Coefficient = 0.5
Parallel Restitution Coefficient = 0.75
Impact Angle in Radians = $\emptyset$

Wall Normal

9.2 m/s

4.6 m/s

$\emptyset$

12.8 m/s   9.6 m/s
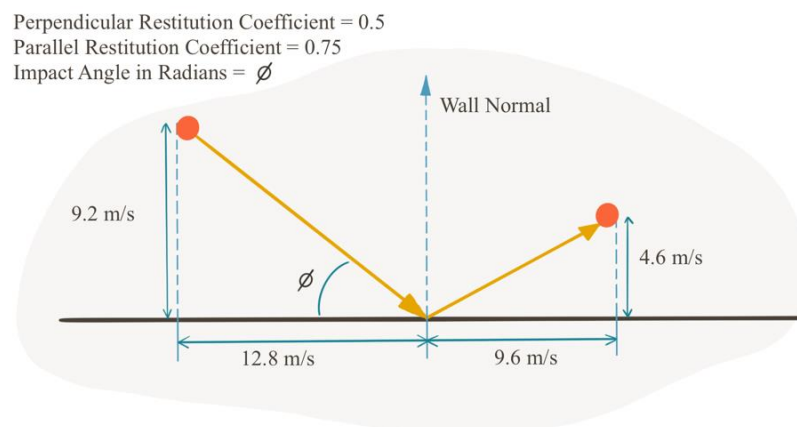
Figure 2.4 *Particle behavior at a wall* [6]

Specie scalars

The general form of scalar transport is

$$\frac{\partial \rho \phi_k}{\partial t} + \frac{\partial}{\partial x_i}\left(\rho u_i \phi_k - \Gamma_k \frac{\partial \phi_k}{\partial x_i}\right) = S_{\phi_k} \text{ and k = 1,...,N} \qquad (2.16)$$

where ϕ_k is a general scalar variable, Γ_k is the diffusion coefficient for each scalar equation, and S_{ϕ_k} is the specie sources.

Shear-thinning blood rheology

Shear-thinning rheology is the behavior of the fluid which its viscosity is depended on its shear rate. The model with best representing the blood is called Carreau's model which is expressed by

$$\mu(\dot{\gamma}) = \mu_\infty + (\mu_o - \mu_\infty)(1 + (\lambda\dot{\gamma})^2)^{\frac{n-1}{2}} \qquad (2.17)$$

where, μ_o is the zero shear rate viscosity (Pa.s)

μ_∞ is the infinite shear rate viscosity (Pa.s)

λ is the relaxation time (s)

$\dot{\gamma}$ is the shear rate (1/s)

Figure 2.5 shows the plot of viscosity when strain rate is varied. The model is a combination of power-law fluid and Newtonian fluid. The fluid behaves like a Newtonian fluid when the shear rate is low ($\dot{\gamma} < 1/\lambda$) while at the intermediate shear rate ($\dot{\gamma} > 1/\lambda$), the fluid behaves like a power-law fluid.
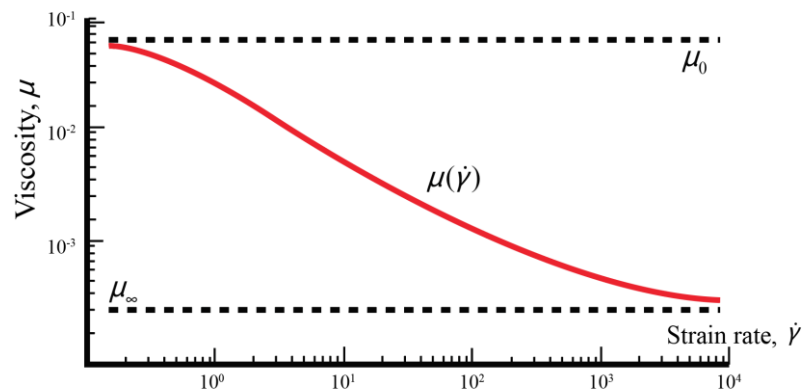
Figure 2.5 *Shear-thinning rheology*

Electrostatic model

Electrostatic model is derived from the Maxwell's electrostatic equations which are composed of four equations including Gauss's law of electric field, Gauss's law of magnetic field, Faraday's law of induction, and Ampere's law. These equations then combine with Lorentz force equation to yield the force acting on a charge under magnetic field. The Lorentz force equation can be expressed as

$$F = q(E + v \times B) \tag{2.18}$$

where,   F   is the force acting on the charge (N)

q   is the electrostatic charge (C, coulomb)

E   is the electric field (N/C)

v is the charge velocity (m/s)

B   is the magnetic flux density (A/m)

From the equation, there are two terms including the force due to the electric field $\left(F_q = qE\right)$ and force due to the magnetic field ($F_q = q(v \times B)$). The force due to the magnetic field can be neglected as the velocity of the charge is so small comparing with the speed of light

especially in the biomedical application of this study. The term of Lorentz force equation is reduced to $F = qE$.

The derivative form of Gauss's law can be expressed as

$$\nabla \cdot D = \rho \tag{2.19}$$

where D is the electric displacement vector, and ρ is charge density. The relation between electric displacement and the electric field can be expressed as

$$D = \epsilon_0 E + P \tag{2.20}$$

where P is the induced polarization, and ϵ_0 is the permittivity of a vacuum. The constitutive relation described the induced polarization and the isotropic electric field can be expressed as

$$P = \epsilon_0 \chi_e E \tag{2.21}$$

where χ_e is the electric susceptibility and $1 + \chi_e$ is the relative permittivity, so the electric field equation can be derived in the form of charge density when $\epsilon_m = 1 + \chi_e$ as

$$\nabla \cdot \epsilon_m \epsilon_0 E = \rho \tag{2.22}$$

The relative electric field equation as a function of solid volume fraction were fitted from the experimental data of Looyenga, Bottcher, and Bordewijk [7] as shown in Eq. 2.23

$$\epsilon_m = 0.97 + 1.20\varepsilon_s = \varepsilon_g \left(\frac{2.17}{\varepsilon_g} - 1.20 \right) \tag{2.23}$$

Where ε_s is volume fraction of solid phase, and ε_g is volume fraction of gas phase. Then, the value of ϵ_m can be obtained from substituting ε_g and charge density. The charge density can be obtained from

$$\rho = \sum_{\alpha=1}^{N} q_{s\alpha} \varepsilon_{s\alpha} \tag{2.24}$$

where $q_{s\alpha}$ is the charge per unit volume of the αth solid phase and $\varepsilon_{s\alpha}$ is the volume fraction of αth solid phase. From all the equations above, the electric field of charge can be derived as

$$\nabla \cdot \left(\varepsilon_g \left(\frac{2.17}{\varepsilon_g} - 1.20 \right) E \right) = \frac{\sum_{\alpha=1}^{N} q_{s\alpha} \varepsilon_{s\alpha}}{\epsilon_0} \tag{2.25}$$

Substituting Poisson's equation $E = -\nabla \varphi$

$$\nabla \cdot \left(\varepsilon_g \left(\frac{2.17}{\varepsilon_g} - 1.20 \right) \nabla \varphi \right) = -\frac{\sum_{\alpha=1}^{N} q_{s\alpha} \varepsilon_{s\alpha}}{\epsilon_0} \tag{2.26}$$

The Poisson's equation is implemented into computational fluid dynamics model by coupled with the gas volume fraction (ε_g) in each calculation time step. The equation yields the change of the electric potential which will be used to achieve the force acting on each of the solid phase ($F_{qs\alpha}$).

$$F_{qs\alpha} = -q_{s\alpha}\varepsilon_{s\alpha}\nabla\varphi \tag{2.27}$$

Reynolds period-averaging

The fluctuation in small-scale occurred in the pulsatile flow system might not be practicable to interpret the results. The conventional smoothing method, Reynolds period-averaging, is introduced to describe the average state of the results. The decomposition of the arbitrary scalar variable (φ) can be defined as

$$\varphi(x,t) = \{\bar{\varphi}(x) + \varphi'(x,t)\} \tag{2.28}$$

The instantaneous scalar variable ($\varphi(x,t)$) can be decomposed into two terms. The $\bar{\varphi}(x)$ term is a period-average of the scalar which defines as

$$\bar{\varphi}(x) = \frac{1}{T}\int_T \varphi(x,t)\,dt \tag{2.29}$$

where the T is the considered flow period. The $\varphi'(x,t)$ term is the deviation of the flow scalar.

By applying the general form to the specie concentration (c_i), the decomposed form can be defined such that

$$c_i(x,t) = \bar{c}_i(x) + c_i'(x,t) \tag{2.30}$$

The period-average is useful to extract relevant data in order to distinguish the time-dependent scalar variable from its steady-state equivalence.

Particle sphericity

Particle sphericity is the measurement of the particle shape on how closely it is comparing with perfect sphere. Mathematically, it is the ratio of the surface area of a sphere to the surface area of the particle.

$$\Psi = \frac{\pi^{\frac{1}{3}}(6V_p)^{\frac{2}{3}}}{A_p} \tag{2.31}$$

$$A_p = \frac{\pi d^2}{4} \tag{2.32}$$

$$V_p = \frac{\pi d^3}{6} \tag{2.33}$$

where V_p is the volume of the aerosol particle, A_p is the surface area of the particle, and d is the mean diameter.

Drag model

Drag model is the set of equations which gives information about the momentum exchange between phases in multiphase simulation, such as between the gas-solid phases and/or solid-solid phases. In this study, two drags model are used to describe the behavior of the momentum exchange. The first model is Energy-minimization multi-scale model (EMMS) which is suitable for the multiphases flow with the cluster of particles. The model was developed based on the work of Li [8]. The second model for particle tracking model is Schiller Naumann drag model.

EMMS

$$\beta_{gs} = \begin{cases} 150 \frac{\varepsilon_s (1-\varepsilon_g) \mu_g}{\varepsilon_g d_p^2} + 1.75 \frac{\varepsilon_s \rho_g |v_g - v_s|}{d_p}, & \varepsilon_g \leq 0.74 \\ \frac{3}{4} C_D \rho_g \frac{(1-\varepsilon_g)\varepsilon_g}{d_p} |v_g - v_s| \omega(\varepsilon_g), & \varepsilon_g > 0.74 \end{cases} \tag{2.34}$$

$$\omega(\varepsilon_g) = \begin{cases} -0.5769 + \frac{0.0214}{4(\varepsilon_g - 0.7789)^2 + 0.0044}, & 0.74 < \varepsilon_g \leq 0.82 \\ -0.0101 + \frac{0.0038}{4(\varepsilon_g - 0.7789)^2 + 0.0040}, & 0.82 < \varepsilon_g \leq 0.97 \\ -31.8295 + 32.8295\varepsilon_g, & \varepsilon_g > 0.97 \end{cases} \tag{2.35}$$

$$C_D = \frac{24}{Re}(1 + 0.15 Re^{0.687}) \tag{2.36}$$

Schiller Naumann drag model

$$f = \frac{C_D Re}{24} \tag{2.37}$$

$$C_D = \frac{24}{Re}(1 + 0.15 Re^{0.687}) \tag{2.37}$$

Where β_{gs} is fluid-solid exchange coefficient.

Related literatures

Wei et al. [9] compared the influence of anatomical and physiological airway change due to different head and neck position using computational fluid dynamics. A healthy female volunteer was undergone CT examination. First, the neutral position by naturally lying flat, second, the extension position by head extension and shoulder elevation and third, the sniffing position by head elevation as if you were trying to sniff the air were performed. The results showed that each head and neck position had different narrowest cross-sectional area. These might result in different flow behavior as the sniffing position had nearly 3 times wider cross-sectional area than its neutral position. Therefore, the air velocity in this position was much lower. As well as the pressure drop in this position was also lower, which led to the decreasing of airflow resistance. The recirculation airflow was found near the sub-glottic region in both neutral and extension position. To improve airway patency, sniffing position was suggesting to be used for aerosol drug delivery and mask ventilation.

Maseri et al. [10] studied the steady and transient transport of the micro particle within realistic model of the human upper airway. The model was included both inhalation and exhalation phases of breathing. The breathing was studied under realistic cyclic breathing and equivalent steady airflow condition. The results showed that the steady state simulation with equivalent airflow rate of the transient simulation could predict the deposition fraction of particle with reasonable accuracy, which could gain some benefits from the reduction of the computational time. However, the regional predictions of the particle deposition fraction were remarkably different from the results obtained from the transient simulations. This might not be accurate for cyclic breathing conditions. In addition, the particle penetration fractions were also different. Hence, the transient simulations were needed to predict particle penetration into the lung.

Kerakes et al. [11] developed the method based on vibrational spectroscopy using Raman and infrared to investigate the aerosol drug deposition in human airway system. The realistic human airway system was printed using 3D printer for rapid prototyping. Three different types of aerosol drugs were separately packed into the metered dose inhalers. The silicon substrates were placed inside the system to collect the aerosol particles that were fed in. The measurement results of the transmittance of the spectra

in the range of 500-2000 cm^{-1} were mapped and calibrated with the characteristic peak of each aerosol type. The intensity of the peaks was plotted as contour. To verify this measurement technique, the visual observation using optical microscopic images were used. The results from the mapped peak of Raman and infrared could be used as a deposition observation technique which had a good agreement with an optical microscopic image.

Koullapis et al. [12] investigated the deposition of the particle in realistic domain reconstructed using multi-detector computed tomography. The charged aerosol particles with diameter of 0.1, 0.5, 1, 2.5 and 10 microns were used in this study. As the level of the charge were depended on the size and physical properties of the aerosols, the wide range of the elementary charges, 0-1000, were considered. These ranges are below the maximum charge holding limit of the aerosol. The result revealed that the electrostatic charge only played roles when the particle size was lower than 5 microns as the inertial impaction was dominant. For the particle with 0.1 microns of diameter, the overall deposition fraction for 1000 elementary charge was approximately 7 times higher than that of the no charge particle within the same size. In summary, the electrostatic charge increased overall deposition for the particle especially for small particles.

Miguel et al. [13] studied the penetration pattern of the aerosol. The experiment using glass fiber tubing representing the human respiratory tree was conducted. The tube was replicated of the authentic model for the bronchial tree from the first branch of the trachea to the seventh generation of the tree. Alumina particles with the size in range of 0.5 to 20 microns were used as an inhaled particle. Then, the penetration fraction had been studied. The experiment showed that the large-sized particles was significantly decreased the particle penetration fraction. In addition, the respiration frequencies showed the same trend. These behaviors could be represented using dimensionless number, Reynolds number and Stokes number. The particle penetration fraction was decreased with the decreasing of Reynolds number and the increasing of the Stoke number.

Phuong et al. [14] investigated the flow pattern of upper human airway using experiment and computational fluid dynamics technique (CFD). The experiment was conducted using particle image velocimetry (PIV). The Reynold's number of the fluid

entering the domain was controlled to ensure the corresponding of the actual breathing condition, 7.5, 15 and 30 L/min. The scattered light from tracer particle in the fluid was then captured. Three turbulent models, LRN k-e model, RNG k-e model, and SST k-omega model, were studied. The result showed that the flow structure from PIV was similar for all three flow rates. The CFD results were consistent with those from PIV. The LNG k-e model was in good agreement with the experiment in term of velocity profile and peak velocity location. The nasal and oral inhalation was also evaluated. The result revealed a notable flow inclination due to pressure gradient from centrifugal force and the secondary motion of the fluid when the air was bend from the larynx to the trachea.

Pourmehran et al. [15] investigated the airflow of the magnetic drug career (PMS40) using computational fluid dynamics technique. The dense discrete phase model (DPM) was applied to describe the flow behavior of the career where the external magnetic source was existed. The magnetic source was utilized in the first two zones of the human lung. The model was generated using realistic computed tomography. The air was fed at the rate of 15 L/min. The effect of magnetic source position, particle diameter and magnetic number was studied. To deliver the drug career to a first bifurcation, the magnetic source distance should increase further from the inlet. For the magnetic number of one Tesla, the drug deposition efficiency decreased with the increasing of the particle diameter between 2 to 5 microns. The effect was in reverse relation when the particle was larger than 5 microns. Also, the higher value of magnetic number, the drug deposition efficiency increased.

Rahiminejad et al. [16] investigated pressure and velocity distributions during sneezing of 24-year old female subject. The effect of reaction of the subject including nose holding and closing the mouth while sneezing was also investigated. Computational fluid dynamics model of a realistic human upper airway was derived and developed using CT scan images. A hybrid mesh scheme with prismatic and tetrahedral elements was implemented to capture the interaction between the air and the walls of the system. SST k-e was used as a turbulence model because the simulated results had a lower error comparing to the available experimental data. The normal sneezing condition without any obstacles was found by applying the pressure of 8 kPa where the air flow rate would equal to the average volume flow rate of 470 L/min. The further experiment of the

subject reaction was assumed that the sneeze happened with either the same inlet pressure or the same flow rate. The results showed that, by holding the nose or mouth, the pressure difference along the tract was increased from 5 to 24 times over that of normal sneeze condition.

Zubair et al. [17] reviewed the limitations of CFD modeling in nasal airflow. Postural effect during imaging could be affected by posture position. Respiratory tract was tending to be narrowest in supine position and widest in prone position. Changes in anatomical geometry due to postural changes had never been studied before. In addition, subject gender could also affect the flow resistance. Male subject had longer pharyngeal airway length and larger cross-sectional area of soft palate. The soft palate was soft tissue distinguished from the hard palate at the front of the mouth. With greater area, the shear force on incoming air was much higher. In such case, there was still no specific numerical modeling studies had been carried out to compare the effect of gender. While many researchers employed the plug flow boundary condition with fixed airflow velocity, nasal cavities were narrowing and widening simultaneously during each breathing cycle, which then caused the flow to be fluctuated with irregular patterns and frequencies. Therefore, fixed velocity boundary condition was not suitable for natural physiological inspiration modeling. In fact, pull-flow boundary was more appropriated as the expansion of the lungs would be set as a negative pressure gradient. Furthermore, respiratory tract contains mucociliary clearance mechanism which helped to maintain epithelial moisture and traps particulate material and pathogens moving through the airway. Without these mucous layers, the result tended to be inaccurate. To develop better model these assumptions must be addressed.

Xu et al. [18] investigated the air flow and temperature gradient within a realistic human airway. As the injury from fire smoke inhalation was a major concern which caused burn-related death issue. The human airway, including nasal, oral, pharynx, trachea and part of first generation of the tracheobronchial tree, was built from the magnetic resonance imaging (MRI). The user-defined function of Pennes' bioheat transfer equation was introduced to capture the heat generated from metabolism, blood circulation and heat conducted from human tissue. The inlet air temperatures were set to be 45℃, 80℃ and 120℃, which represented the early stage temperature of fire. The simulation results indicated that the inhaled hot air was mainly affected the oral cavity.

The inhalation flow rate was one of the factors that affected the interior temperature distribution and the particle deposition. The increasing of the particle size gave a rise to a deposition fraction. The inlet temperature only had a minor influence in the case of bigger particles.

Huang et al. [19] proposed a multiphase kinetic theory model to describe the flow behavior of the red blood cells (RBCs) in a coronary artery. The pulsation of the flow was considered to match with human cardiac waveform. The computational results showed that the migration of the red blood cells away from the vessel walls was occurred in the entrance region of the artery. This migration was caused by the shear in the multiphase granular theory model. The computed viscosity was decreased with shear rate and vessel size. The results were also matched with the measurement. The wall shear stress was found to be highest in the inside area of the system curvature. The oscillating shear index (OSI) could be used to identify the deposition location indication where the particles did not align with the flow direction.

Olgac et al. [20] developed computational fluid dynamics model of LDL transport from the artery lumen to the arterial wall. The volume and solute flux were reported to be affected by the local wall shear stress along the endothelial cell layer. The model was applied to the axisymmetric stenosed artery. The three-pore model was used to describe the contribution of vesicular pathway, normal junction pathway, and leaky junction to determine the value of volume and solute flux. The result showed elevate level of volume flux and solute flux at low shear stress regions.

Giulia et al. [21] investigated atherosclerotic plaque formation in its early stage. The interactions of LDL and the other substances in stenosed artery were studied. It was observed that the formation of the plaque was corresponded with the wall shear stress and the growth was also found to be dependent on LDL levels. The location of plaques and their characteristics were found well when comparing with biological hypothesis.

The four-layer model for the LDL transport in the arterial wall was developed by Yang and Vafai [22]. The endothelium, intima, internal elastic lamina (IEL) and media were modeled as homogeneous porous media. Staverman filtration and osmotic reflection coefficients were introduced to govern the permeability of each porous layer. The results demonstrated that the endothelial diffusive permeability was increased with pressure. In addition, the pressure-driven convective flow enhanced the LDL uptake.

The inlet and outlet boundary conditions were highly sensitive to the species concentration profile within the arterial wall.

Kenjeres and Alexander [23] integrated the four-layer model of Yan and Vafai [22] to the carotid artery bifurcation. The study revealed the strong relationship between blood flow pattern including the wall shear stress distribution and the uptake of the LDL concentration. The model was used to predict the LDL concentration level within a rabbit aorta which was well validated with the experimental results.

Gabriel et al. [24–26] investigated the feasibility of implementing steady-inflow condition instead of transient pulsatile flow in the modeling of atherosclerosis growth as the difference of the two flow fields might result in affecting the flow convection of transport species. The results revealed that the two flow fields were generally similar. However, ignoring the pulsatility might not be appropriate to describe the behavior near-wall transport of the model, since it would be influenced by the time-varying flow features, such as recirculation which was directly influencing the growth of atherosclerosis. Further study of Gabriel also developed index to quantify the flow oscillation so called oscillatory flow index (OFI). It was extended from the widely used oscillatory shear index (OSI). The index demonstrated by ranging the flow from direction-reversing (DR) to non-direction-reversing (NDR) modes, which revealed that DR mode was most prominent at sites of separating and reattaching flow. Whereas NDR modes were spatially spread and propagated from their sources. It was proposed that the flow behavior might be refined by segregating oscillatory flow modes.

CHAPTER III

CFD APPLICATION IN RESPIRATORY SYSTEM:

Computational fluid dynamics simulation of full breathing cycle for aerosol deposition in trachea: Effect of breathing frequency

The emission of fine solid particles is the causing of environmental problems. It also affects human health. The vulnerability of these fine particles leads to the chronic respiratory diseases, such as lung cancer, asthma, etc. These particles are too small which cannot be filtered and captured by human nasal hair [27,28]. The direct treatment of these diseases is to deliver the drug on to the site itself. This medical technique is called aerosol drug delivery.

The small aerosol drug particles can be design specifically to directly deliver them to the disease site. It is the most efficient way for direct treatment of the respiratory disease. However, the proper design of the aerosol is required to maximize the effectiveness and reduce the side effect of treatment. Thus, the understanding of the flow pattern is essential for the aerosol drug design.

One of the main factors affecting the flow of the aerosol is the electrostatic charge. The force of electrostatic interactions plays an important role as the charges are transferred from the particles to the surrounding body and vice versa. The charges with the same type are created repulsive force which repelled them apart. The opposite charges create attractive forces which induce the particle agglomeration. The relationship of the electrostatic charge can be used to manipulate the aerosol movement. By inducing the different charge type, it can assist the flow for localized targeted drug delivery, in contrast, it can also be used to repel those aerosols from other unwanted area.

The studies of particle transport in human airway with different breathing condition, light breathing, normal breathing, and heavy breathing were conducted by many researchers [15,29]. These literature studies used computational fluid dynamics technique to investigate the particles movement using Lagrangian approach [30,31]. The results were different for each of the breathing conditions. The maximum

deposition fraction was found in the upper zone for the normal and light condition. The result was shifted downward to the deeper zone with heavy breathing condition.

The recent studies investigated the effect of the electrostatic force acting on the aerosol drug using computer simulation. They were focused on the magnetic drug carrier (PMS40) using discrete phase model (DPM). The flow phenomena of the aerosol were observed while applying the magnetic source in the first two zones of the human lung. The constant flow rate of air was fed from the inlet at 15 L/min. The study parameters were magnetic source position, aerosol particle diameter, and the magnetic flux density. The result showed that in order to deliver drug to the first bifurcation of the airway, the magnetic source must be put further away from the inlet. For the magnetic number of one tesla, the deposition efficiency of the aerosol decreased with the increasing the particle diameter from 2 to 5 micron. Also, the improvement of the deposition efficiency could be done by increasing the value of magnetic flux density [12,15].

The studies of charged aerosol for both in-vivo and in-vitro reported that the deposition efficiency of the submicron particle was higher when the particle carried higher elementary charge [32–34]. Even though, the design of aerosol devices industry such as inhaler has been improved by the advancement of technology. The instruments are more capable of generating precise charge aerosol. The innovative studies on the effect of electrostatic charge are still needed for better instrument design.

As stated above, previous studies have been investigated the flow behavior of the charge aerosol using Lagrangian approach which required much more computational resources. This study focused on implementing the electrostatic charge model within human airway using Eulerian (Euler-Euler) approach. By varying the breathing frequency, the effect of respiratory frequency on the deposition of the particles was studied. The normal breathing frequency of the average human adult was 15 breaths per minute (BPM) [35]. The breathing frequency could be faster or slower depended on various factors, such as age, gender, or current physical activity [36]. The study flow domain was reconstructed from the patient-specific three-dimensional (3D) computed tomography. The study reintroduced the measurement of the oscillatory flow velocity index (OVFI) to assess the fluctuation of the flow indicating the deposition location of

the aerosol. The OFVI had been previously used to quantify the blood flow oscillatory behavior [24], which will be beneficial to the study of air flow in human airway as well.

Experimental

Computational domain

The computational domain of the human airway was reconstructed from the patient-specific computed tomography shown in Figure 3.1. The DICOM files were rendered to the 3D geometry in an open-source 3D Slicer software by putting all the image slices together. The rendered 3D model is shown in Figure 3.2. The model was exported as .STL file compatible with commercial ANSYS Mesher 18.2. The model then discretized as the computational grid with the number between 100,000 to 200,000 cells. The model had three boundaries for the flow to enter and exit, one at the foremost top and two at the bottom. This computational model will be used in both inhalation and exhalation phases. For the inhalation, the top boundary was set as inlet for the air and aerosol particles to enter the trachea. The fluid transported along the passageway until it reached the first bifurcation. Then, the flow split into left and right bronchi. At the end of both bronchi, there was an outlet on each side. For the exhalation, the boundaries would be swapped, the gas then flew in from the bottom of the domain and flew out at the top of the domain which allowed the trapped particles and the air inside the domain to flow reversely out of the system.

Figure 3.1 *The 3D CT-scan images of the studied patient*
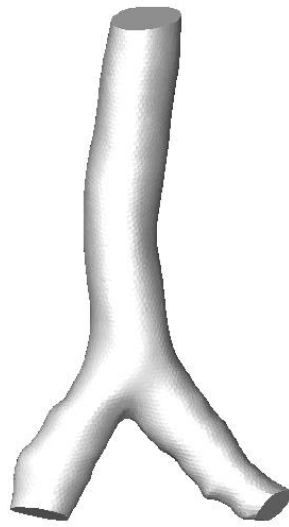
Figure 3.2 *Reconstructed 3D model from the CT-scan images of the patient*
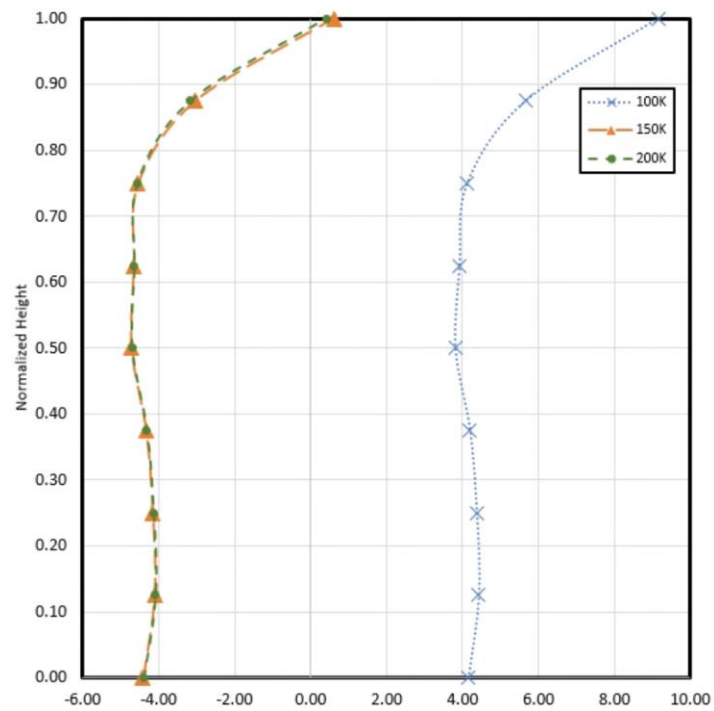
Figure 3.3 *The axial pressure profile for grid independence testing*

The shape of the trachea domain was an irregular shape. Thus, the generation of the mesh was done with the polyhedral structure for better cell gradients approximation compared with the tri/tetrahedral structure, as well as, to reduce the total cell counts. The grid independent test was conducted to verify the precision of the calculation. The pressure profile along the length of the trachea is shown in Figure 3.3. Three differences grid size were compared. The profile showed substantial different results. The 100,000 cells count had insufficient number of cells to precisely obtain the result. The profile was deviated from the others. A 150,000 cells count gave a similar profile which consistent with the 200,000 cell count. The optimized cell count with sufficient quality helps to reduce the computational resources. It clearly showed that the 100,000 cells grid did not have enough cells to obtain accurate results. The 150,000 cells count was then definitely chosen as the suitable one for the rest of the study.

Mathematical model

The governing equations with the additional source term equations were implemented to ANSYS Fluent 18.2. The electrostatic model was added to the model to take the charge particles into account. The Euler-Euler multiphase flow model was developed [37]. The solid phase was treated as the inter-penetrating continua. The kinetic granular theory and the frictional theory, used to solve solid pressure and viscosity, were included in the model [38].

The continuity equations for multiphase flow are given as

$$\frac{\partial}{\partial t}\left(\varepsilon_g \rho_g\right) + \nabla \cdot \left(\varepsilon_g \rho_g v_g\right) = 0 \tag{3.1}$$

$$\frac{\partial}{\partial t}\left(\varepsilon_s \rho_s\right) + \nabla \cdot \left(\varepsilon_s \rho_s v_s\right) = 0 \tag{3.2}$$

whereas the momentum conservation equations are shown in Eqs. 3.3 and 3.4:

$$\frac{\partial}{\partial t}\left(\varepsilon_g \rho_g v_g\right) + \nabla \cdot \left(\varepsilon_g \rho_g v_g v_g\right) =$$

$$-\varepsilon_g \nabla p + \nabla \cdot \tau_g + \varepsilon_g \rho_g g - \sum_{s=1}^{n} \beta_{gs}(v_g - v_s) \tag{3.3}$$

$$\frac{\partial}{\partial t}(\varepsilon_s \rho_s v_s) + \nabla \cdot (\varepsilon_s \rho_s v_s v_s) =$$

$$-\varepsilon_s \nabla p + \nabla P_s + \nabla \cdot \tau_s + \varepsilon_s \rho_s g - \sum_{s=1}^{n} \beta_{gs}(v_g - v_s) + F_{qs\alpha} \qquad (3.4)$$

β_{gs} is the gas-solid exchange coefficient. The subscript "s" and "g" are represented the solid and gas phase, respectively. v_s and v_g are the respective velocity vector field in the trachea. The symbol, p, ρ, μ, ε and P_s are the trachea pressure, density, dynamic viscosity, volume fraction and granular pressure, respectively. The stress tensor (τ) is defined as

$$\tau = \varepsilon\mu(\nabla\vec{v} + \nabla\vec{v}^T) + \varepsilon(\lambda - \frac{2}{3}\mu)\nabla \cdot \vec{v}\bar{\bar{I}} \qquad (3.5)$$

where I is the unit tensor and t is the current flow time. λ is the bulk viscosity of the arbitery phase. The Brownian motion can be neglected in the study as the size of the aerosols are in micrometer size [39,40]. The fluctuating kinetic energy of granular flow is specified as

$$\frac{3}{2}\left[\frac{\partial(\varepsilon_s \rho_s \theta)}{\partial t} + \nabla \cdot (\varepsilon_s \rho_s \theta \vec{v_s})\right] = \left(-P_s\bar{\bar{I}} + \vec{\bar{\tau}_s}\right):\nabla\vec{v_s} + \nabla \cdot (k_s \nabla\theta) - \gamma \qquad (3.6)$$

where θ, k_s, and γ is granular temperature, granular conductivity and collisional energy dissipation, respectively. The random particle kinetic energy measures per unit mass is defined as granular temperature. ($\theta = \frac{1}{3}\overline{v'_s v'_s}$ where v'_s is fluctuating solid velocity [41]).

The air in gas phase was assumed as an incompressible fluid. The density, viscosity and static pressure were defined as constants. The modified minimization multi-scale (EMMS) model was used to describe the drag force between the gas phase and solid phase. The EMMS model was very well suit with the system with particle cluster [8].

The electrostatic charge is taken to account as the particle size is so small. The electrostatic force ($F_{qs\alpha}$) causing by the electric potential gradient may affect the flow behavior of the particle as the force is greater than its gravity force and drag forces [42]. The force could make particles to agglomerate and form the cluster. The particle cluster with electrostatic charge were pushed toward or away the

trachea wall depended on their charge properties. Rokkam's model [43] was developed and implemented for electrostatic force. This model is based on Maxwell equations, which is the combination of four derivative equations, including Gauss's law of electric field, Gauss's law of magnetic field, Faraday's law of induction and Ampere's law. Putting these equations to Lorentz force equation, the calculation of the electrostatic force acting on the particles is shown in Eq. 3.6.;

$$F_{qs\alpha} = q(E + v \times B),$$ (3.6)

where F is the force acting on the particle under magnetic field (N), q is the electric charge (c), E is the electric field (N/c), v is a velocity of the electric charge (m/s) and B is the magnetic flux density (A/m). The equation can be reduced to $F_{qs\alpha} = qE$ as the charge velocity (v) is very low compared with the speed of light.

Gauss's law, in terms of the derivative, is shown in Eq. 3.7;

$$\nabla \cdot D = \rho_c,$$ (3.7)

where D is the electric displacement vector and ρ_c is the charge density. The relation between the electric displacement vector and the electric field can be described by Eq. 3.8;

$$D = \epsilon_0 E + P,$$ (3.8)

where P is an induced polarization and ϵ_0 is the permittivity of a vacuum. This constitutive relationship describes the polarized induction under an isotropic medium. The electric field, in terms of the charge density, can be derived from Eq. 3.9;

$$\nabla \cdot \epsilon_m \epsilon_0 E = \rho_c,$$ (3.9)

where $P = \epsilon_0 \chi_e E$ when χ_e is the electric susceptibility measured from the experiment. The value of ϵ_m can be found in the previous literature [44]. The equation can be linearly fit with the volume fraction of solid particles and the volume fraction of gas, as shown in Eqs. 3.10 and 3.11;

$$\varepsilon_m = 0.97 + 1.20\varepsilon_s = \varepsilon_g \left(\frac{2.17}{\varepsilon_g} - 1.20\right) \qquad (3.10)$$

$$\rho_c = \sum_{\alpha=1}^{N} q_{s\alpha}\, \varepsilon_{s\alpha} \qquad (3.11)$$

The model was included in the momentum equation in a source term to represent the force acting on the solid phase in Eq. 3.4. In addition, the kinetic theory of granular flow was included in this model, which determined the fluctuation kinetic energy and collision of solid particles.

However, the exact value of the Reynolds number was unknown. Recent studies of four flow turbulence models in human airway were reported that there is only a minor deviation from the results compared with that of the laminar flow model [45]. As the trachea domain had larger diameter with less complexity than those of the pharyngeal region, the flow was similar as a flow in single straight conduct. The estimated mean Reynolds number at peak inhalation was determined using hydraulic radius, given a value of 2,200. The value had been reported to be in range of resting and in activity conditions [46]. Thus, the unsteady state air flow in this study was expected to be mostly existing in laminar flow region [45].

Boundary and initial conditions

The computational fluid dynamics was studied in three-dimensional space. The trachea wall was set as the no-slip boundary condition. The air and aerosol particle were fed together at the inlet of the domain. The inlet boundary was controlled by user defined function (UDF) using ANSYS fluent built-in complier. The inlet velocity profiles of gas phase and solid phase were programmed as shown in the Figure 3.4. The complete flow cycle was separated as the inhalation and the exhalation phases which was different than other studies which only applied a constant inlet velocity [14,29,47]. The inhalation phase was started where the velocity was gradually increased from zero until it reached peak velocity where the velocity gradients was zero. The inhalation phase completed when the flow velocity was gradually reduced to zero. The trachea inlet was set as velocity inlet, and those two faces at the bottom were treated as pressure outlet. For the exhalation phase, those two boundaries at the bottom were swapped with

the trachea inlet to become the inlet themselves. The given velocity profile was given as a cyclic sinusoidal time function as shown in equation 3.12 [10,48].
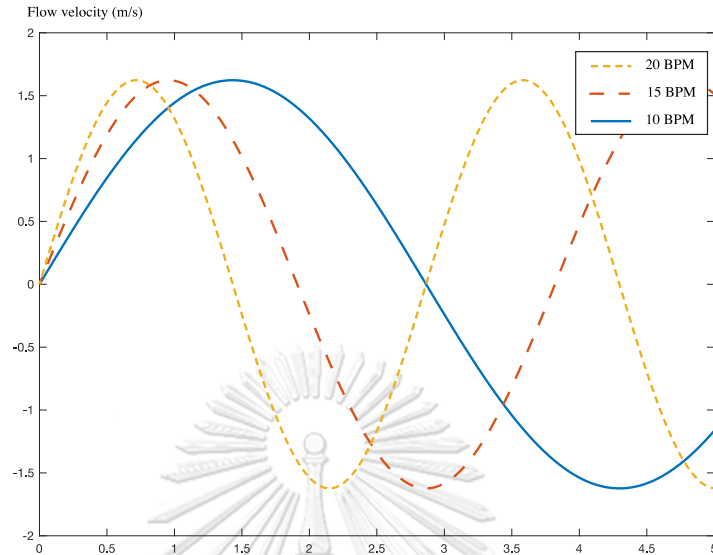
Figure 3.4 *The inlet velocity profile for all studied cases*

$$v = \frac{Q}{A}\sin(2\pi ft) \qquad (3.12)$$

Where v is the velocity normal to the boundary inlet face. Q is the maximum flow rate; A is the cross-sectional area of the inlet face. f is the breathing frequency, and the current flow time. The average volumetric flow rate of human breathing in usual activity estimating from peripheral airway was 30 L/min [49]. To study the effects of breathing frequency, three breathing scenarios were considered, light (10 BPM), normal (15 BPM), and heavy breathing (20 BPM). The pressure boundary condition for the inhalation phase was assumed as pleural pressure which given in Figure 3.5 [50].

The pressure outlet for the exhalation phase was set as constant atmospheric pressure. For the wall boundary, the electric potential was set as zero. Aerosol particles with fixed diameter of 1 micron and density of 1,100 g/m^3 were used in this study [51,52]. Aerosol particles were intended to make sure that they will deposit on to trachea wall. The aerosol charge was assumed to hold 1,000 elementary charge which was below the Rayleigh limit of the charge and also the general range of normal aerosol drug [12,53]. The initial condition of the air and

aerosol particles was set as zero with zero velocity gradient. The aerosol collision with the wall was assumed to be inelastic. The air was assumed to be isothermal and incompressible. QUICK method was used to discretize all the governing equations. The transient simulation was carried out with the time step of 10^{-4} s. It was iteratively calculated until it reached the convergence criteria of 10^{-4}.
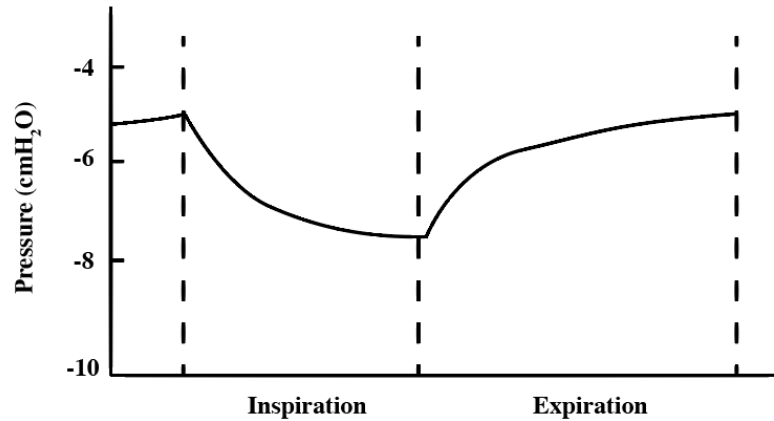
Figure 3.5 *The outlet pleural pressure profile for all studied cases*

Parameter calculation

Wall shear stress (WSS)

Wall shear stress is the force per unit area acting on the wall boundary causing by the velocity gradient causing by the frictional force applied to the adjacent layer of the flow. The WSS (τ_w) is given by equation 3.13.

$$\tau_w = \mu \left(\frac{\partial u}{\partial y}\right)_{y=0},$$ (3.13)

where y is the distance from the wall. The determination of the wall shear stress is an invasive method which can be derived from the governing equations with some limitations as state in Demosthenes et al. work [54]. As the fluid in this study was considered as Newtonian fluid. The viscosity of air was assumed to be constant. Thus, the equation was left only the flow velocity gradient term that affect the wall shear stress. The high wall shear stress region means the velocity gradient is high in that near wall location which means the apostolic particle is expected to collide and deposits more in that region. In contrast, the small value of wall shear stress implies the small movement of the flow near the wall which latter could be attracted or

repelled by the electrostatic force causing by the potential gradient. The wall of the trachea is assumed to be rigid, however the real trachea wall might change during breathing. The skin friction coefficient (*Cf*), which is the derivative of wall shear stress is also examined. It is defined as the ratio of wall shear stress to the reference dynamics pressure which expresses as $Cf = \tau_w / (0.5\rho_{ref} v_{ref} v_{ref})$. where ρ_{ref} and v_{ref} is the reference density and reference velocity given as 1.225 kg/m³ and 1 m/s, respectively.

Oscillatory flow velocity index (OFVI)

Oscillatory flow velocity index (OFVI) is proposed by Gabriel et al. [24] It is an index which extensively used to quantify the oscillatory flow behavior of blood. The idea is to assess the deviation of wall shear stress across the flow domain in the period of the study which can be expressed as

$$OSI = 1 - \frac{\|\overline{\tau_w}\|}{\|\tau_w\|},$$ (3.14)

where $\tau_w = \Theta_i - (\Theta_j n_j) n_i$ of the traction stress $\Theta_i = \tau_{ij} n_j$ and n_i is the unit normal to the wall. The index was normalized to have a range of 0 to 1 to be able to compare with other indices. The index limitation is that it is only able to describe the flow in its wall space. The index was then extended to the flow space in analogous from of the oscillatory index (OI) [55] which is shown in Eqs. 3.15 and 3.16.

$$OI\{\varphi\} = 1 - \frac{\|\overline{\varphi}\|}{\|\varphi\|},$$ (3.15)

$$OI\{\varphi\} = 1 - \frac{\left\|\frac{1}{T}\int_T \varphi dt\right\|}{\frac{1}{T}\int_T \|\varphi\| dt},$$ (3.16)

where φ is the generic flow field variable and T is the assessment time. The oscillatory flow velocity index (OFVI) is obtained from applying the same equation to the flow velocity. The OFVI can be expressed as.

$$OI\{u\} = OFVI = 1 - \frac{\|\overline{u}\|}{\|u\|}$$ (3.17)

The indices applied to all the cell in control volume to measure the flow disturbance. Together, OSI and OFVI are able to measure the disturbance in both wall region and flow region. The indices were intended to develop for arterial blood flow study. Since the flow in human airway were physically solving using the same fundamental, the indices were re-introduced and applied to human airway study.

Results and discussion

The flow domain was divided into 11 sliced planes for better representation of the flow variables. Figure 3.6 shows the sliced planes. It is clearly seen that each plane had different shapes and sizes. The cross-sectional area of the flow domain narrowed from plane 4 to 6, then expanded from plane 7 to 9. The widest section of the flow domain was at the bifurcation where the flow split into two part of the bronchi.

To validate the implemented mathematical model, the flow proportion to the left and right bronchi was compared with that of real human data. The flow ratio to the left bronchus was 0.455 and to the right bronchus was 0.545. The results agreed well corresponded to the data reported from previous literatures [40,56,57]. The implemented mathematical model therefore able to predict the result for further investigate in this study.
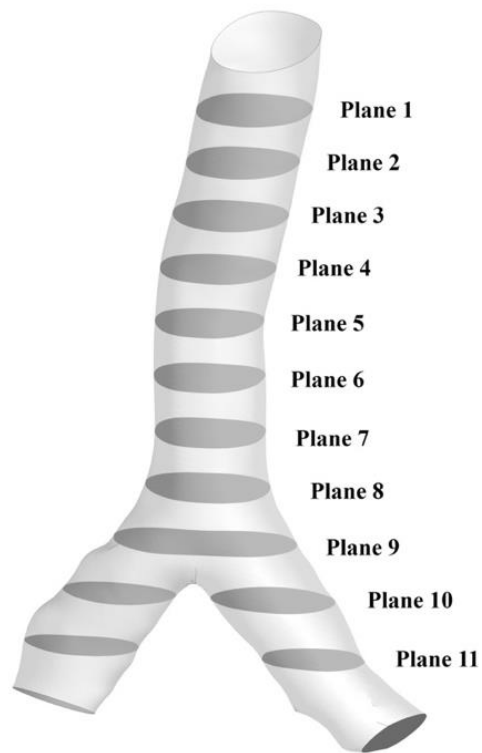
Figure 3.6 *Representative planes*
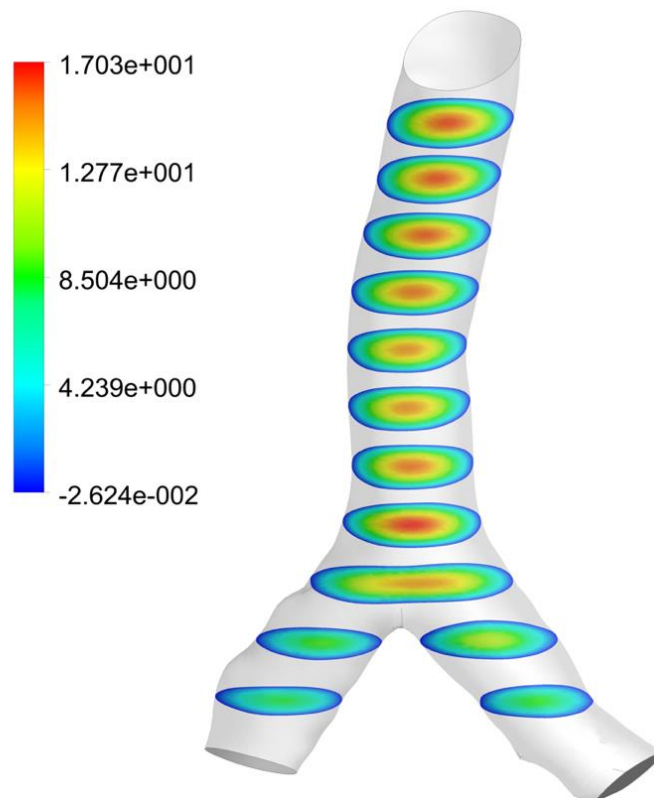
Figure 3.7 *The obtained electrostatic field contour*

Electrostatic field

The electrostatic model was solved on the trachea flow domain to observe the electric potential in the vicinity of aerosol charge. As the positive aerosol charges were continuously fed in to the system, the electric potential gradually changes according to the current amount of charged aerosol. The snapshot of electric potential contour is shown in Figure 3.7. The electric field developed non-uniformly inside the domain. The contour in Figure 3.7 shows that the potential at the wall is zero as set at the boundary condition. The potential was positively increased as it moves toward the center of the trachea. As expect, the solid volume fraction contour confirmed that the aerosol particle was denser at the region close to the wall (Figure 3.8-3.10). The contour also showed the agglomeration of the aerosol particles. Flow behavior of the solid had been altered by the influential of the electrostatic charge especially for the micrometer size of the particles [58]. Previously, experimental result from other literature also reported that the deposition fraction was higher as the aerosol charge increasing [59].

The velocity vector plot in Figure 3.11 also confirmed the aerosol flow behavior. Apart from the volume fraction contour, the velocity vector plot showed the direction where the aerosol particle was moving toward. The color shows the magnitude of the velocity. The aerosol particle flow vectors were mostly showed to move toward the wall of the trachea. The aerosol agglomeration was formed in layer next to the wall. The vector plot revealed the slow movement of the agglomeration layer. In all three cases, the particles were crammed in planes, 4, 10, and 11. The agglomeration of particle were noticeably found at the breathing frequency of 15 BPM and 20 BPM. The flow patterns were disturbed differently for each breathing frequency case. As the flow patterns changed, the aerosol particles might not deposit in the intended location.

Volume Fraction Contour (10 BPM)
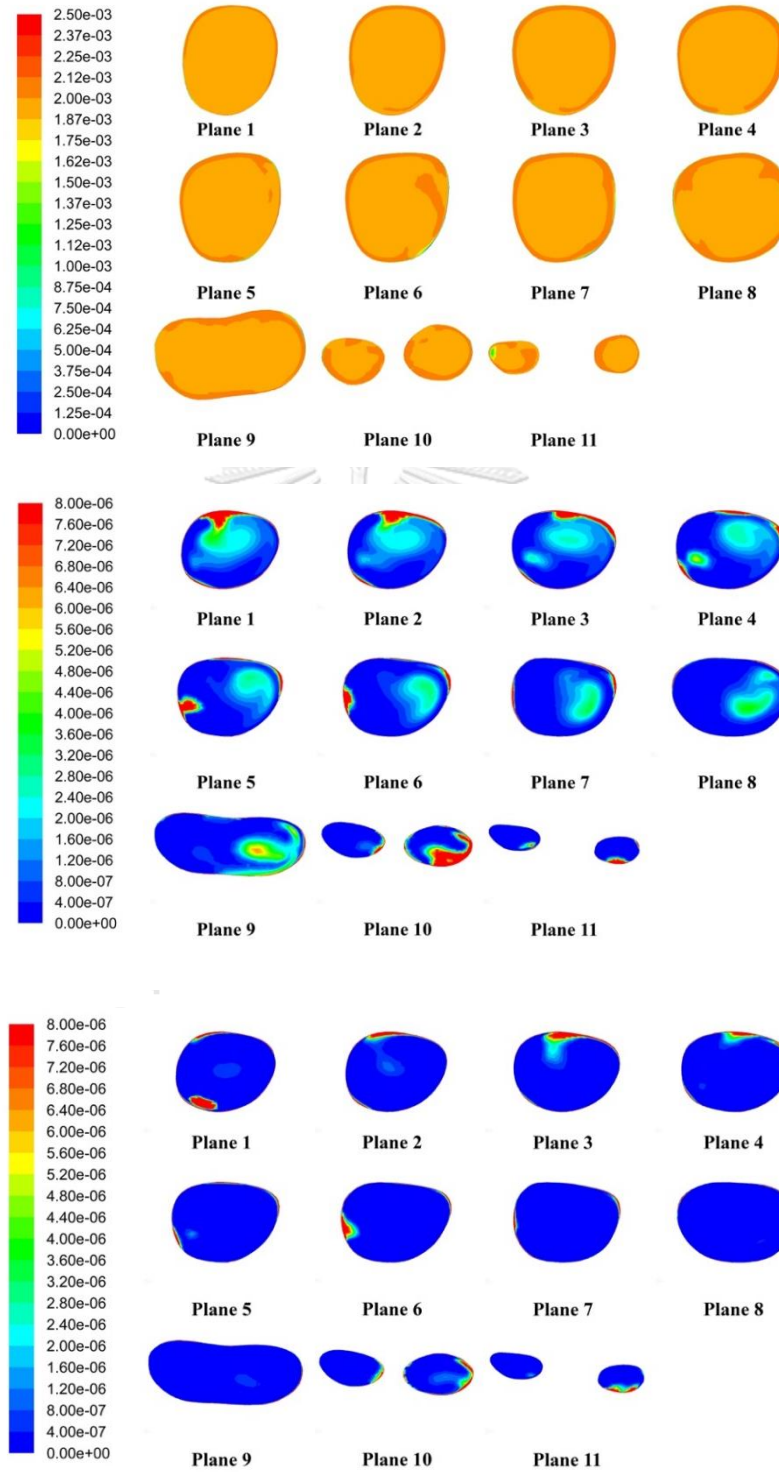
Figure 3.8 *The obtained solid volume fraction contour for a breathing rate of 10 BPM in the (a) inhalation, (b) peak exhalation and (c) complete exhalation phases.*

Volume Fraction Contour (15 BPM)
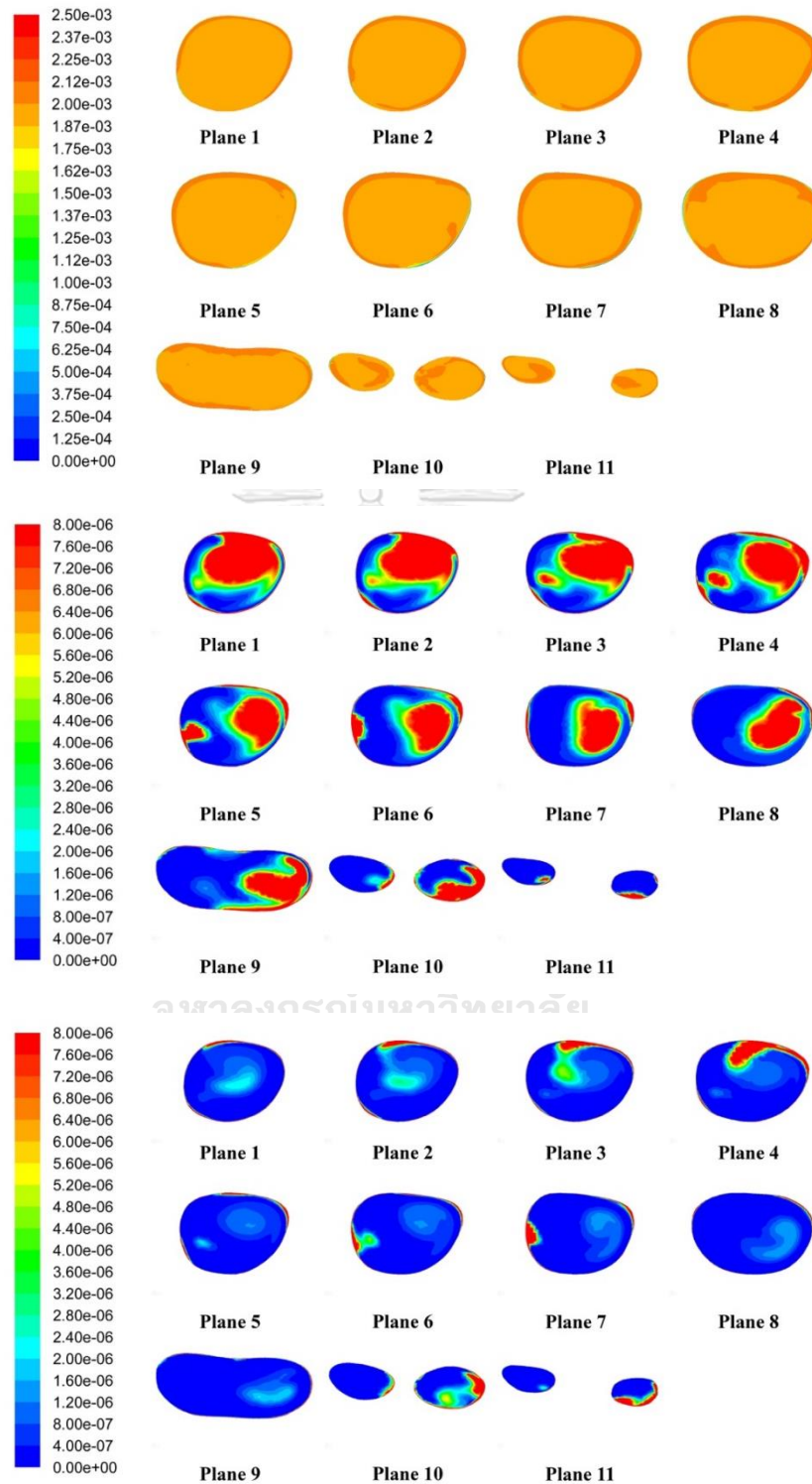
Figure 3.9 *The obtained solid volume fraction contour for a breathing rate of 15 BPM in the (a) inhalation, (b) peak exhalation and (c) complete exhalation phases*

Volume Fraction Contour (20 BPM)
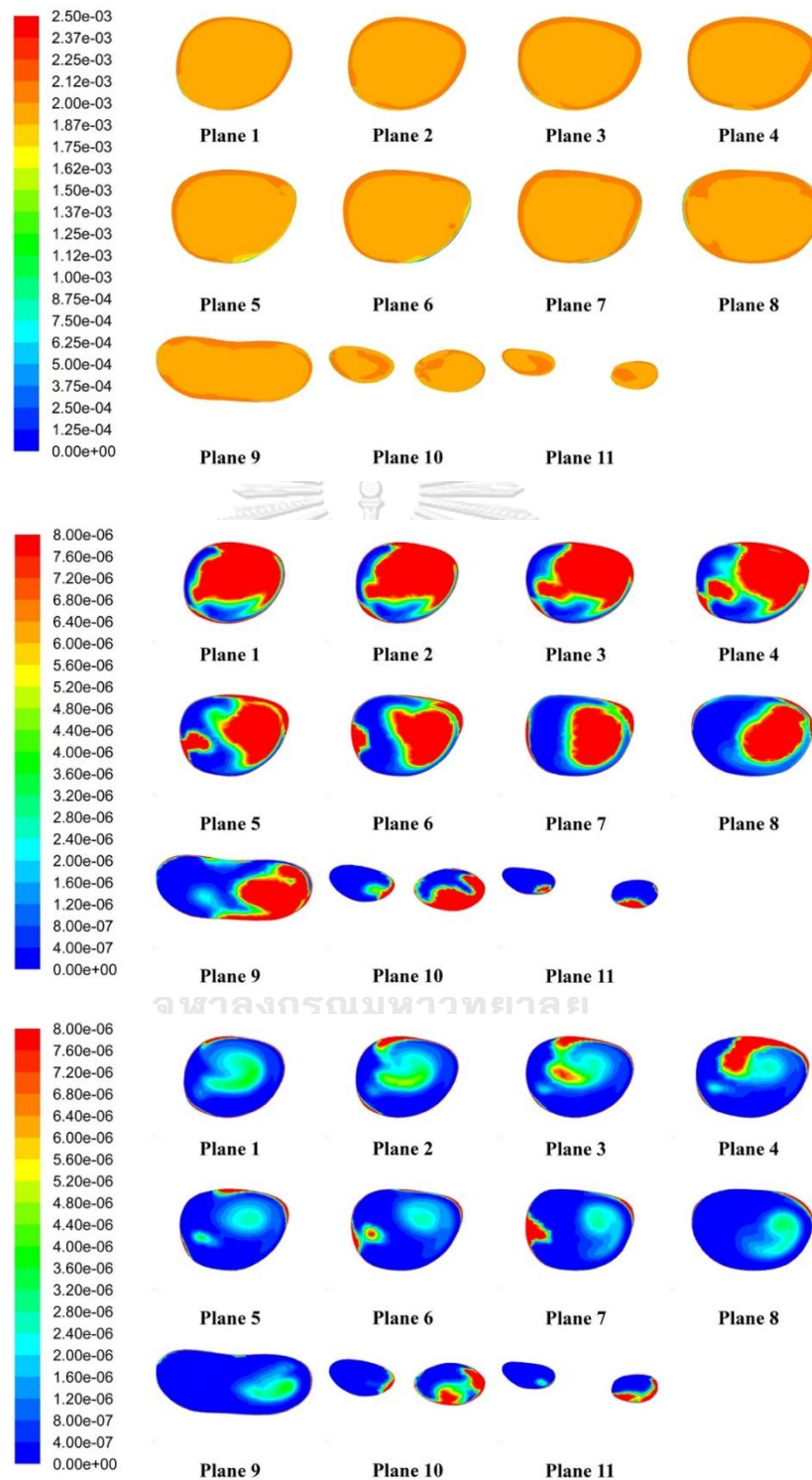
Figure 3.10 *The obtained solid volume fraction contour for a breathing rate of 20 BPM in the (a) inhalation, (b) peak exhalation and (c) complete exhalation phases.*
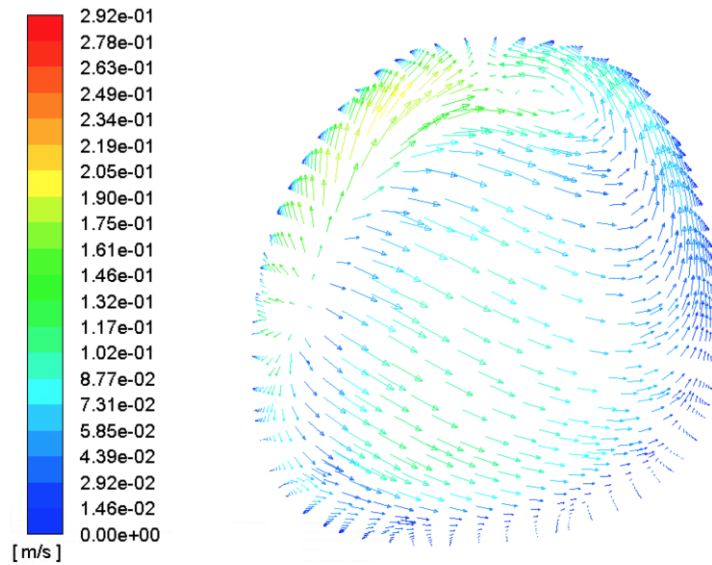
Figure 3.11 *The obtained flow field velocity for a breathing rate of 15 BPM*

Table 3.1 *Leftover fraction (-) of charged aerosol in the system at a given time*

Frequency	Peak inhalation phase	Peak exhalation phase	Fully exhale
10 BPM	1.19E-01	8.15E-04	6.26E-04
15 BPM	1.79E-01	1.45E-03	7.14E-04
20 BPM	2.38E-01	2.83E-03	1.06E-03

The total mass fraction of the aerosol that were still float and left in system after peak inhalation phase and peak exhalation phase and fully exhaled are shown in Table 3.1. The total mass fraction of all cases was similar in peak inhalation phase where the flow velocity was at its highest value. The volume fraction contours of all eleven sliced planes showed significant higher values near the wall region. This is because the electrostatic force pushes the positive aerosol charges towards the location that has low electric potential. After the end of inhalation phase, the flow velocity was gradually reducing to zero. Some of aerosol particles that were unable to penetrate deep enough were suspended inside of the flow domain. These aerosol particles were likely to flow out in the exhalation phase. Previous literatures had not considered this possibility of particles flowing out. They

marked them as trapped particles instead. However, these particles could also deposit on the way out as well.

From the results shown in the table, the total mass fraction of charged aerosol appeared to be lowest for the condition where the breathing frequency was 10 BPM. Since the flow time of this case was longest compared with other cases, the flow might flush out all the aerosol particles in the flow domain. The force acting on the solid particles were unbalanced which causing them to move towards specific direction. In this case, the electrostatic force was not strong enough to withstand the shear force from the main gas flow, the deposited aerosols were then carried out by the main flow.

The flow streamlines are shown in Figure 3.12. There were some regions where the flow streamlines were not aligned with others. It caused by the changing of the cross-sectional area of the geometry. The sudden change of the geometry by the reduction or enlargement of the trachea diameter caused the circulation zone where the flow was moving slowly in the circular region. In this region, the increasing temporal residence time would give a much longer time for the aerosol to move according to the electrostatic force which had a significant influence on the particle comparing to the shear force from the main flow. Thus, the deposition and segregation were mainly found in this region. The volume fraction of the aerosol particles was then dense in some of these planes.

The flow distance in the case of breathing frequency 15 BPM and 20 BPM were slightly shorter than that of the 10 BPM case. The total mass fraction accumulation in the system for these cases were found to be higher, eventhough the overall flow behavior might not have much differences.
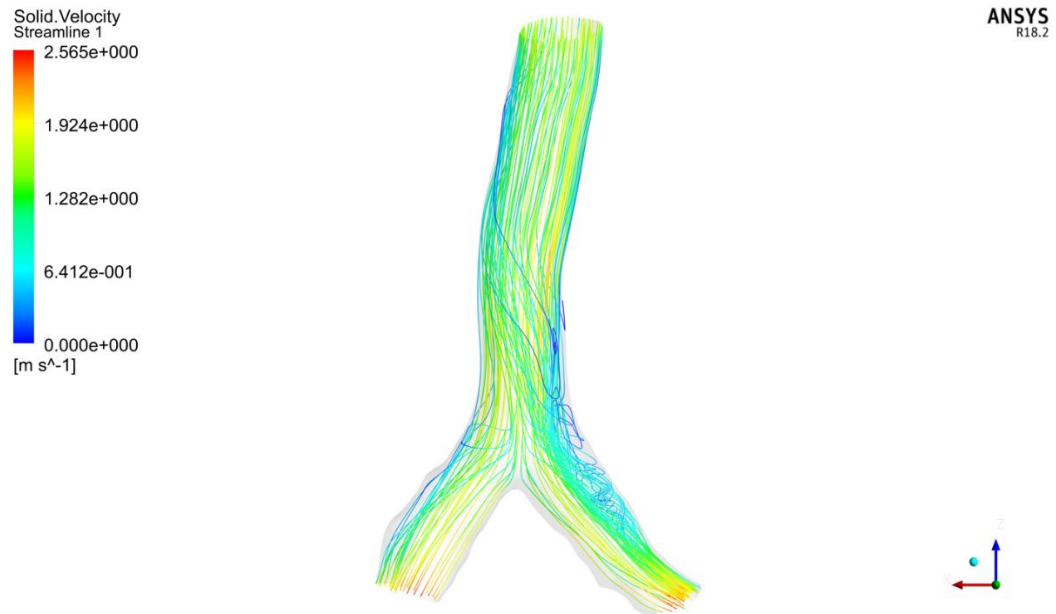
Figure 3.12 *The obtained gas velocity streamline for a breathing rate of 15 BPM*

Table 3.2 shows the average granular pressure for each breathing phase. The results were consistent with the result from the total mass fraction accumulation. The average granular pressure of all cases was similar in peak inhalation phase where the flow velocity was at its highest value. The higher of the granular pressure suggested the higher of the solid volume in that interested region. In 10 BPM case, the result showed the lowest granular pressure, and slightly higher in 15 and 20 BPM cases, respectively, for the fully exhale case.

Table 3.2 *Average granular pressure (Pa) in the system at a given time*

Frequency	Peak inhalation phase	Peak exhalation phase	Fully exhale
10 BPM	2.49E-11	4.91E-11	2.90E-11
15 BPM	2.13E-11	9.93E-11	3.43E-11
20 BPM	2.14E-11	1.81E-10	4.50E-11

Wall shear stress

In general, the flow within the flow domain were not moved with the same velocity at every flow layer. From the streamlines, the flow velocity was the fastest in the center of the trachea. The flow velocity was gradually reduced until

it was slowest at the wall. The friction of the fluid between fluid and the wall created the tangential force onto the wall. As the fluid velocity increased while the fluid was moving away from the wall toward the center of the trachea, the magnitude of the wall shear stress could be observed. According to the flow, the complexity in the flow field will significantly affect the flow velocity, in this case, the wall shear stress will consistently be affected. The changes in the value of wall shear stress imply the location of where the particle collision was occurred which was an alternative method to indicate the particle deposition.

The contour plot of the wall shear stress was shown in Figure 3.13. For all the three breathing frequencies, the wall shear stress was high along the left side of the trachea. The flow velocity was suddenly changed in that region in the inhalation phase. The result was in reversed for the exhalation phase, the wall shear stress value was high on the opposite side. These are the effect of the unsymmetrical geometry of the human airway.

The average value of wall shear stress at each stage of breathing was shown in Table 3.3. The results showed that the average wall shear stress was varied over breathing stages as the particle were fed into the system. The main concern of this study was at the end of the exhalation phase. The average wall shear stress was highest in the case of breathing frequency of 20 BPM. These results were consistent with the volume fraction contours.

As expected, the wall shear stress was lowest for a case of breathing rate of 10 BPM. The total number of aerosol particles accumulation left in the system was the lowest because the particles were already flew out of the system. So, there was just only a small movement of the particle near the wall. The skin friction coefficient was also showing the same trend as wall shear stress. The skin friction coefficient results were shown in Table 3.4. The skin friction coefficient is derived from the value of wall shear stress. These values were also high when the wall shear stress was high.

10 BPM

15 BPM

20 BPM

(a)   (b)   (c)
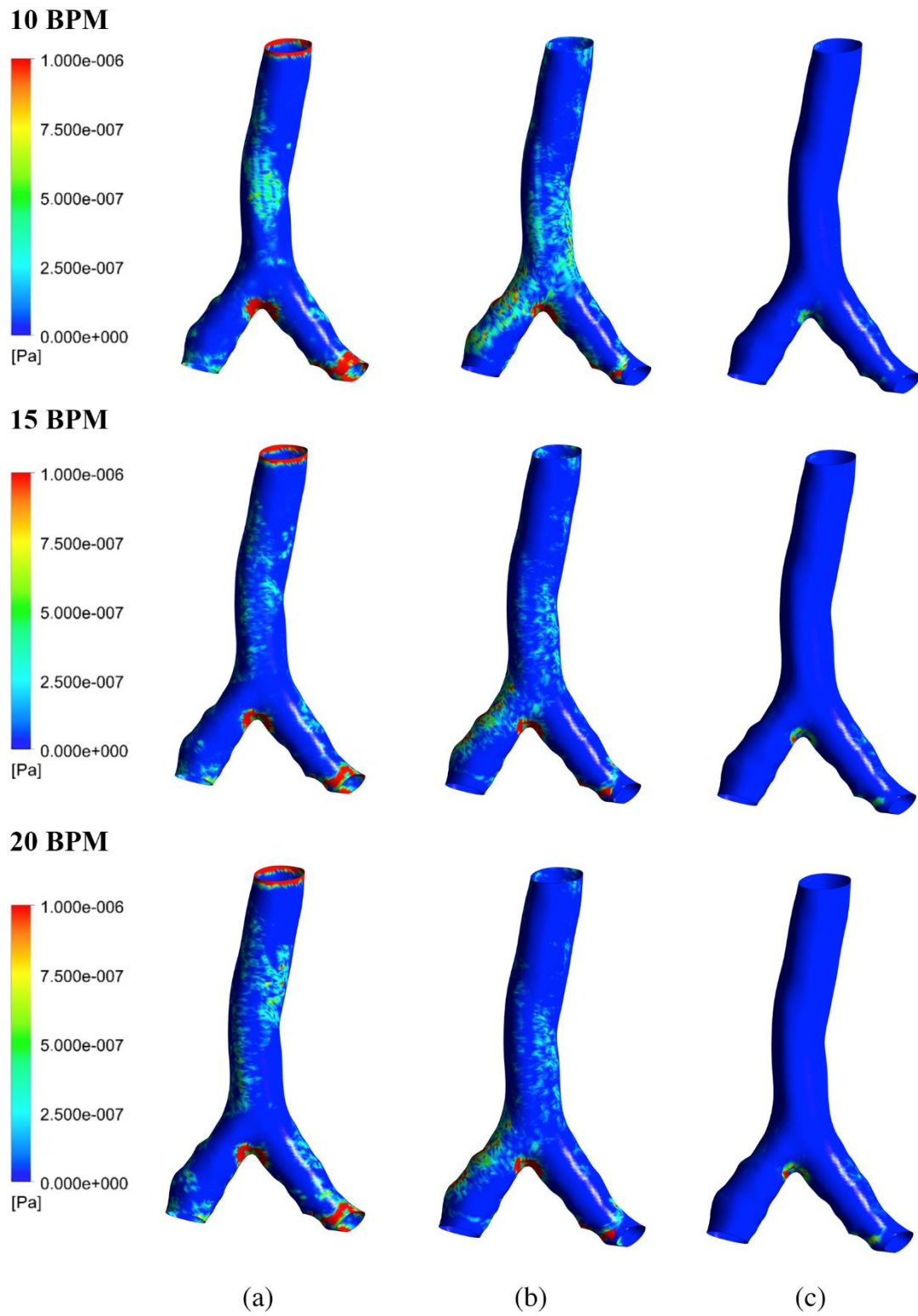
Figure 3.13 *The obtained WSS contour for the (a) peak inhalation, (b) peak exhalation and (c) complete exhalation phases.*

Table 3.3 *Average solid wall shear (Pa) in the system at a given time*

Frequency	Peak inhalation phase	Peak exhalation phase	Fully exhale
10 BPM	1.68E-10	4.90E-09	2.18E-10
15 BPM	2.03E-10	4.86E-09	2.69E-10
20 BPM	2.46E-10	4.82E-09	3.58E-10

Table 3.4 *Average skin friction coefficient (-) in the system at a given time*

Frequency	Peak inhalation phase	Peak exhalation phase	Fully exhale
10 BPM	2.73E-10	8.00E-09	3.55E-10
15 BPM	3.31E-10	7.94E-09	4.40E-10
20 BPM	4.01E-10	7.87E-09	5.84E-10

Many attempts had been done by researchers to develop such a tool such as oscillatory shear index, granular temperature, or oscillatory flow index, to locate the potential site for particle deposition in human organ system, for instance, the location of atherosclerotic lesion growth [19,24]. However, it is proposed here that the highest increase of wall shear stress regions is showing the possible aerosol deposition site. The wall shear stress is a possible index nominating the evaluation of the deposition site in aerosol drug design development.

Granular temperature

The average granular temperature results were shown in Table 3.5. It is so called the solid fluctuation kinetic energy which indicates the fluctuation of the particle velocity. In the case of breathing frequency of 10 BPM, the average granular temperature was the highest which means the fluctuation kinetic energy of the aerosol was still high. The high kinetic energy implied that the particles were still able to move elsewhere. The granular temperature is proportional to the kinetic energy of the random motion of the particles. Comparing the results with other studies, the granular temperature results were relatively low due to the considered volume fraction in this study was very low. The results from the study were in the range of 1E-09 to 1E-11 m^2/s^2 which gave a reasonable extension to the data

trend of the previous literatures [41,60–63] whereas the solid volume fraction was remarkably low values.

Table 3.5 *Average granular temperature (m^2/s^2) in the system at a given time*

Frequency	Peak inhalation phase	Peak exhalation phase	Fully exhale
10 BPM	8.50E-11	9.91E-09	9.96E-09
15 BPM	5.56E-11	9.84E-09	9.94E-09
20 BPM	4.59E-11	9.74E-09	9.92E-09

Oscillatory flow velocity index (OFVI)

OFVI was introduced in this study to obtain the steady-equivalent result of the flow which the flow velocity was averaged over the period of the simulation from the initial to the end of inhalation phase. These results were mandatory for the inhalation-based drug delivery design which helps pharmacist to formulate the site-specific aerosol drug. The OFVI plot helps to identify the oscillatory flow disturbances which affect the flow field. OFVI is an extension to the wall shear stress on to the flow spaces. A higher OFVI value represents the higher flow complexity where the local velocity is fluctuated with time.

The OFVI contours of all three cases were shown in Figure 3.14. In all cases, The OFVI values were high in the same region which was reasonable as all the three cases share the same geometry. The flow should analogously be the same. Comparing the results with volume fraction contour, the agglomeration region of the particles was consistent. Thus, the OFVI was also be able to indicate the aerosol deposition location. This index can also be used for rapidly determine the location of deposition for targeted aerosol drug delivery, which is traditionally used in blood vessel studies.
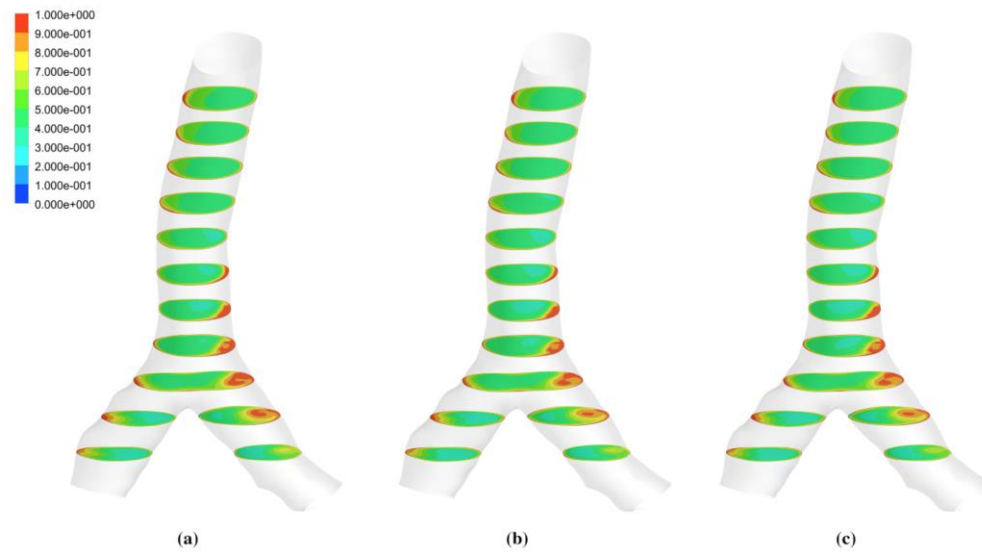
Figure 3.14 *The obtained OFVI for a breathing rate of*
(a) 10 BPM, (b) 15 BPM and (c) 20 BPM

Conclusion

The three-dimension computational fluid dynamics model of patient-specific trachea was investigated based on the data from computed tomography scan. The electrostatic model was implemented to represent the segregation and agglomeration behavior of the aerosol particles. The electrostatic force affected the movement of the particles especially where the flow velocity was low. The low flow velocity regions were primarily at the flow recirculation region. The positive aerosol charge caused them to move away from the center of the domain toward the wall due to lower electric potential near the wall. The flow field results were similarly showed the same pattern in all three breathing frequency (10, 15, and 20 BPM). However, the deposition of the particles was affected by the breathing frequency. A shorter flow time, particles only flew in short distance and then deposited at the upper part of the trachea. A longer flow time, the particles tended to flow much further to the lower part of the trachea. In summary, the computational fluid dynamic model of aerosol including electrostatic charge within patient-specific trachea had been successfully developed. The study reintroduced the WSS and OFVI as potential deposition region indicator. The WSS was high in the region where the particles were deposited. Like WSS, the analogous index, OFVI gave the same trend as WSS. The granular pressure, and skin friction coefficient were able to indicate the deposition trend. The total remaining aerosol particles was reflexed by

the value of kinetic energy, granular temperature and skin friction coefficient. These indices can be implemented into the mathematical model to use as a preliminary prediction of the aerosol deposition location for further problem analysis.

CHAPTER IV

CFD APPLICATION IN RESPIRATORY SYSTEM:

The statistical study of the effect of aerosol properties on the deposition in idealized trachea

Aerosol drug therapy was revolutionized the medication of several respiratory diseases. To efficiently treat the patients with the aerosol, not only the dosage of the active pharmaceutical ingredient (API) but also the location where they're deposited in are essential [64]. Therefore, the study of particle deposition aids the design of the aerosol drug.

The structure of human respiratory tract is complicate in shape and size. It is difficult for researcher to conduct the experiment. The measurement of flow inside the tract is thus challenged and limited. The idealized model was proposed by Weibel et al. [65] which simplified the respiratory geometry by reducing their dimensions and making it symmetrical, resulting in the widely used of the Weibel model among group of researchers to investigate the flow phenomenon for both in-vivo and simulation studies.

In this chapter, the objective of this study is to develop the mathematical model and to identify the significant factors of aerosol properties affecting the particle deposition using multiphases Euler-Lagrangien computation fluid dynamics technique. In order to compare and validate the developed model with experimental data and other studies, the Weibel idealized trachea was reconstructed from G0 to G4. The understanding of the transport characteristic of the particle can be benefit in the design of aerosol drug delivery device which will promote the development of the inhaled aerosol.

The Mathematical model

There are two fundamental approaches in the CFD analysis of the fluid flow, the Euler-Euler approach and Euler-Lagrangien approach. In this study, the Euler-Lagrange approach was used which solved the particle trajectory using equations of the motion for each individual particle. The volume fraction of the particles is not included in the continuous phase. As the aerosol particle considered in this study is small in volume,

the volume fraction of the particle was quite low which was reasonable for not included in the continuous phase.

Computational model

To study the gas and particle conduction, the human lower respiratory tract was selected from generation 0 (G0) to generation 4 (G4). In this study, the Weibel symmetrical model was used to construct the computational domain. The model was created in commercialized computer aided design software, Ansys Design modeler, which will further be used in computational fluid dynamics calculation. Figure 4.1 shows the first four generation of the Weibel symmetrical trachea. The detailed parameters are shown in Table 4.1

Table 4.1 *The Weibel symmetrical model parameters*

Generation	Diameter (mm)	Length (mm)
G0	18.0	120.0
G1	12.2	47.6
G2	8.3	19.0
G3	5.6	17.6
G4	4.5	12.7

Figure 4.1 *The idealized trachea model*

Weibel symmetrical trachea was meshed using ANSYS Mesher. The meshes were divided with the number of cells in the range of 150,000-400,000 elements. The meshes were tested for the grid independence of the computed result. The geometry using in this study had 1 inlet at the top of the trachea, and 16 outlets at the end of fourth generations. Each generation of the respiratory tree was marked to identity the amount aerosol particle deposited. The flow governing equations were applied with finite volume method. The unsteady-state solution was solved for the flow field which assumed to have a convergence criterion of the residual less than 10^{-4}. Air was considered as the main fluid of this system which assumed to be incompressible Newtonian fluid. (constant density, viscosity, and fluid static pressure) The governing equations are expressed as follows:

Continuity equation

$$\frac{\partial \rho}{\partial t} + \nabla \cdot (\rho \vec{u}) = 0 \tag{4.1}$$

Momentum equation

$$\frac{\partial \rho \vec{u}}{\partial t} + \nabla \cdot (\rho \vec{u} \vec{u}) = -\nabla p + \nabla \cdot (\bar{\bar{\tau}}) + \rho \vec{g} \tag{4.2}$$

$$\bar{\bar{\tau}} = \mu [(\nabla \vec{v} + \nabla \vec{v}^T) - \frac{2}{3} \nabla \cdot \vec{v} \bar{\bar{I}}] \tag{4.3}$$

where *I* is the unit tensor and *t* is the current flow time. The Brownian motion can be neglected in the study as the size of the aerosols are in micrometer size [39,40]

Particle transport theory

Particle transport model is the sub model of multiphase model, where the particles are all tracked in the whole domain using Lagrangian method, rather than being modeled as an additional phase in Eulerian method. The aerosol phase is modeled by a sample of individual aerosol particles. The tracking is conducted by forming the set of ordinary differential equations for each particle. These set of equations are equations for their position, velocity, temperature, and mass, which are then integrated to calculate the behavior of the particles.

Individual particles are tracked from the injection point which is an inlet of the domain until they escape out of the domain or collide to the domain wall. Every time particle is injected, the source terms are generated to the fluid mass and momentum equations in order to couple with continuous fluid. The particle displacement is determined using forward Euler integration of the particle velocity as expressed:

$$x_p^n = x_p^o + U_p^o \delta t \qquad (4.4)$$

$$\left(\frac{dx_p}{dt}\right) = U_p \qquad (4.5)$$

where, U_p^o is the initial particle velocity. The superscript o and n are referred to old and new values, respectively. The forward integration of the particle aerosol is calculated then at the end of the timestep, the new particle velocity is determined using the particle momentum equation as given:

$$m_p \left(\frac{dU_p}{dt}\right) = \sum F \qquad (4.6)$$

where $\sum F$ is the summation of the forces acting on the particle. The particles are discretely travel in a continuous fluid medium which the acceleration of the velocity by multiple sources of force, for instance, the difference in particle and fluid velocity, displacement of the fluid by the particle, etc. The Eq 4.6 can be expanded as:

$$m_p \left(\frac{dU_p}{dt}\right) = F_D + F_g \qquad (4.7)$$

In this study, only two forces are included in the model. F_D, and F_g are the particle drag force and the force due to gravity, respectively. U is the fluid velocity.

The drag force per unit particle mass is expressed as:

$$F_D = \frac{18\mu}{\rho_p d_p{}^2} \frac{C_D Re_r}{24} \qquad (4.8)$$

Where μ is the dynamic viscosity of the fluid, ρ_p is the density of the particle, and d_p is the particle diameter. The relative Reynolds number (Re_r) is defined as:

$$Re_r = \frac{\rho d_p |U_p - U|}{\mu} \tag{4.9}$$

The Schiller Naumann drag model for the drag force between the particles and the fluid is described as

$$C_D = \frac{24}{Re_r}(1 + 0.15 Re_r{}^{0.687}) \tag{4.10}$$

The sphericity (Ψ) calculation is used to interpret the aerosol particle shape into the model which refers to the ratio of the surface area of the sphere to the surface area of the particle. It is defined as:

$$\Psi = \frac{\pi^{\frac{1}{3}}(6V_p)^{\frac{2}{3}}}{A_p} \tag{4.11}$$

where V_p is the volume of the aerosol particle, and A_p is the surface area of the particle.

Boundary conditions

The top of the domain was considered as the trachea inlet which the air and aerosol were fed in. The inlet air velocity was given as sinusoidal function as:

$$v = \frac{Q}{A}\sin(2\pi f t) \tag{4.12}$$

where Q is the volumetric flow rate, A is the cross-sectional area, f is breathing frequency, and t is current flow time. The aerosol particle velocity was set equal to the air. The normal average human flow rate of (30 L/min) and normal breathing frequency (15 breaths per minute) were chosen for this study. The amount of particle fed in the system was set to 10 microgram per cubic meter of air flow. The particle properties including particle size, particle density, and particle shape were the considered parameters.

As air and particle flew along the tract, their momentum transfer to the trachea wall was governed by particle-wall interaction model which expressed by the value of restitution coefficient. In general, the wall of trachea is normally moistened and cover with thin-layer mucus, this study then assumed that every particle that interacted with the wall would be collected on that local site. Thus,

the tracking of the particle was terminated. To stop the motion of the collided particles, the coefficient of restitution in parallel and perpendicular direction were set to 0.

The outlet was assumed as the average pleural pressure which was lower than the atmospheric pressure to represent the inhalation. The particles that reached this boundary, they escaped from the domain and eventually stopped being tracked. The total accumulated mass and total mass escaped from the domain was recorded for further analysis.

The statistical analysis

The effect of aerosol properties on the deposition of the aerosol particles were evaluated using three-level (3^k) factorial experimental design method. The studied factors were the properties of the aerosol including aerosol diameter, aerosol density, and the aerosol shape which was represented by the sphericity of the aerosol. These factors were coded from, A, B, and C, respectively. Table 4.2 shows all the factors with their coded symbol, unit, and levels. The factor levels were shown in coded symbol, 1, 0, and -1, representing high level, medium level, and low level, respectively. The experimental design was varying to capture the interaction effects by interpreted with all the combinations of the factor levels which yielded the total number of 27 runs.

The corresponded level of the diameter was chosen from their practical range of that of aerosol particles which was from 1 to 10 microns. The chosen density range was broad in order to represent the aerosol as well as the fine dust commonly found in the environment. The sphericity was assumed to be in range of perfect sphere (sphericity = 1) to the value of 0.5. The responses of this study were the deposition percentage of the aerosol and the amount of the aerosol that flew out the system to the deeper generation of the respiratory tree. The deposition percentage (DP) of the aerosol and the aerosol escaped percentage (EP) are defined as

$$DP = \frac{Total\ mass\ of\ particle\ deposited\ to\ the\ wall}{Total\ mass\ injected} \times 100 \qquad (4.14)$$

$$EP = \frac{Total\ mass\ of\ aerosol\ escaped}{Total\ mass\ injected} \times 100 \qquad (4.15)$$

Table 4.2 *Input parameters considered in this study*

Coded Factor	Factor	Unit	Level		
			-1	**0**	**1**
A	Aerosol diameter	μm	1	2.5	10
B	Aerosol density	kg/m^3	900	1,775	2,650
C	Aerosol sphericity	-	0.50	0.75	1.00

The model was implemented in commercial ANSYS CFX solver. The parallel computation was utilized to reduce the computational time. Computations were made with double-precision on a 64-bit machine for better resolution of the micro-scale simulation.

Results and Discussions

Mesh independency test

The mesh independency test was conducted on the meshed trachea geometry (shown in Figure 4.1) to ensure the result accuracy. The mesh independence of the pressure was examined, and the results are plotted in Figure 4.2. The figure shows the pressure profile along the length of the trachea. As the total number of elements increased, the pressure profile converged onto a mesh-independent state. The 300,000 elements mesh was sufficient enough to provide the accurate results. To reduce the computation resources and time needed to complete the calculation, the final converged mesh selected for the study was 300,000 elements.
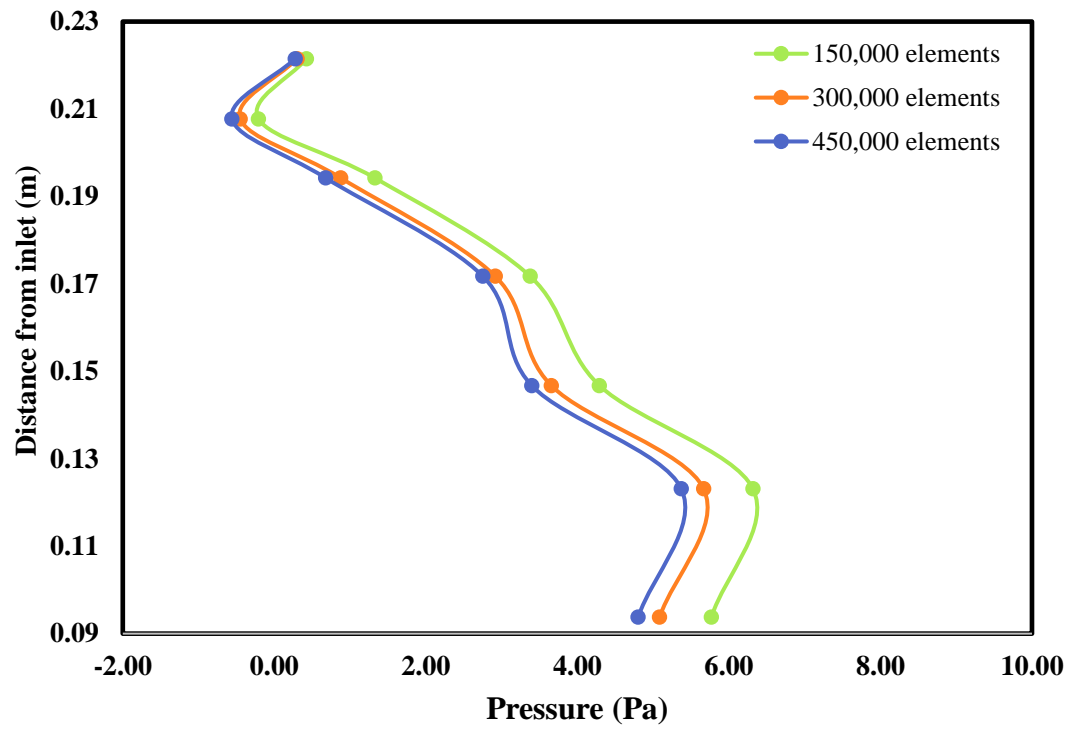
Figure 4.2 Grid independence test
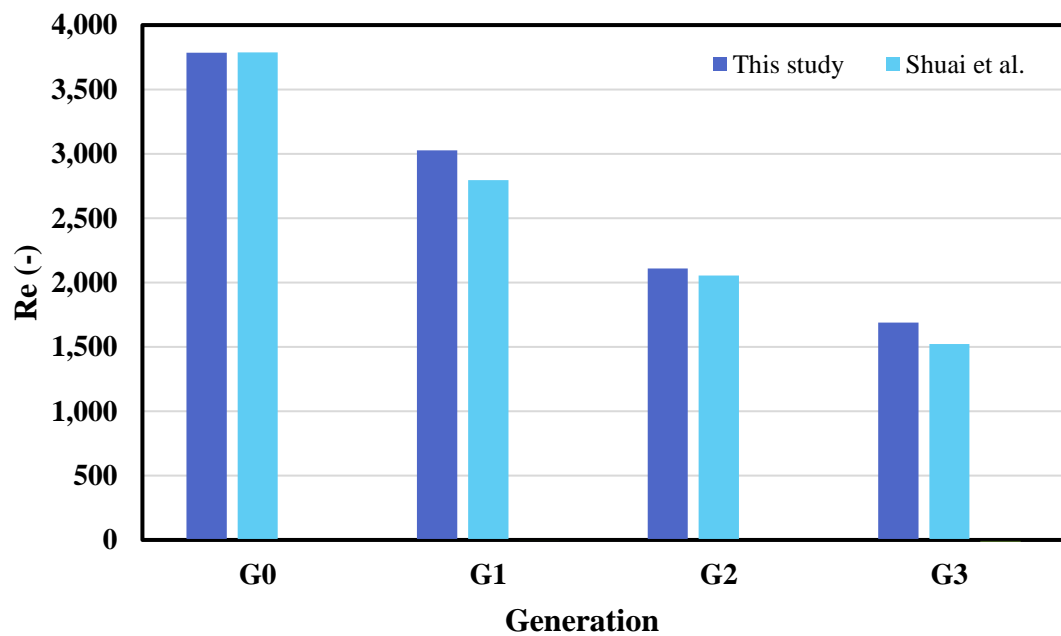
Figure 4.3 Reynolds number of each generation (Q = 50 L/min)
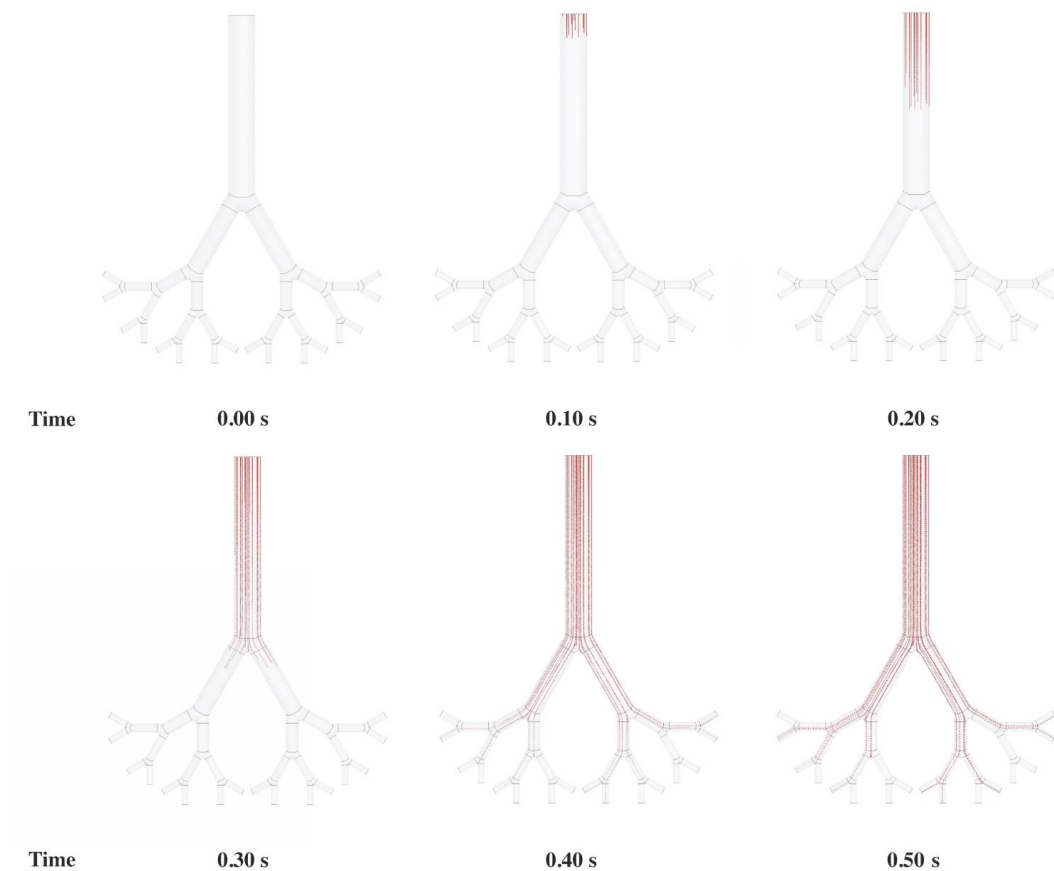
Figure 4.4 *Particle trajectory snapshot from 0 s to 0.5 s.*

Model Validation

The validation was made to ensure the correctness of the model. The flow field was computed using the mathematical model as described in previous section. The results were compared with those of Shuai et al [66]. In order to compare the results, the flow rate was adjusted to match with their experiment. The Reynolds number for each trachea generation was determined. The results are shown in Figure 4.3. The plot showed that the mathematical model using in this study gave adequate prediction of the flow field. The prediction of the early generation was shown only 0.079 percent different.

Preliminary results

Figure 4.4 shows the comparison of the particle trajectory after in various flow time of Run 18 which all of the study factors was set at their medium level. From the beginning, there was no particle in the system. From 0.1 s to 0.5 s, the

trajectory clearly showed that the particles were moving faster in the middle of the flow domain. This was due to the particles were trapped to the wall according to the particle handling condition given at the wall boundary. At 0.4 s, the aerosol particles reached the outlets at the bottom of the fourth generation and started to escape out of the domain. The total mass of the aerosol that escaped the domain was recorded, which implied that the particles were able to penetrate further down to the latter generation of the respiratory tree. Table 4.3 shows all the run combinations with their total mass escape and deposition percentage results. The results showed that Run 13, 17 and 25 had the highest total mass escaped from the flow domain with the value of 2.1305E-11 kg which was 63.77 percent of the total aerosol inhaled. These three runs shared the same configuration except the aerosol sphericity which represents the shape of the aerosol. The sphericity was used to determine the actual diameter of the aerosol which latter used in drag model to evaluate the momentum exchange between the main flow and the particles themselves. It can imply from the results that the particle sphericity might not affect the total particle penetrated deep down the tree. Run 1, 5 and 10 showed the lowest total mass escaped from the flow domain with the value of 1.3355E-11 kg which was 39.98 percent of the total aerosol inhaled. The results were similar to the case with high total mass escaped, the different in sphericity did not affect the particle to escape the domain. The difference between the maximum cases and the minimum cases were the diameter and the density of the aerosol. The group of the highest total mass escaped cases had the low level of both diameter and density configuration, whereas, the lowest total mass escaped cases had the high level of both diameter and density.

The deposition percentage for all cases were evaluated and represented in Table 4.3. The results revealed the same group of runs giving similar trend results. Run 1, 5 and 10 showed the highest deposition percentages of 40.65 percent. The deposition percentage only took account for the aerosol particle that collided to the wall which were not included the aerosol particle that suspended in the air. The fraction was calculated with respect to the total aerosol mass inhaled. These runs shared the same properties except the sphericity. In contrast, run 13, 17, and

25 showed the lowest deposition percentages of all cases with the value of 16.71 percent. The differences between these cases were the diameter and the density of the aerosol.

Figure 4.5 depicted the deposition percentage in each generation of the respiratory tree. The deposition percentage of the aerosol particle in the first four generation (G1-G4) was the highest in cases of 10 μm diameter compared with 2.5 μm and 1 μm. The larger particle size tended to deposit more in the early generations. The plot further confirmed that the smaller particle size tended to penetrate to the deeper generation (>G4). The results were similar with the reported from others [29]. Figure 4.6 depicted the deposition percentage of each generation while varying the aerosol density. The aerosol with high density tended to deposit more in the early generation. The deposition percentage was higher as it was getting deeper. This was because the deeper generation had more child branches resulting in higher contact area which gave higher collision probability for the aerosol. Figure 4.7 depicted the deposition percentage of each generation while varying the aerosol sphericity. The bar graph showed nearly identical. These might imply that the aerosol sphericity might not have an effect to the location of deposition. To interpret the result statistically, the results were then evaluated to determine the significant of the factors using the analysis of variance (ANOVA).

Table 4.3 *The designed experiment with all possible combinations*

Run No.	Factor			Total aerosol escaped		Deposition percentage (%)
	A	B	C	(kg)	(%)	
1	1	1	1	1.3378E-11	40.05	40.6616469
2	1	0	1	1.6703E-11	50.01	30.5266467
3	1	-1	-1	1.8067E-11	54.09	26.4330988
4	1	-1	0	1.9205E-11	57.48	23.0161039
5	1	1	0	1.2078E-11	36.16	44.5276798
6	-1	1	1	2.1291E-11	63.75	16.769089
7	1	0	0	1.5603E-11	46.71	33.8658638
8	0	1	1	2.1085E-11	63.13	17.4159132
9	-1	0	0	2.1296E-11	63.76	16.7572257
10	1	1	-1	1.0333E-11	30.94	49.8258834
11	0	0	-1	2.1090E-11	63.14	17.3627709
12	0	0	1	2.1180E-11	63.40	16.6140923
13	-1	-1	-1	2.1298E-11	63.75	16.7277197
14	-1	1	-1	2.1264E-11	63.65	16.8279692
15	-1	1	0	2.1276E-11	63.69	16.7920098
16	0	-1	-1	2.1210E-11	63.49	16.9876462
17	-1	-1	1	2.1305E-11	63.77	16.705316
18	0	0	0	2.1147E-11	63.30	17.1758575
19	1	-1	1	1.9534E-11	58.47	22.0232729
20	-1	0	1	2.1292E-11	63.73	16.7478689
21	1	0	-1	1.3739E-11	41.12	39.5052532
22	-1	0	-1	2.1281E-11	63.70	16.3541136
23	0	1	-1	2.0905E-11	62.57	17.9004729
24	0	-1	1	2.1241E-11	63.58	16.8951286
25	-1	-1	0	2.1303E-11	63.76	16.7136898
26	0	-1	0	2.1229E-11	63.54	16.9333407
27	0	1	0	2.1025E-11	62.93	17.5402149
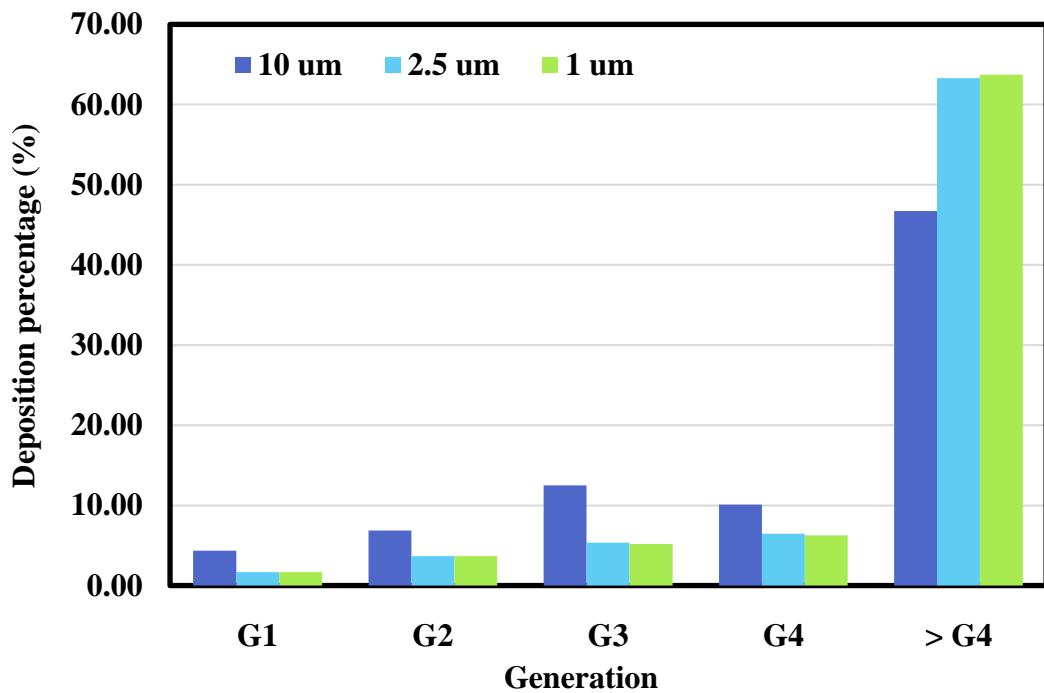
Figure 4.5 *The deposition percentages of each generation for different aerosol diameter*
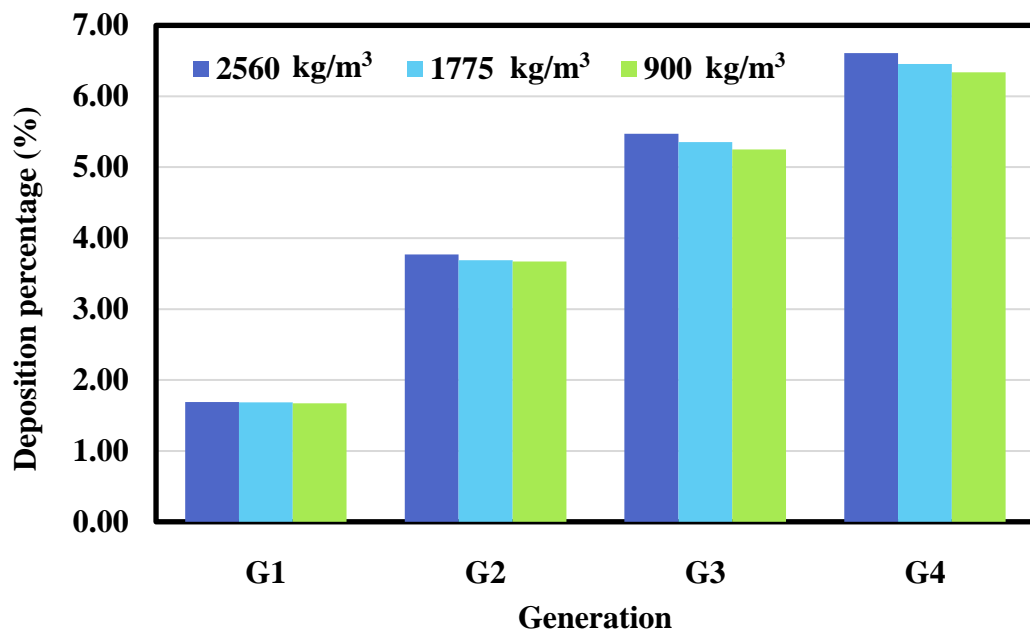
Figure 4.6 *The deposition percentages of each generation for different aerosol density*
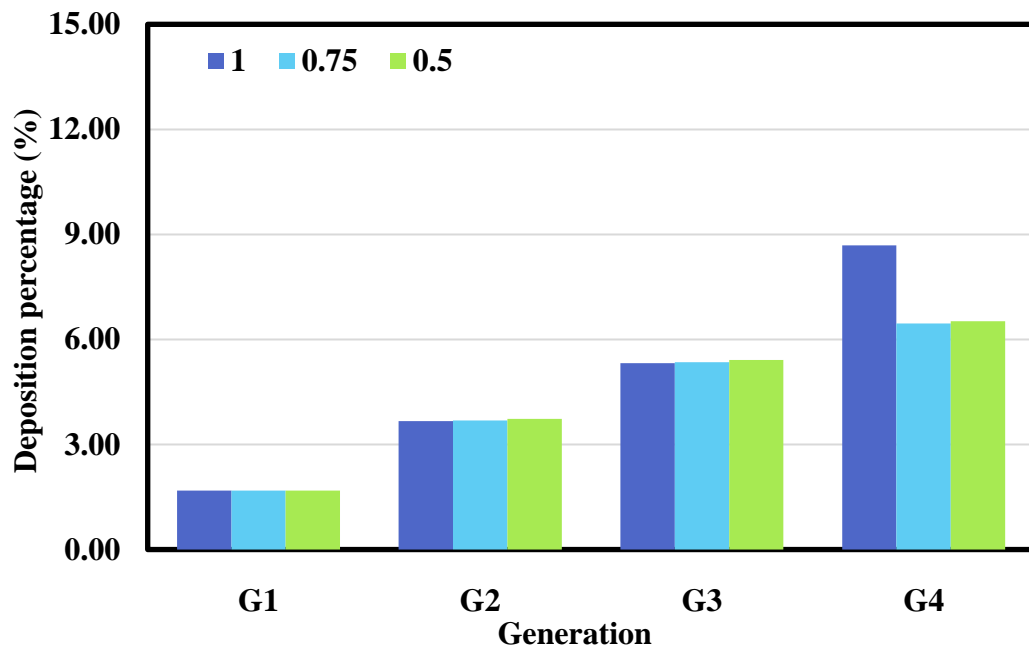
Figure 4.7 *The deposition percentages of each generation for different aerosol sphericity*

Parametric study results

Escaped aerosol percentage

To analyze the significant levels of the factors affecting the escaped aerosol percentage, the study utilized the ANOVA. The analysis results are shown in Table 4.4. At given confidence interval of 95.00%, the p-value of the significant parameter was considered to be lower than 0.05, thus, the analysis confirmed that the aerosol diameter (A), aerosol density (B), aerosol sphericity (C), the interaction between aerosol diameter and aerosol density (AB), the interaction between aerosol diameter and aerosol sphericity (AC) and the quadratic effect of the aerosol diameter (A^2) were the important parameters. The main effect plot of aerosol diameter (A) is shown in Figure 4.8. The aerosol diameter had negative effect on escaped aerosol percentage. The plot shows the maximum escaped aerosol percentage where the diameter level was in between low and medium level. Figure 4.9 shows the main effect plot of aerosol density. The aerosol density

had negative effect on the escaped aerosol percentage. The highest escaped aerosol percentage was found at low level of aerosol density. Figure 4.10 shows the main effect plot of aerosol sphericity. The plot showed slightly higher in escaped aerosol percentage when the aerosol sphericity was increased. The aerosol sphericity lower than one suggested that the particle is not a perfect sphere. The lower the particle sphericity, the higher the aerosol projected surface area, resulted in the lower escaped aerosol percentage. However, the aerosol sphericity had only slightly positive effect on the escaped aerosol percentage.

Figure 4.11 and Figure 4.12 showed the interaction plot and the surface plot which included the interaction effect of aerosol diameter and aerosol density (AB). It was clearly shown that within the range of the study, the escaped aerosol percentage was low when both diameter and density of aerosol particles was high. Figure 4.13 and Figure 4.14 shows the interaction effect plot and the surface plot of the aerosol diameter and aerosol sphericity (AC). The surface plot shows that the lowest escaped aerosol percentage was found when the aerosol sphericity was low and the aerosol diameter was high.

The high diameter, high projected surface area and high density are correlated with the force due to gravity. The particles are pulled down by the gravity force causing them to collide with the wall before it can reach the outlet of G4, resulting in low escaped aerosol percentage. The interaction plot revealed that the relationship between aerosol diameter, aerosol density and aerosol sphericity was depended on each other. At the low level of aerosol density, the escaped aerosol percentage showed negative relationship with the aerosol diameter. The higher the diameter, gave the lower the escaped aerosol percentage. However, for the case of high level of aerosol density, the relationship between diameter and the escaped aerosol percentage changed direction. The plot depicted the positive relationship where the diameter was below medium level, and negative relationship where the diameter was above medium level.

Table 4.4 *Analysis of variance for response 1: The particle escaped percentage*

Source	Sum of squares	Df	Mean square	F-value	p-value
Model	2447.92	9	271.99	40.03	< 0.0001
A-Diameter	1396.04	1	1396.04	205.44	< 0.0001
B-Density	235.33	1	235.33	34.63	< 0.0001
C-Sphericity	30.49	1	30.49	4.49	0.0492
AB	327.51	1	327.51	48.20	< 0.0001
AC	41.18	1	41.18	6.06	0.0248
BC	2.32	1	2.32	0.3414	0.5667
A²	414.28	1	414.28	60.96	< 0.0001
B²	0.0206	1	0.0206	0.0030	0.9567
C²	0.7470	1	0.7470	0.1099	0.7443
Residual	115.52	17	6.80		
Cor Total	2563.44	26			
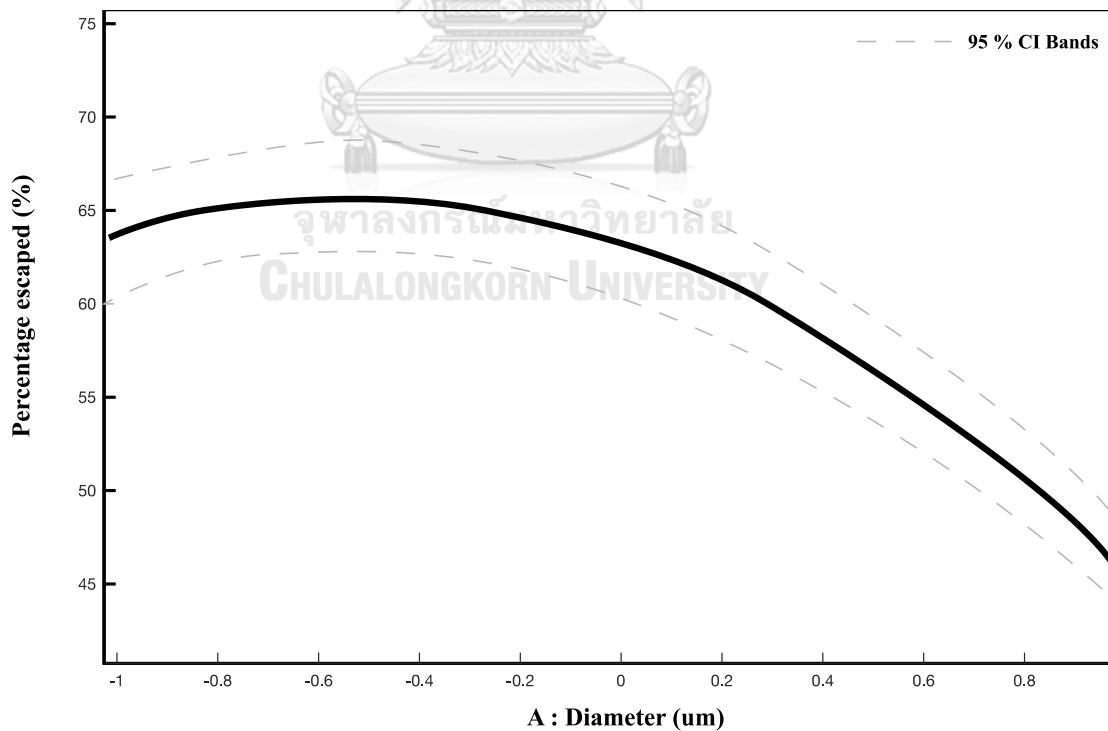
Figure 4.8 *Main effect plot of aerosol diameter on the particle escaped percentage*

Figure 4.9 *Main effect plot of aerosol density on the particle escaped percentage*

Figure 4.10 *Main effect plot of aerosol sphericity on the particle escaped percentage*
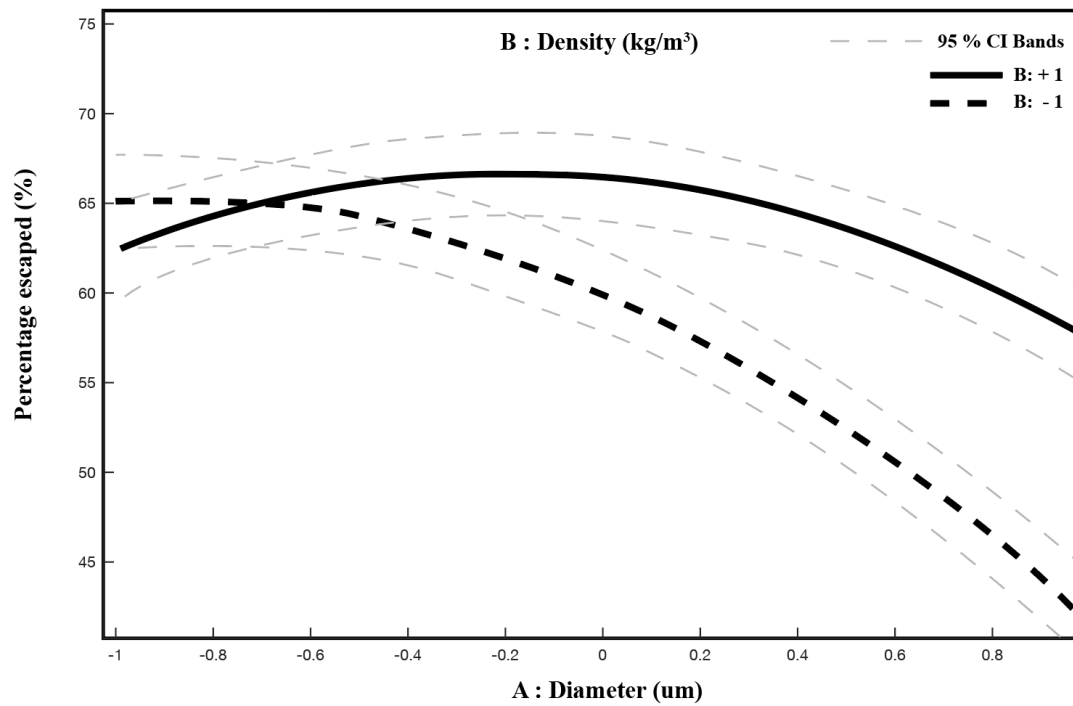
Figure 4.11 The interaction plot between factor A and B

Figure 4.12 The surface plot of particle escaped percentage between A and B
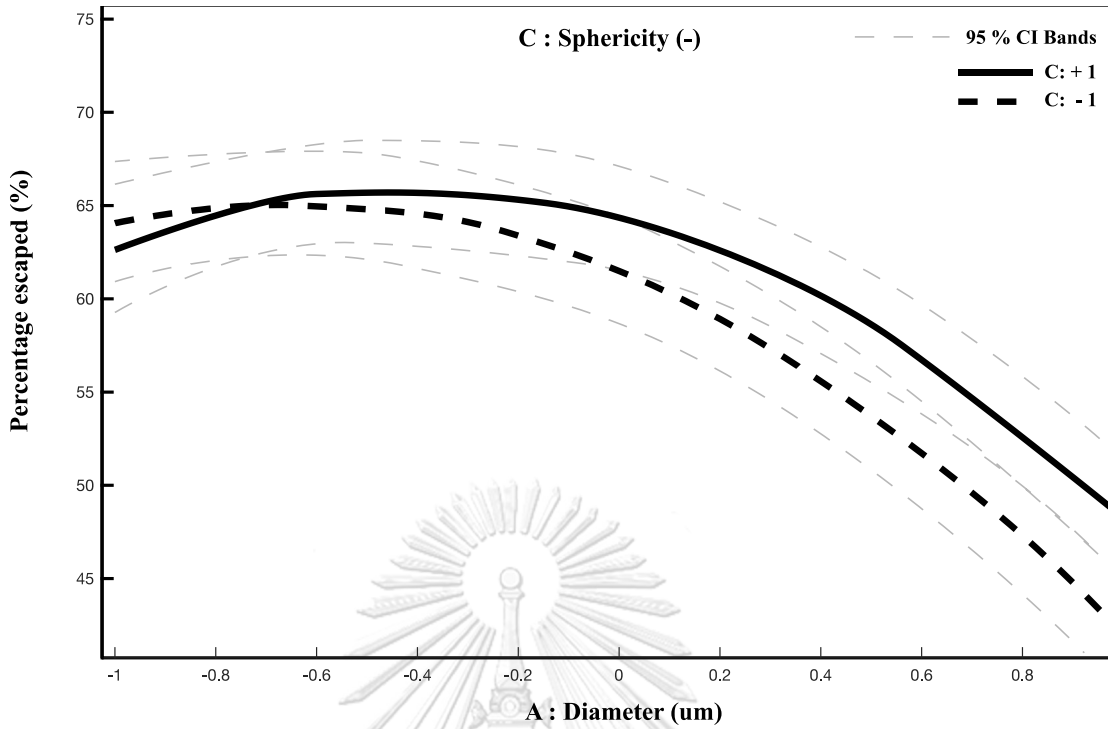
Figure 4.13 *The interaction plot between factor A and C*
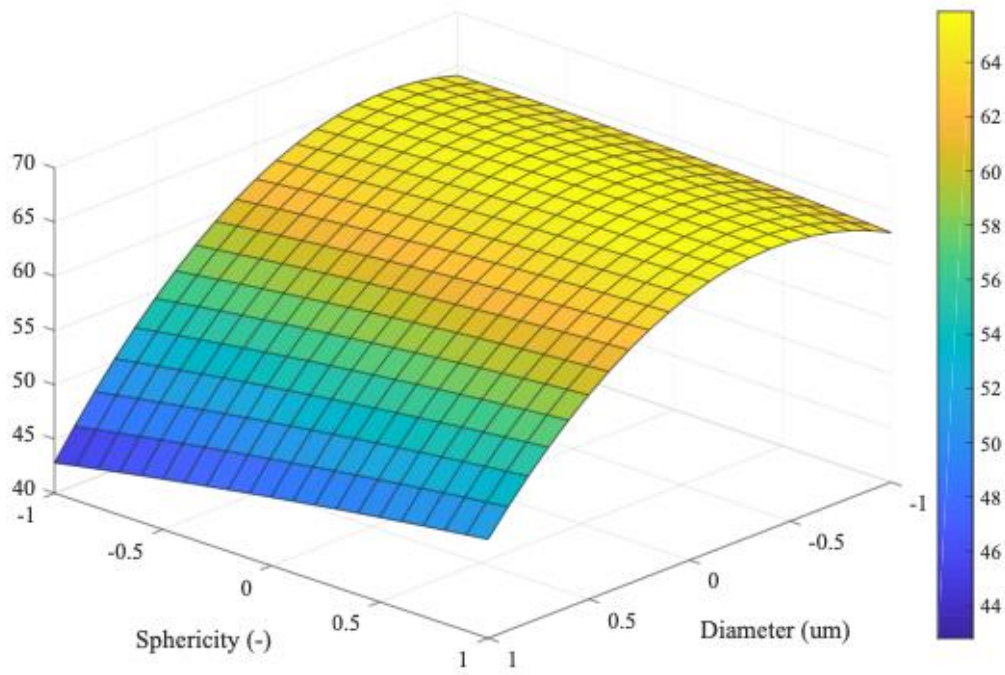
Figure 4.14 *The surface plot of particle escaped percentage between A and C*

Table 4.5 *Analysis of variance for response 2: The deposition percentage*

Source	Sum of squares	Df	Mean square	F-value	p-value
Model	2496.91	9	277.43	40.39	< 0.0001
A-Diameter	1422.05	1	1422.05	207.05	< 0.0001
B-Density	240.72	1	240.72	35.05	< 0.0001
C-Sphericity	30.85	1	30.85	4.49	0.0491
AB	333.91	1	333.91	48.62	< 0.0001
AC	43.57	1	43.57	6.34	0.0221
BC	2.24	1	2.24	0.3259	0.5755
A²	422.97	1	422.97	61.58	< 0.0001
B²	0.0142	1	0.0142	0.0021	0.9642
C²	0.5891	1	0.5891	0.0858	0.7732
Residual	116.76	17	6.87		
Cor Total	2613.67	26			

Deposition percentage

The analysis of variance (ANOVA) results for the effects of the factors on the deposition percentage are shown in Table 4.5. At the same given confidence interval of 95.00%, ANOVA table indicated the aerosol diameter (A), the aerosol density (B), the aerosol sphericity, the interaction of the aerosol diameter and density (AB), the interaction of the aerosol diameter and sphericity (AC), and the quadratic effect of aerosol diameter (A^2) had significant effect on the deposition percentage. Figure 4.15 shows the main effect plot of the aerosol diameter (A). The increased of aerosol diameter resulted in the increasing of deposition percentage. Mathematically, the diameter was accountable in the drag force acting on the aerosol particle and the gravitational force. The higher the diameter, the drag force decreased (d_p is in reverse relationship with drag force as represents in Eq 4.8.) As the aerosol particles were assumed to have constant density, the increasing in aerosol diameter resulted in the increased in particle volume which directly proportional to gravitational force causing the particles to get pulled downward. The gravitational force played an important role on the particle movement as its combined with the force from the inhaled air. The particles accelerated and directly hit the wall at the Y-

junction of the bifurcation yielding high deposition percentage of the aerosol particles. Figure 4.16 shows the main effect plot of the aerosol density. The higher the aerosol density, more particles were deposited on the wall. The higher aerosol density denoted that the particle had higher mass, which had higher gravitational force acting on the particle. The effect was similar to that of the aerosol diameter. The sphericity is related to the aerosol projected surface area. The decreasing of aerosol sphericity denoted the higher in projected surface area which the main effect plot is shown in Figure 4.17.

The interaction effect of the aerosol diameter and density (AB) was also significant. The interaction plot is shown in Figure 4.18. At both medium level and high level of the aerosol density, the aerosol diameter had positive relationship with the deposition percentage. The effect showed the opposite relationship when the aerosol diameter was below its medium level. Figure 4.19 shows the surface plot of the interaction of these two factors. It was clearly shown that the maximum deposition percentage was found when both aerosol diameter and aerosol density were high.

The interaction effect of the aerosol diameter and sphericity (AC) was plotted in Figure 4.20. While the aerosol diameter was at its low level, the sphericity showed small positive effect on the deposition percentage. On the other hand, the aerosol sphericity showed strong negative effect on the deposition percentage.
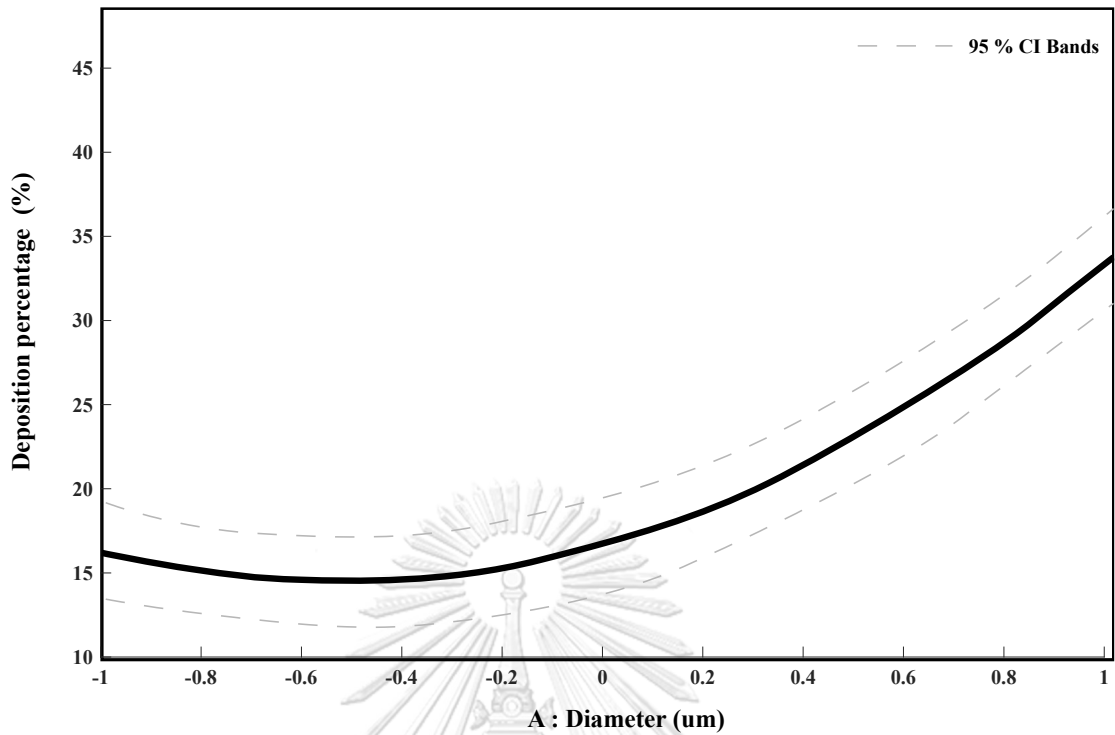
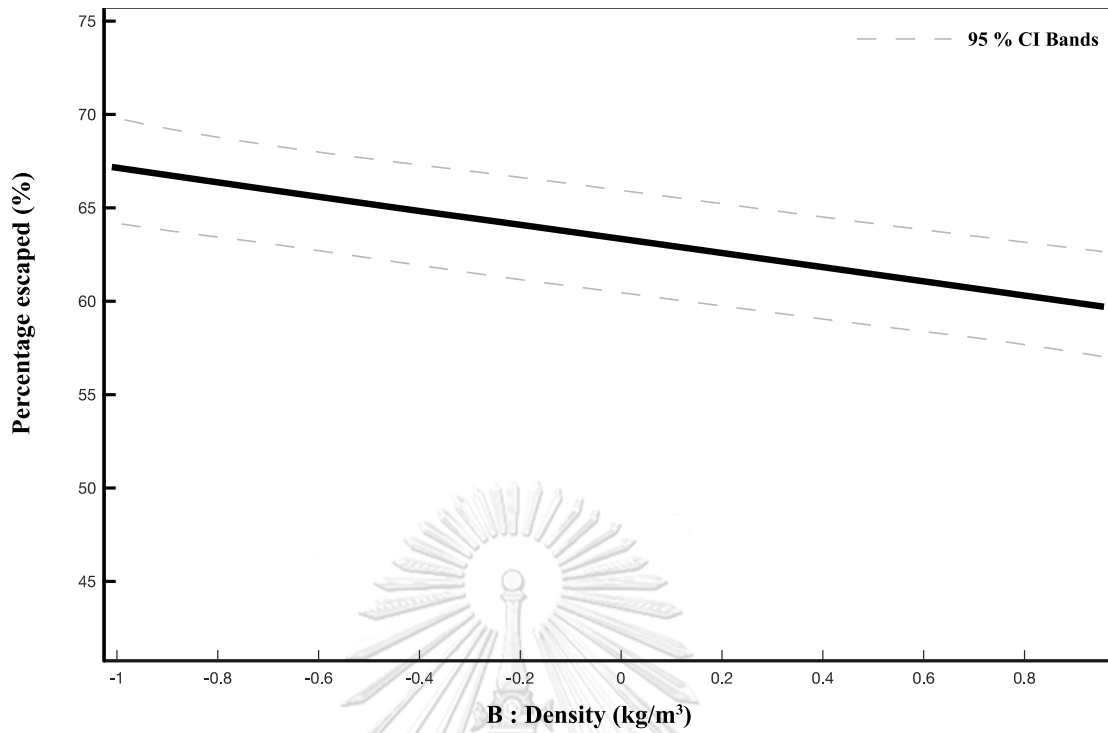**Figure 4.15** *Main effect plot of aerosol diameter on the deposition percentage*
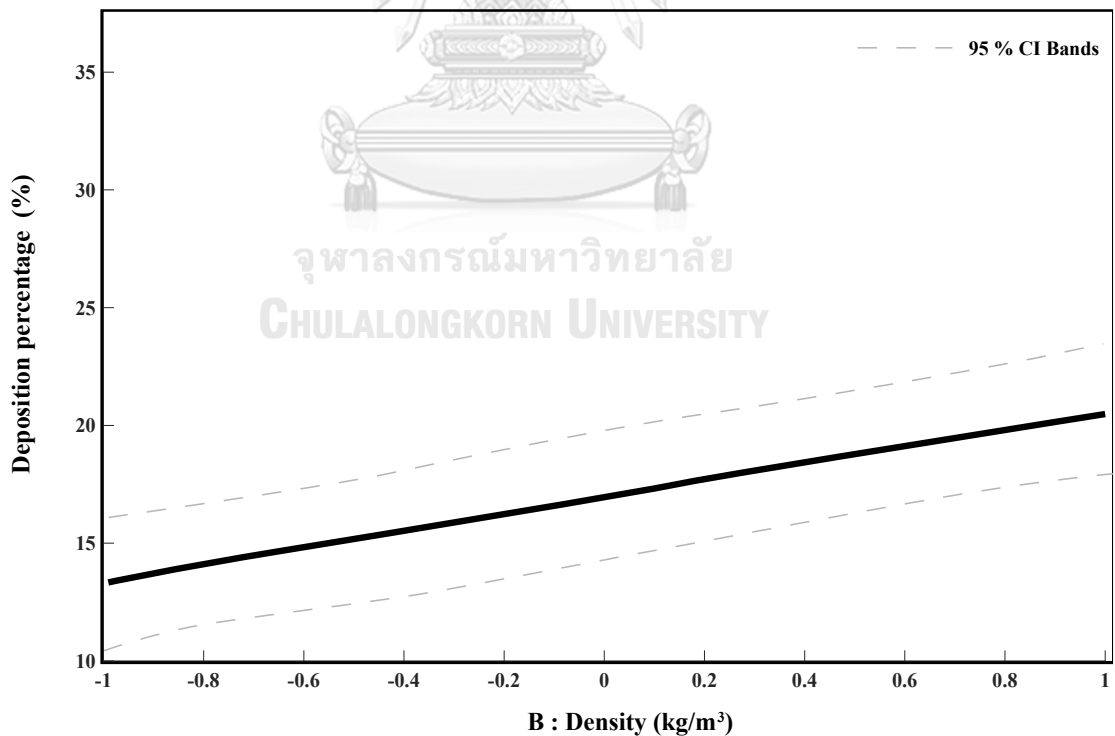
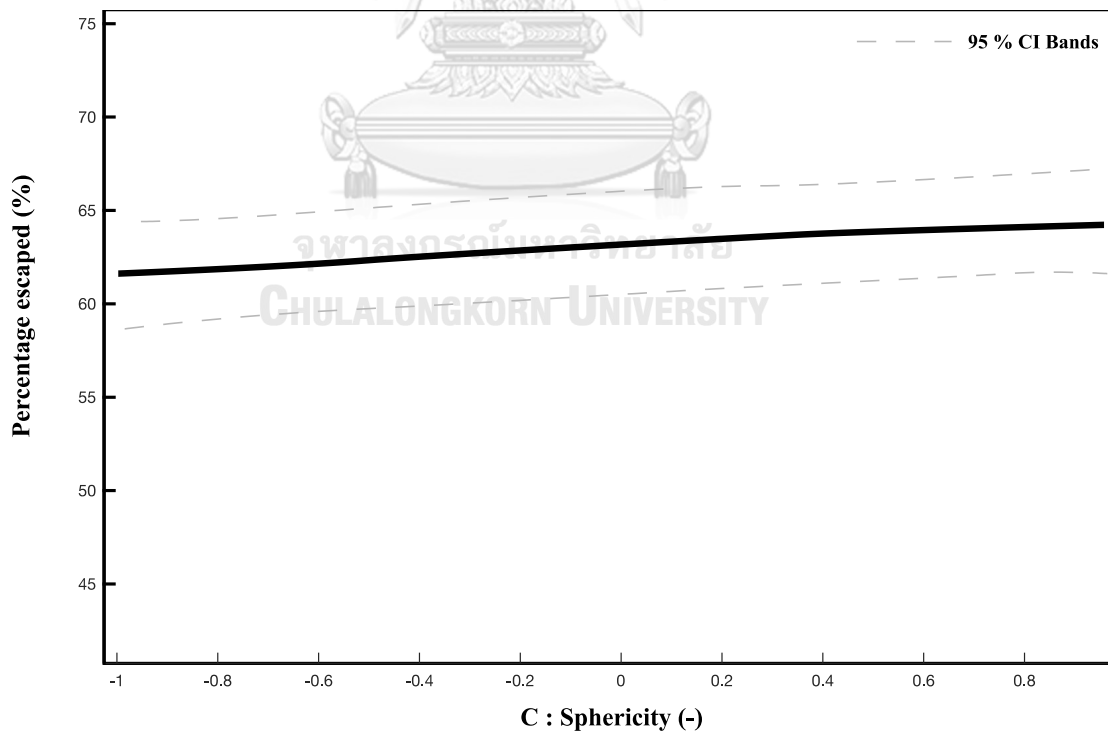**Figure 4.16** *Main effect plot of aerosol density on the deposition percentage*
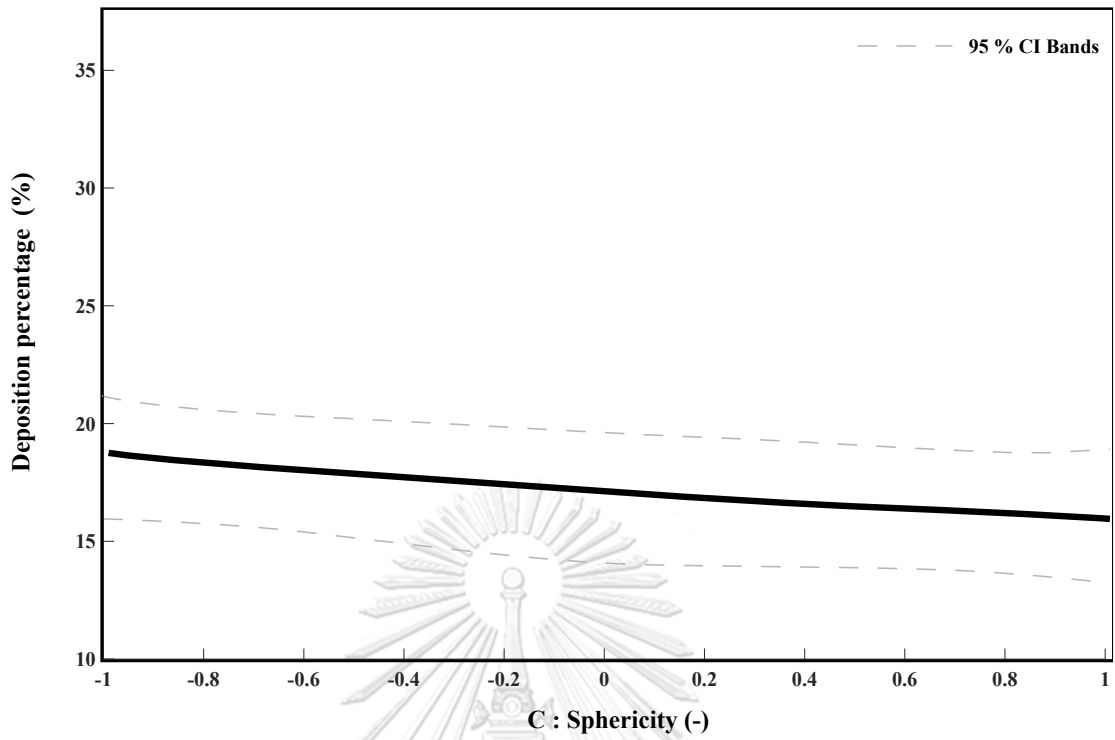
Figure 4.17 Main effect plot of aerosol sphericity on the deposition percentage
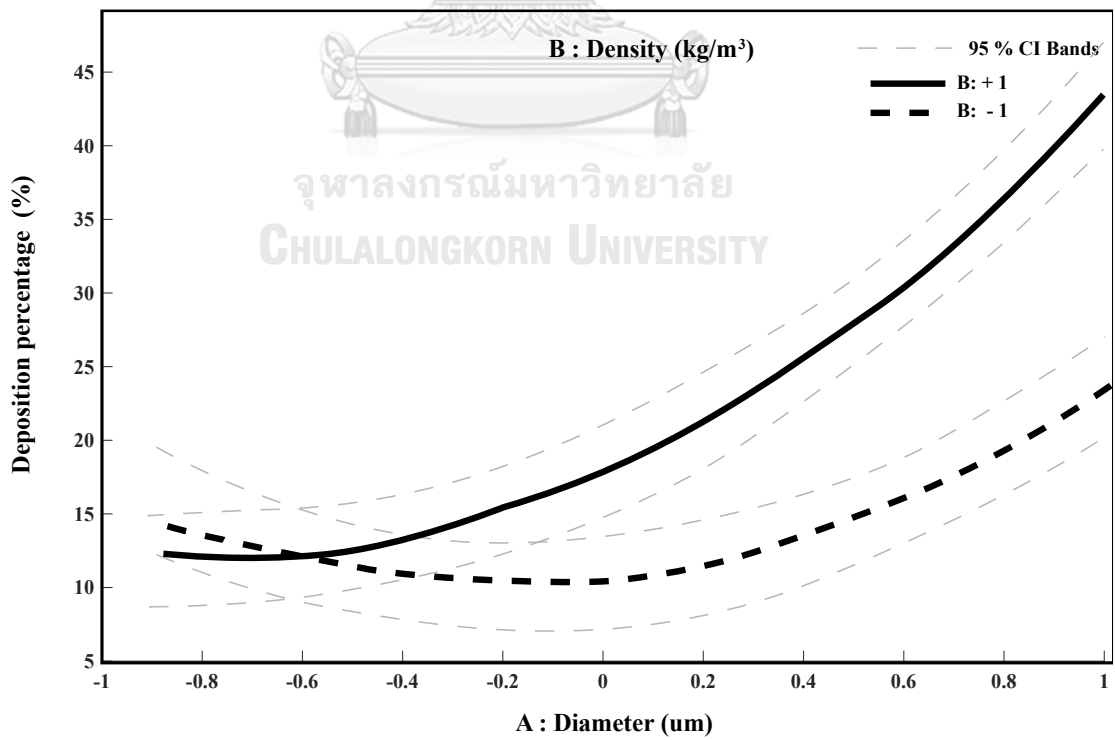
Figure 4.18 The interaction plot between B and C

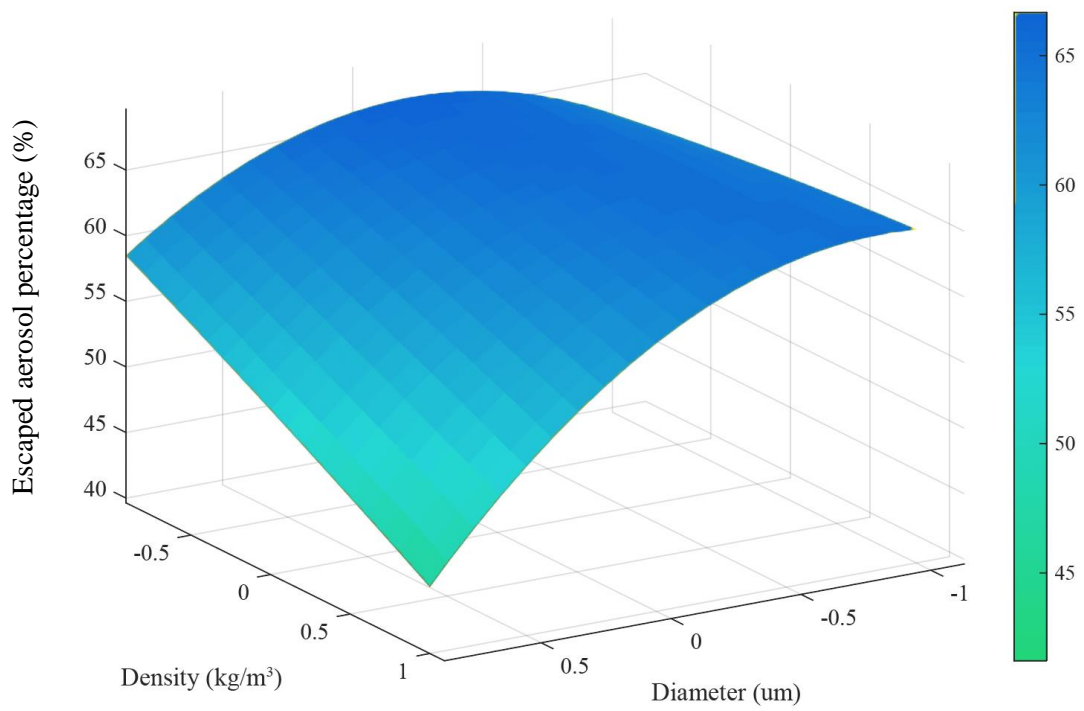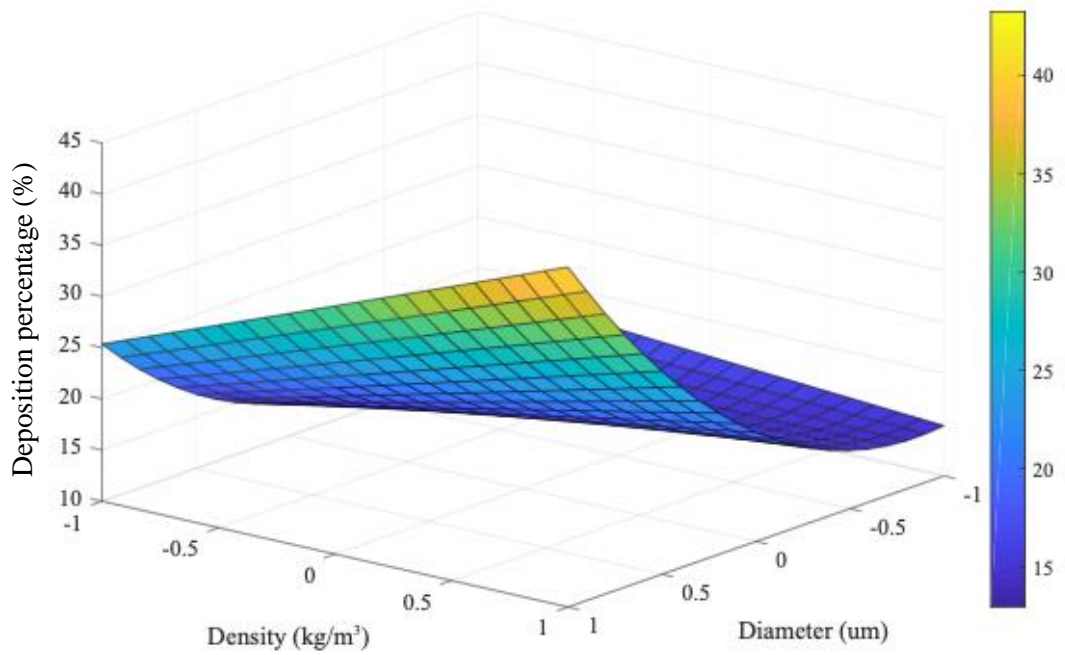***Figure 4.19*** *The surface plot of deposition percentage between A and B*
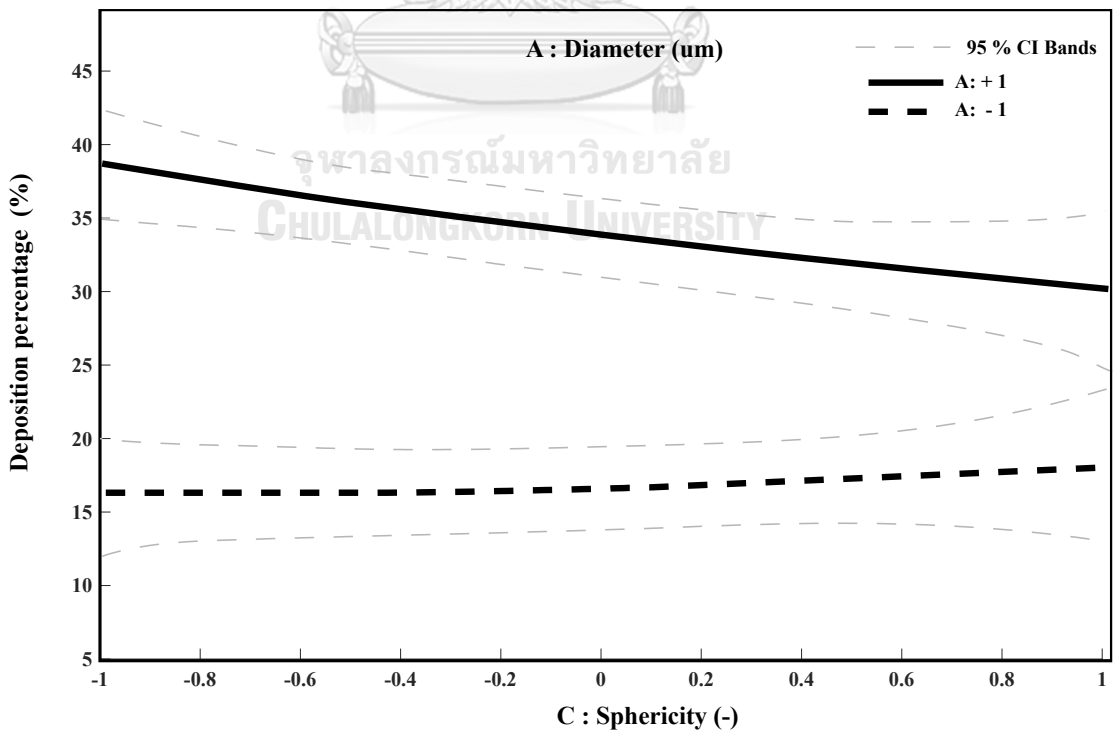
Figure 4.20 *The interaction plot between B and C*
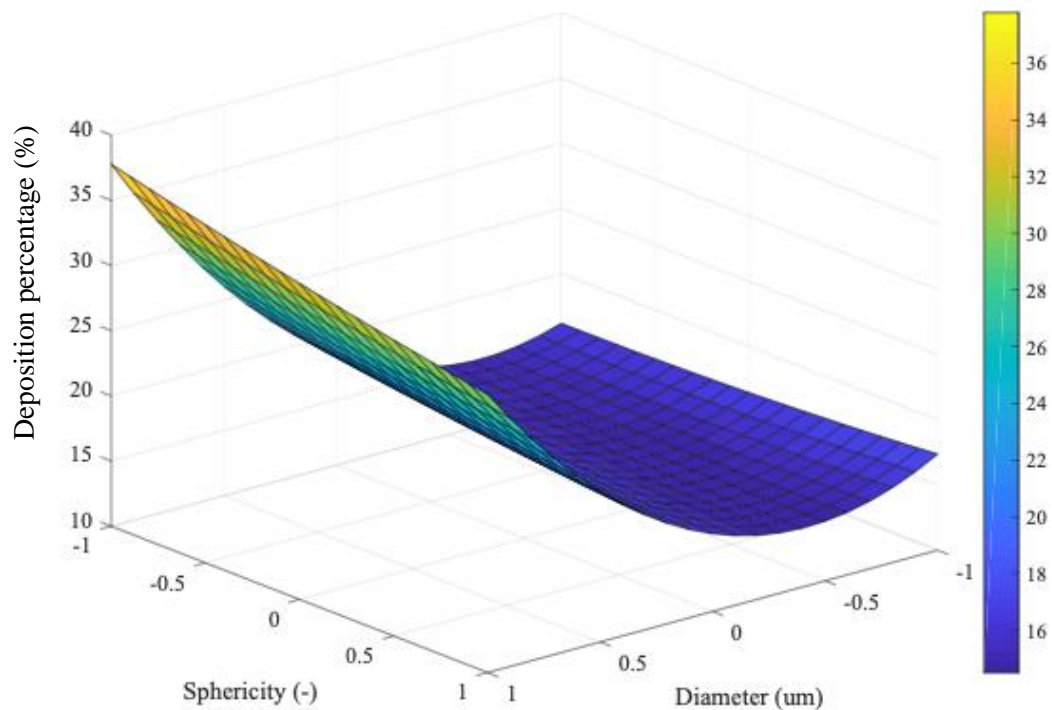
Figure 4.21 *The surface plot of deposition percentage between A and C*

Conclusion

The three-dimension computational fluid dynamics model of the Weibel's idealized trachea model from 0 to 4 generations was investigated. The particle transport theory was utilized to track the particle trajectory. The model was implemented and simulated in ANSYS CFX. The results from the model were compared and validated with experimental data from Shuai et al [66]. The model was extended to statistically investigate the effect aerosol properties on the escaped aerosol percentage and the aerosol deposition percentage. Three more aerosol properties were selected for the study including aerosol diameter, aerosol density, and aerosol sphericity. The 3^k factorial experimental design method was employed. The results could be concluded as:

- Aerosol diameter (A), aerosol density (B), aerosol sphericity (C), the interaction between aerosol diameter and aerosol density (AB), the interaction between

aerosol diameter and aerosol sphericity (AC), and the quadratic effect of the aerosol diameter (A^2) were identified as the important factors affecting the aerosol escaped percentage.

- Aerosol diameter had negative effect on the escaped aerosol percentage. Small aerosol diameter penetrated deeper causing it to escape more than the particle with large diameter.
- Aerosol density had negative effect on the escaped aerosol percentage. The high-density aerosol collided more to the wall, resulting in less particle escaped the domain.
- Aerosol sphericity had slight positive effect on the escaped aerosol percentage.
- The surface plot suggested that within the range of study the escaped particle percentage was lowest when both aerosol diameter and aerosol density were high while the aerosol sphericity was low.
- Aerosol diameter (A), aerosol density (B), aerosol sphericity (C), the interaction between aerosol diameter and aerosol density (AB), the interaction between aerosol diameter and aerosol sphericity (AC), and the quadratic effect of the aerosol diameter (A^2) had significant effect on the deposition percentage.
- Both aerosol diameter (A) and aerosol density (B) had positive effect on the particle deposition percentage.
- The maximum deposition percentage was found when both aerosol diameter and aerosol density were high while the aerosol sphericity was low.

The understanding of the effect of aerosol properties was served as a guideline for the aerosol drug design industries. The identified factors could provide valuable guidance to the pharmacist to increase an efficiency of the aerosol drug design in targeted treatment specified to the patient as a part of precision medicine. However, the model was done based on the idealized model. The forces and interactions model were limited which could be improved in the future study for better representation of the flow phenomena.

CHAPTER V

CFD APPLICATION IN CIRCULATORY SYSTEM:

Effect of transport parameters on atherosclerotic lesion growth:

statistical experimental design analysis

This chapter presents the application of computational fluid dynamics in circulatory system. The effect of transport parameters are studied which may cause the atherosclerotic lesion growth. Firstly, to give an overview of the disease, Atherosclerosis is categorized as cardiovascular disease. As the inflammation of the degenerated arteries starts, they are likely to restriction the blood flow to the other parts of the human body resulting in severe complications. This can happen in any arteries including in the brain, heart, and kidney, etc. The lesion from the inflammatory artery may develop then cause the accumulation and permeation of the macromolecules, including low-density lipoprotein (LDL) and other substances, into the arterial wall [67–69]. Over time, the wall becomes thicken and harden which make the arteries to become narrower. This restricts the oxygenated blood to flow to the other organs. The physical properties of the wall also change according to the inflammation [70]. The arteries may lose their flexibility which can potentially lead to the ruptures of the arteries. This blockage can be life threaten if the forming is located at the major organs, brain, or heart, resulting many serious symptoms including stroke, heart failure, etc [71].

The stage of lesion development is complicated. Many researchers proposed that the area where the LDL was deposited in the artery was correspond to the local elevation of the LDL concentration [72,73]. On the early stage of development, the LDL was found to be highly accumulate in the intima region where it was abnormally enlarged. In addition, the wall shear stress was also noted to reveal the atherosclerosis lesion formation location [74]. The reduction of artery diameter showed higher wall shear stress value due to its increasing of flow velocity. Besides, the accumulation of LDL macromolecules was found behind the plaque where recirculation of the flow was found which appeared to be low in those location [75]. Previously, report from various studies suggested that the shape of endothelial cells near the wall were affected by the flow

field nearby that location which was represented by the value of wall shear stress. The hydraulic conductivity and the permeability of the endothelial cell layer were also responded to the wall shear stress [76–79].

The development of the computer simulation in this field has been rapidly advanced. In the early stage of development, the blood flow was considered as homogenous with single-layer porous wall model [20]. The multi-layer wall model including endothelium, intima, and media layers, was later introduced for better representation of the arterial wall [23,73,80].

However, recent development of the model has not yet considered the relationship between the wall shear stress and the flow properties. The objective of this study was to investigate the effect of the different fluid properties including blood density, blood viscosity, plasma density, plasma viscosity, and LDL concentration level in the blood on the intima-average LDL concentration level and the LDL coverage area. The axisymmetric geometry was used to investigate the results. Those study parameters were chosen from the practical ranges of normal human adult to find the highest risk factor. The 2^k factorial statistical experimental design was used to find the influence of these parameters.

The Mathematical Model

The coronary artery geometry used in this study is illustrated in Figure 5.1. The multi layers geometry was introduced which consisted of three zones including lumen zone (1.84 mm), endothelium zone (0.001 mm), and intima zone (0.34 mm). The lumen zone was the zone where the blood was mainly flowing in. Blood was considered as incompressible Newtonian fluid. The zone adjacent to lumen zone was endothelium zone and intima zone. These zones were modeled as porous media with additional transport of blood plasma. It was noted that the thickness of endothelium zone and intima zone were much different in size. In this study, the assumption was made to the endothelium zone in order to reduce the computational cost. Given the thickness of endothelium layer as 1 micron. The thickness of endothelium layer was approximately 2 order thinner than that of intima zone, and 3 order than that of lumen zone. It was assumed that the variation within the endothelium zone could be neglected. Thus, the

endothelium zone was assigned as thin layers of 1 micron thickness which had two pseudo interfaces, one on lumen side called lumen-endothelium interface, and on the other side, the endothelium-intima interface. These pseudo interfaces were acted as the data storage to store the scalar values within the endothelium zone.
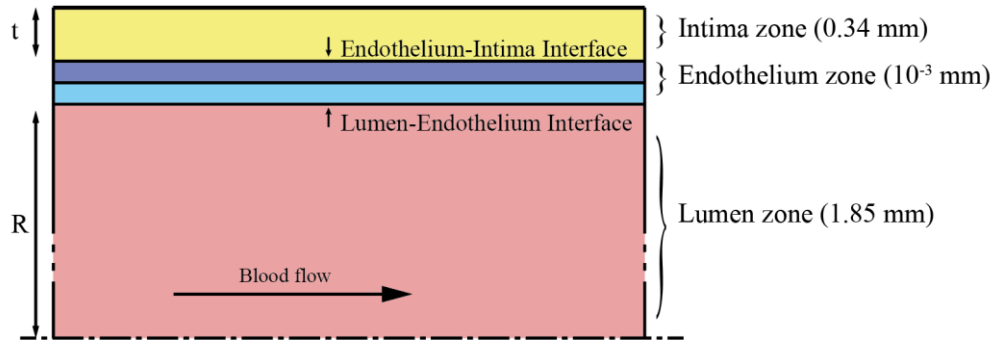
*Figure 5.1 The detailed structure of the three-zone artery geometry
(for illustration, not to scale)*

The blood flow in the lumen zone were governed by steady state Navier-Stroke equation. The mass flowing in the domain also needed to be conserved. The continuity equation and mass conservation are expressed as:

$$(u_l \cdot \nabla)u_l - \mu \Delta u_l + \frac{1}{\rho}\nabla p_l = 0 \tag{5.1}$$

$$\nabla \cdot \rho u_l = 0 \tag{5.2}$$

where u_l, μ and p_l are the blood velocity in the lumen zone, blood viscosity and luminal pressure, respectively. Because blood was considered as incompressible fluid, therefore blood density (ρ) was taken as constant.

In the arterial wall, the endothelium zone and the intima zone were treated differently compared with the lumen zone. The plasma flow was governed by Darcy's law instead. These zones were assumed to be homogeneous porous media.

$$u_w = \frac{\kappa_p}{\mu_p}\nabla p_w \tag{5.3}$$

where κ_p is the arterial wall permeability, p_w is the wall-side pressure, and μ_p is the plasma viscosity. Table 5.1 shows the properties of blood and plasma using in this study which including viscosity and density. The properties were chosen as the studied factors

which acquired from the practical range of normal human adult. The LDL transport, which is the main cause of the plaque formation, is the main consideration of this study. It was governed by the convection-diffusion equation.

$$u_l \cdot \nabla c_l - D_l \Delta c_l = 0 \tag{5.4}$$

where c_l is the LDL concentration in the lumen zone and D_l is the diffusion coefficient of the LDL. For the straightforward representation of the notation, subscript l is denoted as the variable in the lumen zone and subscript w is denoted as the variable in the arterial wall.

The LDL transport in the arterial wall is slightly different compared with that of the lumen zone. The LDL consumption term (r_w) was included to mimic the biochemical reactions. The flow transport also included reflection coefficient (σ_{lag}) which is a measure of the degree to which molecules are retained or reflected by the membrane as expressed:

$$(1 - \sigma_{lag})u_w \cdot \nabla c_w - D_w \Delta c_w + r_w c_w = 0 \tag{5.5}$$

The value of LDL reflection coefficient was proposed by Sun *et al.* [80] as $\sigma_{lag} = 0.8514$. Olgac *et al.* and Prosi *et al.* studied the diffusivity of LDL and proposed the consumption rate of LDL which were taken as $D_l = 5 \times 10^{-12}$, $D_w = 8 \times 10^{-13}$ m/s, and $r_w = 3 \times 10^{-4}$ s^{-1} [20,81].

The membrane permselectivity was governed by three-pore model to determine the flux of solute that will penetrate the endothelium layer. The filtration velocity, J_v is defined by

$$J_v = \frac{\Delta P}{R_{Total}} \tag{5.6}$$

where, ΔP is the pressure difference between the endothelium on the lumen side and media-adventitia interface $\Delta P = p_l^{endo} - p_{adv}$. The pressure at media-adventitial interface was set to be constant at 2333.33 Pa; and R_{Total} is the total flow resistance, which is the summation of the resistance of endothelium cell and intima wall defines as

$$R_{Total} = R_{end} + R_{wall} \tag{5.7}$$

The flow pathways within the endothelium layer is composed of normal junction flow and leaky junction flow, which are parallel of each other. Thus, the resistance from these two pathways can be expressed as

$$\frac{1}{R_{end}} = \frac{1}{R_{nj}} + \frac{1}{R_{ij}} \tag{5.8}$$

where, $R_{nj} = 1/L_{p,nj}$ and $R_{lj} = 1/L_{p,lj}$. Previous literatures suggested that the $L_{p,nj}$ was set to be 8.7009×10^{-12} [m/(s Pa)] [82–84]. The auxiliary equations to calculate the resistances are shown in Eq. 5.9-5.12.

$$L_{p,lj} = \frac{A_p}{S} L_{p,slj} \tag{5.9}$$

$$L_{p,slj} = \frac{w^2}{3\mu_p l_{ij}} \tag{5.10}$$

$$\frac{A_p}{S} = \frac{4w}{R_{cell}} \phi \tag{5.11}$$

$$\phi = \frac{LC \times \pi R_{cell}^2}{\text{unit area}} \tag{5.12}$$

The hydraulic conductivity of the leaky junction pathway ($L_{p,lj}$) is shown in Eq. 5.9. The single hydraulic conductivity of the leaky junction ($L_{p,slj}$) is given in Eq. 5.10. The parameters, w is the half-width of the leaky junction, l_{ij} is the length of the leaky junction, μ_p is the plasma viscosity, R_{cell} is the endothelial cell radius given the value of 15 um, and ϕ is the ratio of the area of leaky cells to the area of all cells. ϕ is correlated to the number of leaky cells (LC), the number of mitotic cells (MC), and the shape index (SI), which eventually derived from the wall shear stress:

$$LC = 0.307 + (0.805 \times MC) \tag{5.13}$$

$$MC = 0.003797e^{14.75 \cdot SI} \tag{5.14}$$

$$SI = 0.380e^{-0.790WSS} + 0.225e^{-0.043WSS} \tag{5.15}$$

$$WSS = \left| \mu \frac{dv}{d\vec{n}} \right| \tag{5.16}$$

where, μ is the fluid viscosity, v is the fluid velocity, and $\vec{n}$ is the unit vector normal to the artery wall. The resistance from the wall was computed from $R_{wall} = \frac{\mu_p t_w}{\kappa}$ where,

t_w is wall thickness and κ is Darcy's permeability of the wall. The total LDL flux, J_s, is described as

$$J_s = P_{app} C_l^{endo} \tag{5.17}$$

where C_l^{endo} is the local LDL concentration in the lumen side, P_{app} is the total apparent permeability of the endothelium. The total apparent permeability is the summation of the permeability of each flow pathway which is defined as

$$P_{app} = P_v + P_{app,nj} + P_{app,lj} \tag{5.18}$$

where $P_{app,lj}$ and P_v are apparent permeability of the leaky junction and permeability of the vesicular pathway; given by Olgac *et al.* [20] as 1.9×10⁻¹⁰ m/s and 1.92×10⁻¹¹ m/s, respectively. $P_{app,nj}$ is the endothelium permeability component of the normal junction. This study assumed that the normal junction pathway could be neglected as the size of LDL was larger than the passage of the solute [78,81], hence, the value of $P_{app,nj}$ was neglected.

The three-zone model was designed to individually solve the flow field in lumen zone and intima zone. The properties of blood and plasma were the study factors. To validate the model results, the data from previous literature was used to validate against. The same simplified axisymmetric artery geometry of Olgac *et al* [20] with 40 percent blockage is shown in Figure 5.2.
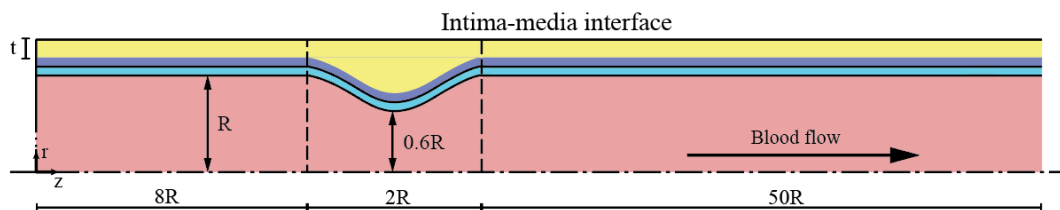
Figure 5.2 *The 40% blockage axisymmetric artery model used in this study (for illustration, not to scale)*

The simplified artery had radius with $R = 1.85$ mm and the intima wall thickness $t = 0.34$ mm. The length of the artery was extended to ensure that the flow to be developed and no disturbance was affected by the outlet. The blood inflow at the inlet boundary was assumed as a parabolic profile and imposed as,

$$u(r) = 2U_0[1 - (\tfrac{r}{R})^2] \tag{5.19}$$

with $U_0 = 0.24$ m/s, taken as the average of the mean velocity of systolic and diastolic [85]. A constant pressure of 9,332 Pa was applied for the outlet. The intima interface with media was set with the constant 2,333 Pa. The filtration velocity (J_v) was calculated by Eq. 5.6 was directly applied to the endothelium interface in the normal direction.

LDL transport boundary conditions

LDL concentration profile was uniformly fed in at the inlet boundary. A Naumann boundary condition of a zero-flux was set to the outlet and intima-media interface. Along the endothelium pseudo interfaces, the LDL flux, J_s was described by convection-diffusion balance equation. Both interfaces are assumed that the mass entering the interface must be consistent with mass going out. Each layer had different value of diffusion coefficient (D). As reported by [23], the LDL flux is defined as:

$$J_s = (1 - \sigma_f)J_v c_i - D \frac{\partial c_i}{\partial x} \tag{5.20}$$

where $D = D_l = 5.0 \times 10^{-12}$ m/s is the diffusion coefficient of LDL in the lumen zone, and $D = D_w = 8.0 \times 10^{-13}$ m/s in the artery wall. $\partial x = 0.5$ μm is the half distance between the two pseudo-interfaces which is half of the endothelium zone thickness. The solute flux in Eq. 5.17 was determined and applied to scalar flux in the normal direction of the pseudo-interfaces.

The mathematical models were implemented in the commercial solver, ANSYS Fluent v18.2. The customized functions were added in to handle the inter-boundary of the pseudo interfaces. Double-precision solver was used for better floating-point accuracy of micro-scale calculation. The SIMPLE algorithm was used for pressure-velocity coupling of the Navier-Stokes equations. The second-order upwind scheme was used for the flow variables and species equations discretization.

Mesh independence test

The artery geometry (shown in Figure 5.2) was divided into several grids of different mesh numbers. The mesh independency test was conducted to ensure the accuracy of the mesh. The test was done under steady-state flow of four meshes with different first-layer element height in a range between 1×10^{-4} μm to 5×10^{-7} μm. The mesh independence of the wall shear stress in z-component was examined on the endothelium interface. The z-component of wall shear stress results are plotted in Figure 5.3.
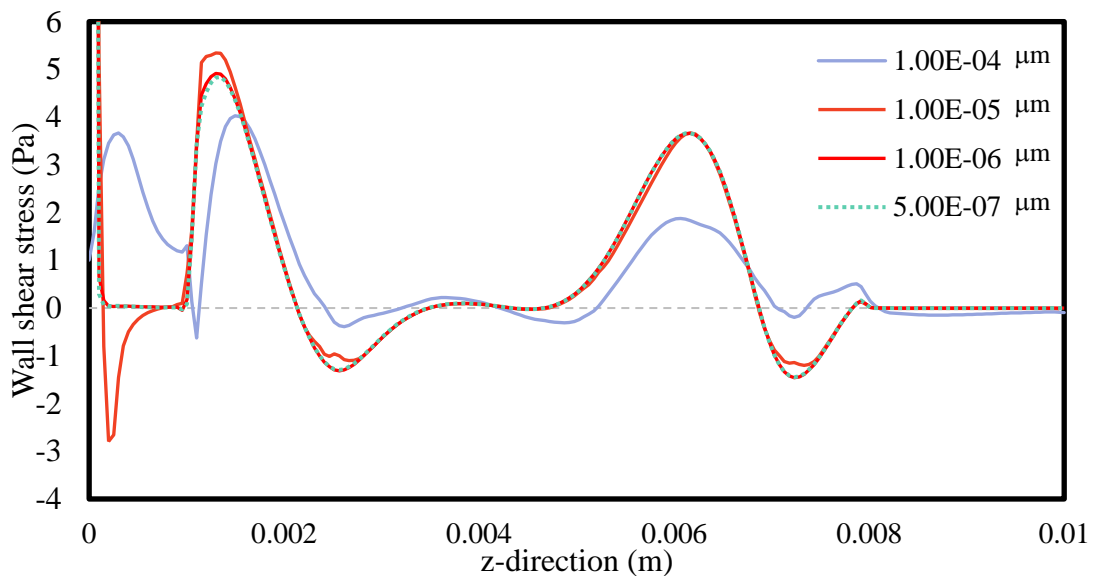
Figure 5.3. *The plot of wall shear stress in z-direction along the normalized span of endothelium interface for varying near-wall cell height*

As the first-layer cell height was decreased. The wall shear stress plot converged onto a mesh-independent state. In the test conditions, the mesh with first-layer cell height of 1×10^{-6} μm was nearly identical to that of the small cell height 5×10^{-7} μm. This result was in agreement with the mesh refinement study of Gabriel *et al* [26]. Thus, the prior was chosen for the rest of the study. The final converged mesh used in the study was 300,000 elements to resolve the local flow phenomena.

The statistical experimental design

The statistical analysis was applied to this study to measure the effect of the flow parameters. The high average intima LDL concentration and high LDL coverage area are unwanted outcomes which are known as the risk factors of the atherosclerotic lesion growth. The effect of these parameters was examined using 2^k factorial experimental design method. It is a systematic approach to design the experiment for the system with one or more input parameters on the output responses with the minimal number of trials. The design is aimed to extract the maximum information from the study by interpreting the number of trials with all possible combinations of the factor level [86,87]. With this varying, the interaction effects which are caused by input parameters are also able to capture.

Table 5.1 *Input parameters considered in this study*

Coded Factor	Factor	Unit	Low Level (-)	High Level (+)
A	Blood Density	kg/m^3	1040	1060
B	Blood Viscosity	Pa.s	0.0025	0.0045
C	Plasma Density	kg/m^3	1000	1035
D	Plasma Viscosity	Pa.s	0.00096	0.00130
E	Inlet LDL Concentration Level	g/ml	0.001	0.002

Table 5.1 shows all study factors in this study including their codes, units, and values in each level. These considered study parameters were blood density, blood viscosity, plasma density, plasma viscosity, and inlet LDL concentration level which were represented in coded form, A, B, C, D, and E, respectively. These factor values were chosen from practical healthy human adult. In fact, these factors were preferably controllable by medical treatment or living manner. The positive sign (+) and negative sign (-) denoted the high level and low level of each factor. The study was replicated with different initial conditions of the pressure with the values of 9,000 and 12,000 Pa, respectively. These initial pressure values were equivalent to the average systolic and diastolic pressure. With the total of 5 study parameters, the total combination of the runs were 64 trials. All the trials are shown in Table 5.2 which also provides the results

of the study responses. The responses of this study were the intima average LDL concentration, and the LDL coverage area on the endothelium interface. The calculation of these two responses are expressed as

$$C_{\text{avg,intima}} = \frac{1}{V}\sum_{i=1}^{n} C_i |V_i| \tag{5.21}$$

where, $C_{\text{avg,intima}}$ is the volume-averaged LDL concentration in the intima zone (mg/ml), C_i is the LDL cell concentration, V is total volume of the intima domain and V_i is individual intima cell volume; and,

$$\text{LDL coverage Area} = 2\pi r A_{\text{coverage}} \tag{5.22}$$

where, A_{coverage} is the LDL deposition coverages area on the surface area of the endothelium and r is the inner radius of the blood vessel. The F-statistic is computed to examine the significance of each individual factorial effect via p-value. [86]
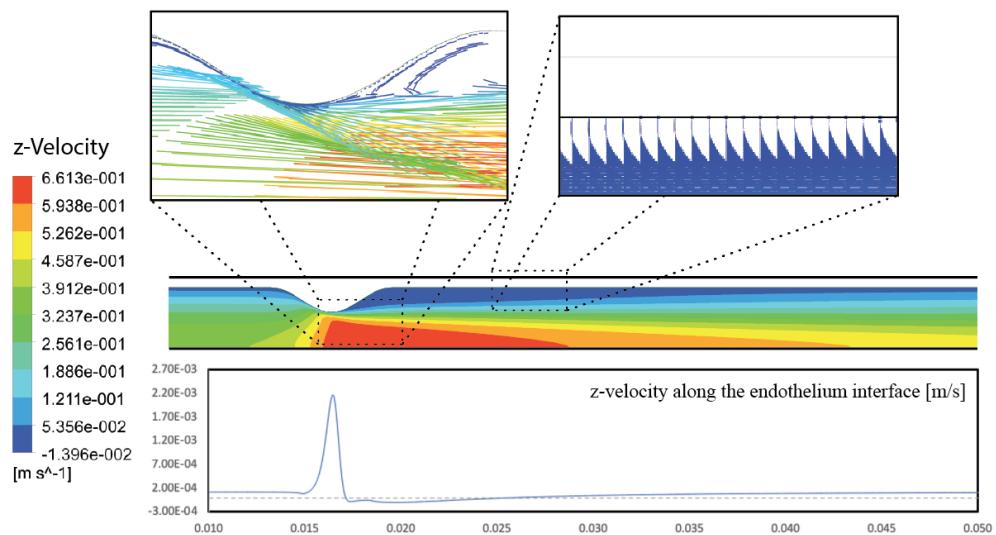
Figure 5.4 The velocity streamline of the flow in the vicinity of the lesion

Table 5.2 *Designed experiment and its results*

Run No.	Replicate	A	B	C	D	E	Intima Average LDL Concentration (mg/ml)	LDL Coverage Area (m^2)
1	1	-	-	-	-	-	0.03523	1.749E-03
2	1	-	-	-	-	+	0.07047	1.629E-03
3	1	-	-	-	+	-	0.03535	1.749E-03
4	1	-	-	-	+	+	0.07071	1.872E-03
5	1	-	-	+	-	-	0.03524	1.749E-03
6	1	-	-	+	-	+	0.07048	1.749E-03
7	1	-	-	+	+	-	0.03540	1.749E-03
8	1	-	-	+	+	+	0.07079	1.749E-03
9	1	-	+	-	-	-	0.01706	7.605E-04
10	1	-	+	-	-	+	0.03411	8.232E-04
11	1	-	+	-	+	-	0.01724	8.107E-04
12	1	-	+	-	+	+	0.03447	7.780E-04
13	1	-	+	+	-	-	0.01706	8.232E-04
14	1	-	+	+	-	+	0.03412	8.232E-04
15	1	-	+	+	+	-	0.01724	8.107E-04
16	1	-	+	+	+	+	0.03449	7.780E-04
17	1	+	-	-	-	-	0.03545	1.800E-03
18	1	+	-	-	-	+	0.07091	1.800E-03
19	1	+	-	-	+	-	0.03557	1.759E-03
20	1	+	-	-	+	+	0.07115	1.606E-03
21	1	+	-	+	-	-	0.03546	1.651E-03
22	1	+	-	+	-	+	0.07092	1.800E-03
23	1	+	-	+	+	-	0.03556	1.606E-03
24	1	+	-	+	+	+	0.07112	1.800E-03
25	1	+	+	-	-	-	0.01717	8.081E-04
26	1	+	+	-	-	+	0.03434	8.332E-04
27	1	+	+	-	+	-	0.01734	8.107E-04
28	1	+	+	-	+	+	0.03468	8.107E-04

Run No.	Replicate	A	B	C	D	E	Intima Average LDL Concentration (mg/ml)	LDL Coverage Area (m²)
29	1	+	+	+	-	-	0.01717	8.332E-04
30	1	+	+	+	-	+	0.03434	8.081E-04
31	1	+	+	+	+	-	0.01736	7.705E-04
32	1	+	+	+	+	+	0.03472	8.081E-04
33	2	-	-	-	-	-	0.03731	1.872E-03
34	2	-	-	-	-	+	0.07461	1.794E-03
35	2	-	-	-	+	-	0.03743	1.805E-03
36	2	-	-	-	+	+	0.07487	1.805E-03
37	2	-	-	+	-	-	0.03729	1.794E-03
38	2	-	-	+	-	+	0.07459	1.872E-03
39	2	-	-	+	+	-	0.03748	1.805E-03
40	2	-	-	+	+	+	0.07496	1.872E-03
41	2	-	+	-	-	-	0.01709	8.107E-04
42	2	-	+	-	-	+	0.03417	8.107E-04
43	2	-	+	-	+	-	0.01727	7.780E-04
44	2	-	+	-	+	+	0.03453	7.780E-04
45	2	-	+	+	-	-	0.01711	8.107E-04
46	2	-	+	+	-	+	0.03421	8.107E-04
47	2	-	+	+	+	-	0.01726	7.780E-04
48	2	-	+	+	+	+	0.03452	7.780E-04
49	2	+	-	-	-	-	0.03741	1.709E-03
50	2	+	-	-	-	+	0.07481	1.709E-03
51	2	+	-	-	+	-	0.03740	1.709E-03
52	2	+	-	-	+	+	0.07480	1.709E-03
53	2	+	-	+	-	-	0.03738	1.709E-03
54	2	+	-	+	-	+	0.07476	1.709E-03
55	2	+	-	+	+	-	0.03738	1.664E-03
56	2	+	-	+	+	+	0.07476	1.709E-03
57	2	+	+	-	-	-	0.01721	7.705E-04

Run No.	Replicate	A	B	C	D	E	Intima Average LDL Concentration (mg/ml)	LDL Coverage Area (m^2)
58	2	+	+	-	-	+	0.03442	7.705E-04
59	2	+	+	-	+	-	0.01739	7.881E-04
60	2	+	+	-	+	+	0.03477	7.881E-04
61	2	+	+	+	-	-	0.01720	7.705E-04
62	2	+	+	+	-	+	0.03440	7.705E-04
63	2	+	+	+	+	-	0.01737	8.207E-04
64	2	+	+	+	+	+	0.03473	8.207E-04

Results and Discussions

Model validation

The models were implemented and solved in the axisymmetric multi-zone artery model (Figure 5.1 and 5.2). The simulation result was validated against the result from Olgac et al. [20]

The velocity vector plot in the vicinity of the lesion is shown in Figure 5.4. The observed results from the simulation revealed the path line magnitude and direction of the blood flow. It is clearly seen that the maximum velocity was found at the tip of the lesion where the diameter of the artery was reduced sharply. The recirculation zone region was also found right behind the stenosis. Four key variables including WSS, filtration velocity, LDL concentration profile, and LDL solute flux from the simulation model agreed well with that of the Olgac *et al.* work as presented in Figure 5.5, 5.6, 5.7, and 5.8, respectively.

The wall shear stress plot in the vicinity of the lesion is shown in Figure 5.5. The result showed the highest wall shear stress value at the point of stenosis ($Z^*_{sep} = 4.5$). The peak indicated the highest velocity gradient which was presented at the location of the maximum reduction in artery diameter. The circulation zone region presented behind the stenosis. In fact, the separation point and reattachment point were able to reveal from the WSS plot. The peak location of

WSS was found to be in agreement with other studies [20,72,88,89]. The filtration velocity (J_v) plot along the endothelium interface is shown in Figure 5.6. The plot referred as the volume flux of the blood flow passing through the endothelium layer.
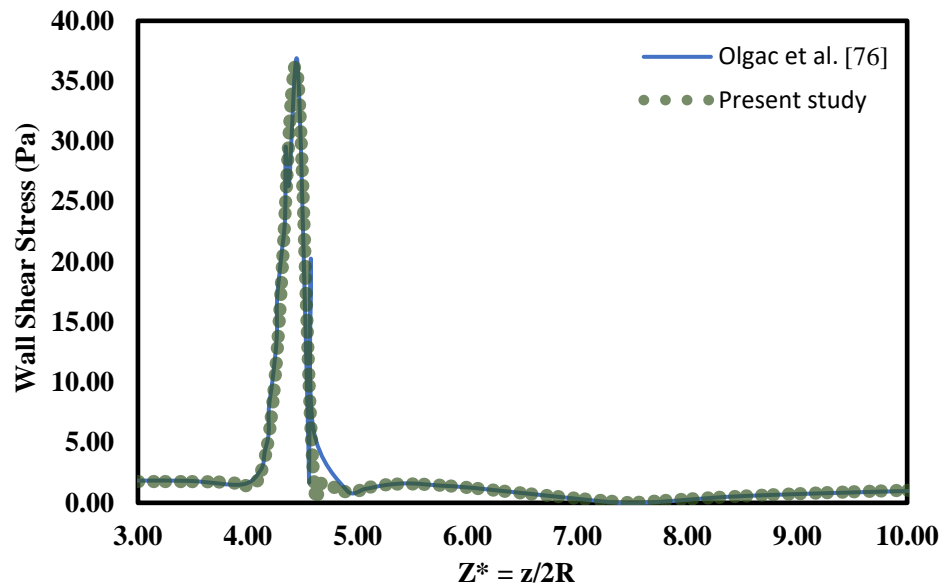
Figure 5.5 *Wall shear stress variation in the vicinity of the lesion along the normalized endothelial and location Z* = z/2R where z is the artery axial location from the model domain inlet and R is the inner radius of the lumen*
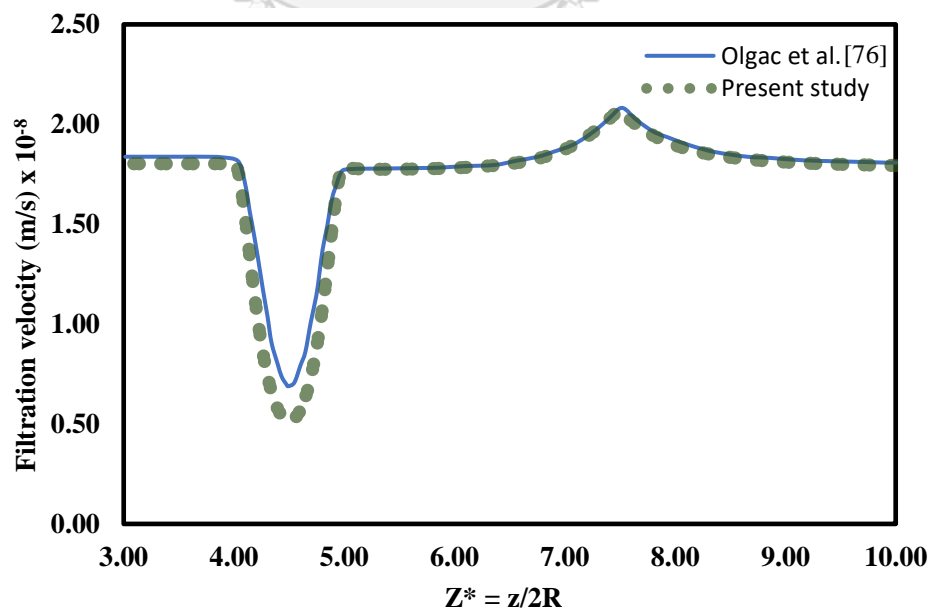
Figure 5.6 *Filtration velocity through the endothelial layer versus the normalized endothelial axial location Z**
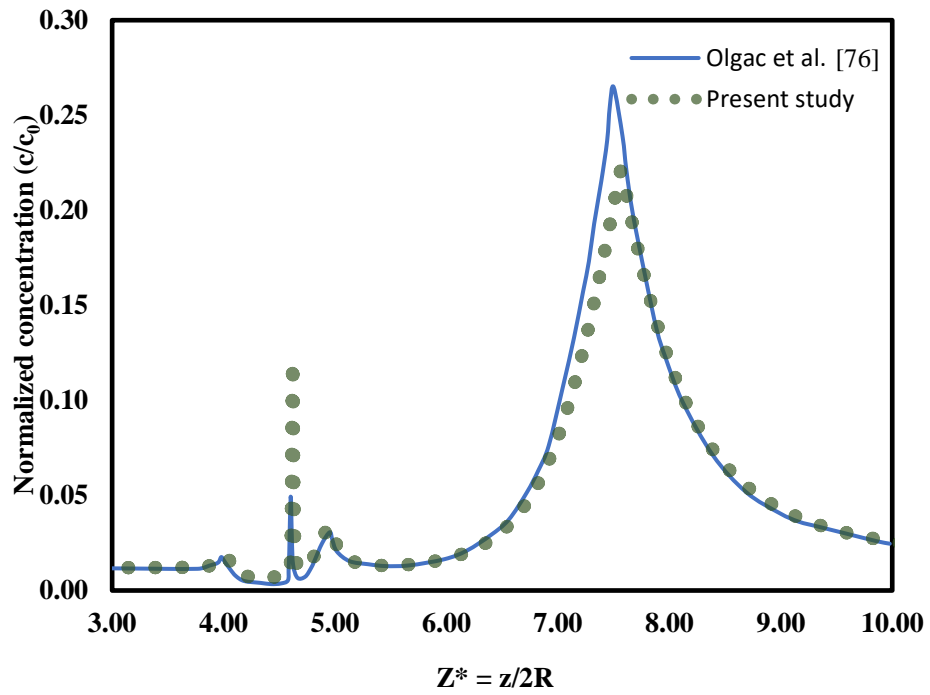
Figure 5.7 *Normalized LDL concentration profile along the normalized endothelial axial location*
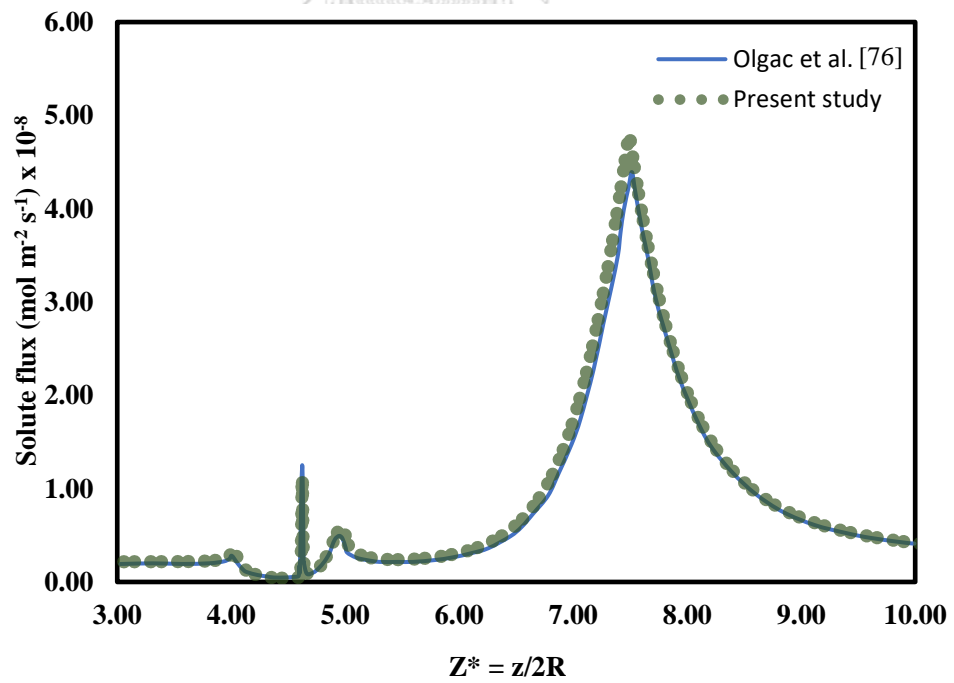
Figure 5.8 *Solute flux through the endothelial layer*
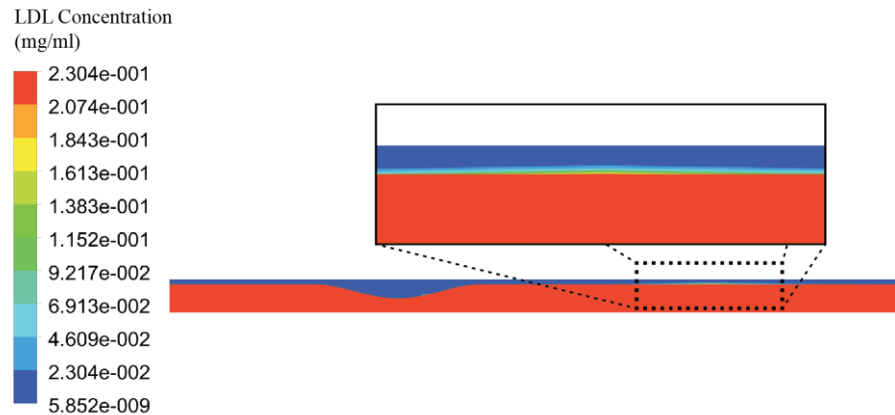
Figure 5.9 LDL concentration contour in intima zone

The plot showed the filtration velocity decreased acutely at the location of the stenosis. The increasing of intima layer (wall layer) thickness made the flow resistance of the wall to be higher which reflected in term of R_{wall} and R_{Total}. The maximum filtration velocity was increased and reached its maximum at the reattachment point. ($Z^*_{reattach} = 7.5$)

The LDL concentration profile is shown in Figure 5.7. The LDL concentration reached to a local peak at the separation point and the maximum peak at the reattachment point. The maximum peak value was approximately two times higher than that of the local peak. The LDL concentration profile was corresponding with the solute flux profile as shown in Figure 5.8. The profile showed that maximum solute flux was found at the re-attachment point next to the stenosis site [90]. The contour plot of LDL concentration in Figure 5.9 confirmed the location where solute flux was high. At the reattachment point, the LDL concentration was highest with the value about 0.23 times of the inlet concentration, while the average concentration elsewhere was about 0.05 times.

**Statistical analysis of intima average LDL concentration**

LDL build-up in the artery wall leads to its oxidative modification into highly atherogenic particle inducing the development of atherosclerotic lesions, namely, oxidized LDL (oxLDL) [91]. The average LDL concentrations in intima layer of each individual cases were measured from the results by the well-validated model as expressed earlier. The results are shown in Table 5.2. The maximum intima

average LDL concentration was found from Run 40 with the value of 0.074936 mg/ml. which was the case when the blood density and blood viscosity were set as low and plasma density, plasma viscosity, and LDL concentration level were set as high. The minimum intima average LDL concentration was found from Run 9 and Run 13 with the value of 0.01706 mg/ml. These two runs were shared the same properties except the different in level of plasma density, in which Run 9 was set as low and Run 13 was set as high. The 2^5 factorial design was used to analyze the simulation outcomes. Figure 5.10 shows the half-normal plot which helps to distinguish the dominant factors that affect the intima average LDL concentration. The deviation of the factor in the plot from the normal line implies that the factors have statistical significance on the average LDL concentration. The plot clearly showed that blood viscosity (B) and inlet LDL concentration level (E) were deviated away. Other blood factors including blood density (A), plasma density (C), and plasma viscosity (D) were screened out by the plot. The interaction between blood viscosity and inlet LDL concentration (BE) was also marked as significant effect on intima average LDL concentration.
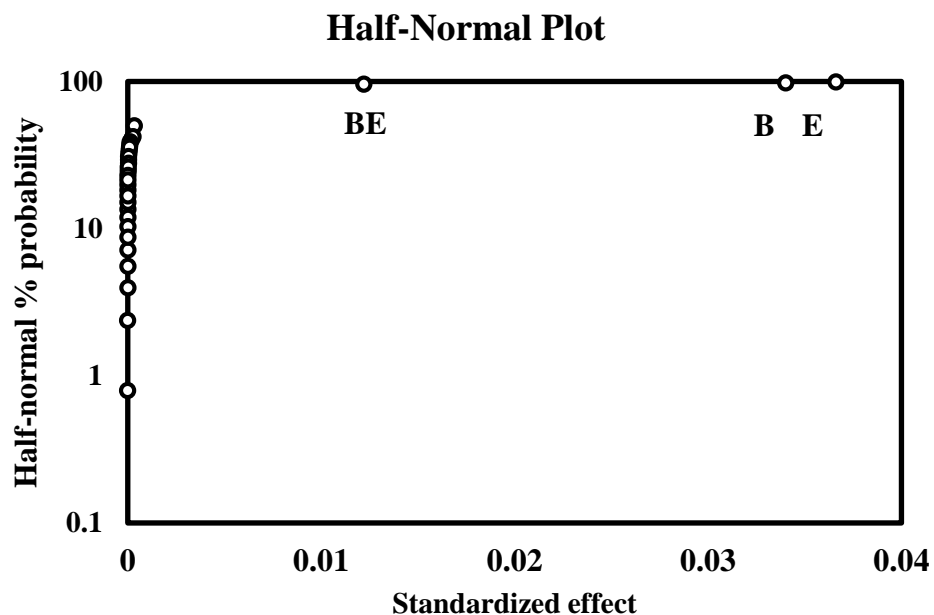
Half-Normal Plot

Figure 5.10 The half-normal probability plot of blood factors on the intima average LDL concentration

Table 5.3 *Analysis of variance for response 1: Intima average LDL concentration level*

Source	Sum of Squares	df	Mean Square	F Value	p-value
Model	6.33E-03	3	2.11E-03	6182.17	< 0.0001
B - Blood Viscosity	3.21E-03	1	3.21E-03	9397.04	< 0.0001
E - LDL Concentration Level	2.77E-03	1	2.77E-03	8105.36	< 0.0001
BE	3.57E-04	1	3.57E-04	1044.11	< 0.0001
Residual	2.05E-05	60	3.41E-07		
Lack of Fit	7.00E-07	28	2.50E-08	0.04	1.00E+00
Pure Error	1.98E-05	32	6.18E-07		
Cor Total	6.35E-03	63			

The study utilized the analysis of variance (ANOVA) to determine the significant levels of those preliminary-screen factors in Figure 5.10. Table 5.3 provides the result of the analysis. At given confidence interval of 99.99%, the p-value of the significant parameters was lower than 0.0001, thus, the ANOVA table given the additional confirmation that the blood viscosity (B), inlet LDL concentration level (E), and their interaction (BE) had the significant effects on the intima average LDL concentration. Figure 5.11, 5.12, and 5.13 are plotted for further analysis on how these significant parameters impact the intima average LDL concentration. Figure 5.11 shows the main effect plot of the blood viscosity. The intima average LDL concentration decreased when blood viscosity increasing. Physically, the phenomena can be explained as that high blood viscosity makes it more difficult for the LDL particles to penetrate into the intima wall which happened to make the average LDL concentration in the intima zone to be low. Mathematically, the Eq. 5.16 explains this certain behavior. The term of wall shear stress: $WSS = \left| \mu \frac{dv}{d\bar{n}} \right|$ is linearly proportional to the fluid viscosity level. The higher the viscosity resulting in high wall shear stress. This also yielded the lower value of endothelial shape index (SI) as shown in Eq. 5.15. Therefore, through Eqs. 5.12-5.14, the hydraulic conductivity of the leaky junction pathway, $L_{p,lj}$ (see Eq. 5.9) become lower. In another word, the higher wall shear stress value

reduced the penetration ability of the LDL particles that going through the endothelium layer onto the intima zone. Therefore, less LDL particles were accumulated in the intima zone. The modelling of the phenomenon was in a good agreement with the finding reported by Sakamoto et al [92].

The main effect plot of inlet LDL concentration is shown in Figure 5.12. The intima average LDL concentation was high corresponded with the high inlet LDL concentration. The different of LDL concentration between the lumen-endothelium interface and the endothelium-intima interface was the driving force for local mass transfer which denoted in term C_i^{endo} of Eq. 5.17. This was well agreed with Wilson et al. [77], that the higher LDL concentration within the blood stream would give a higher risk of having coronary heart disease.

Figure 5.13 shows the interaction effect between blood viscosity (B) and inlet LDL concentration level (E). The interaction effect implied that the impact of one factor could depend on the level of the another. The plot shows that those two lines neither cross nor parallel to each other which stated as ordinal interaction between these two factors. Within the interested range of study, the plot showed only a small mutual effect of these factors so that the predicted intima average LDL concentration was high when both blood viscosity and inlet LDL concentration level were high. Vice versa, the predicted intima average LDL concentration was low when the blood viscosity and inlet LDL concentration level were high.
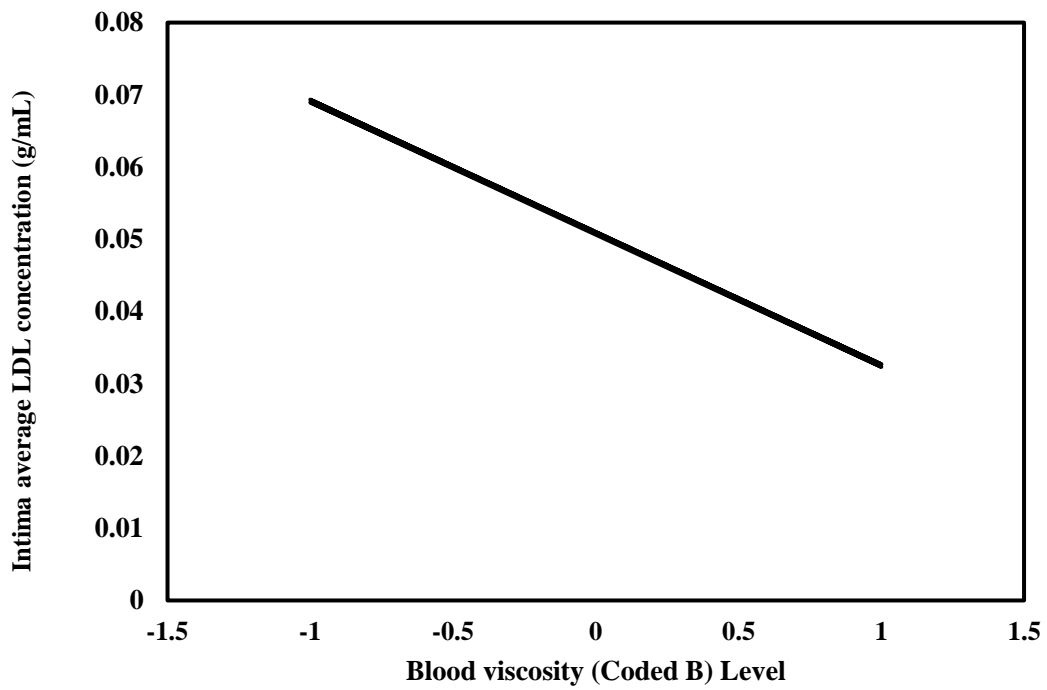
Figure 5.11 *The main effect plot of blood viscosity on average LDL concentration*
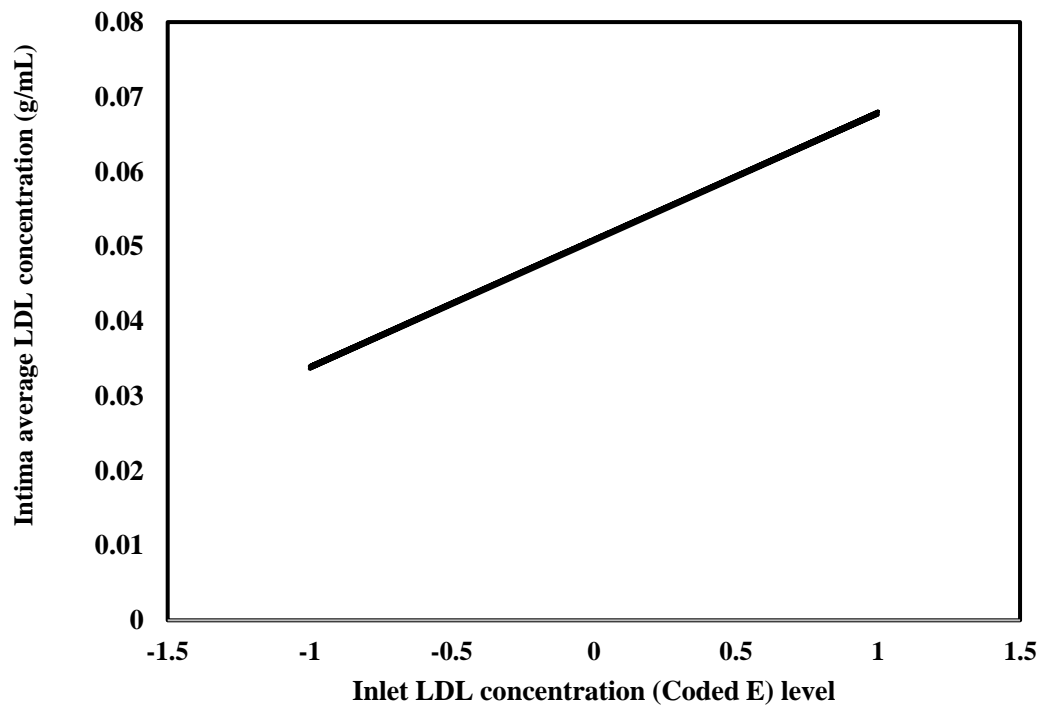
Figure 5.12 *The main effect plot of inlet LDL concentration level on the intima*

average LDL concentration
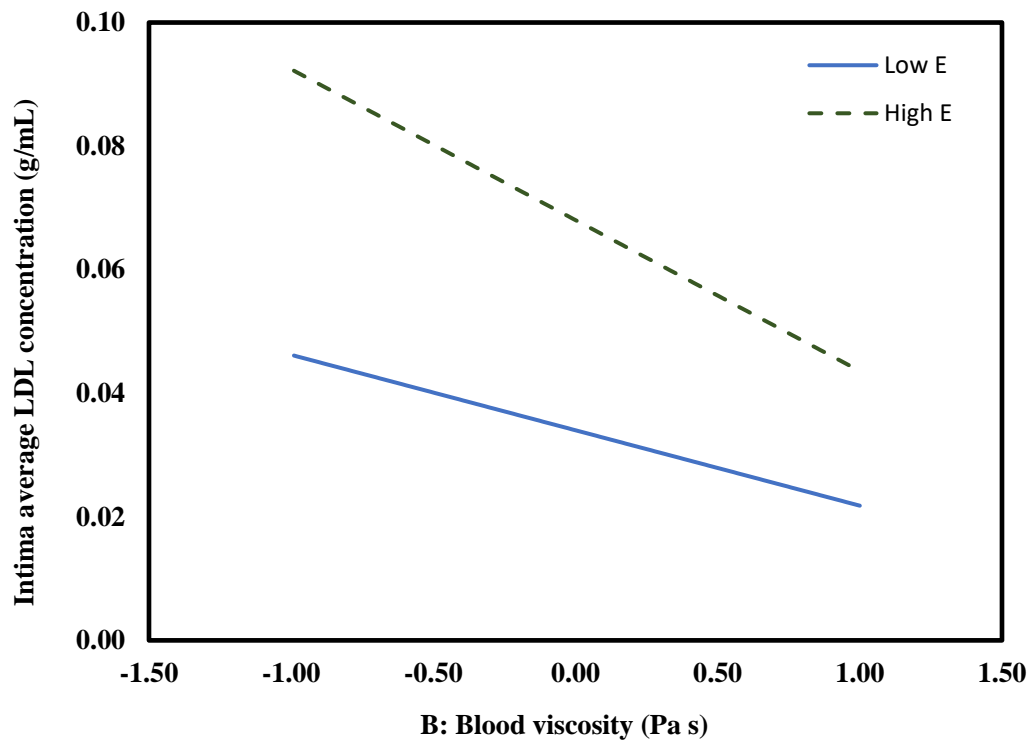
Figure 5.13 *The interaction plot between initial LDL concentration and blood viscosity*
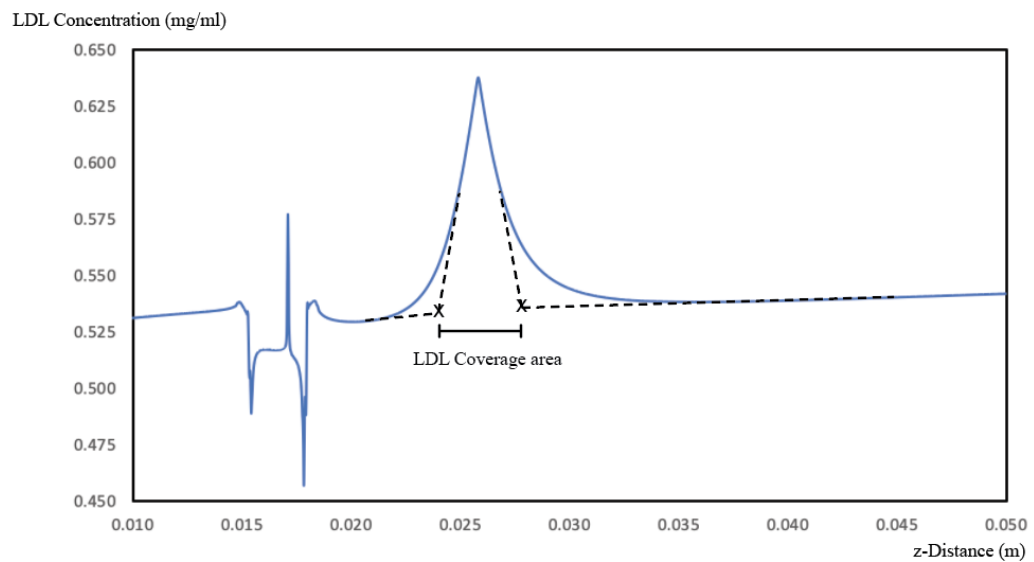
Figure 5.14 *Deposited LDL concentration in the intima region versus endothelial*

axial location

Statistical analysis of LDL coverage area

The LDL coverage area is measure by the ratio of surface area where LDL particles were deposited into the intima zone to the total surface area of the endothelium-intima interface which is determined from the plot of the LDL concentration along the endothelium-intima interface. The inflection point of the slope was used to define the cut-off point for the selected area. The results in Table 5.2 showed that Run 4, 33, 38, and 40 had the highest LDL coverage area $(1.872 \times 10^{-2}$ m$^2)$. These four runs shared the same value of blood density and blood viscosity. The lowest LDL coverage area was found in Run 9 with the value of 7.604×10^{-3} m^2, in which all blood factors were set as low except for the blood viscosity. Figure 5.15 shows the half-normal plot which clearly indicated that all of the effects were lied closely along the vertical axis. This simply screened out all of the non-significant factors except the blood viscosity (B). The blood viscosity was the only significant factor that affect the LDL coverage area on the endothelium-intima interface.
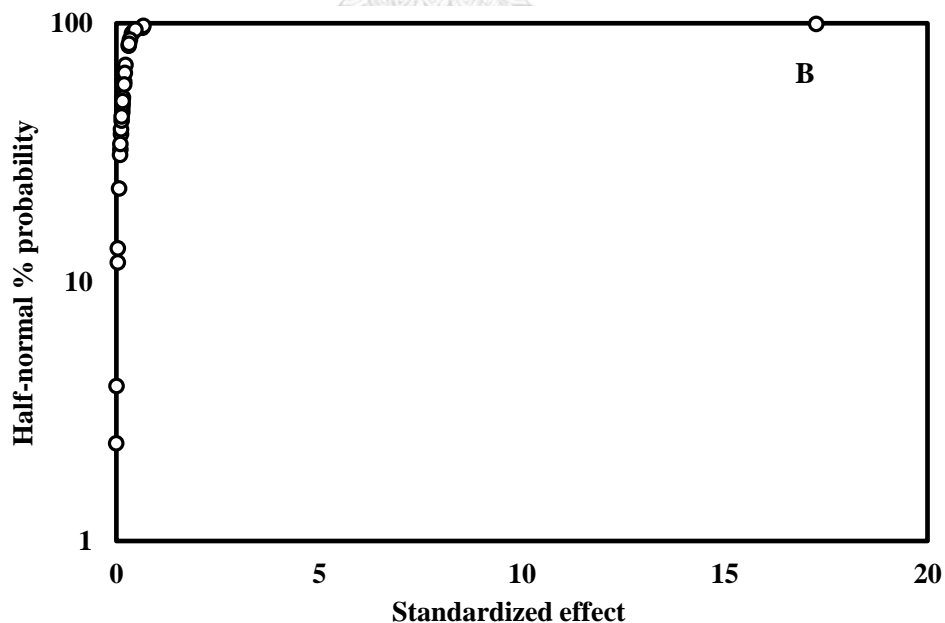
Figure 5.15 *The half-normal probability plot of flow parameters*

Table 5.4 *Analysis of variance for response 2: LDL coverage percentage*

Source	Sum of Squares	df	Mean Square	F Value	p-value
Model	4764.03	1	4764.03	4957.28	< 0.0001
B - Blood Viscosity	4764.03	1	4764.03	4957.28	< 0.0001
Residual	59.58	62	0.9610		
Lack of Fit	33.81	30	1.13	1.40	0.1760
Pure Error	25.77	32	0.8054		
Cor Total	4823.62	63			
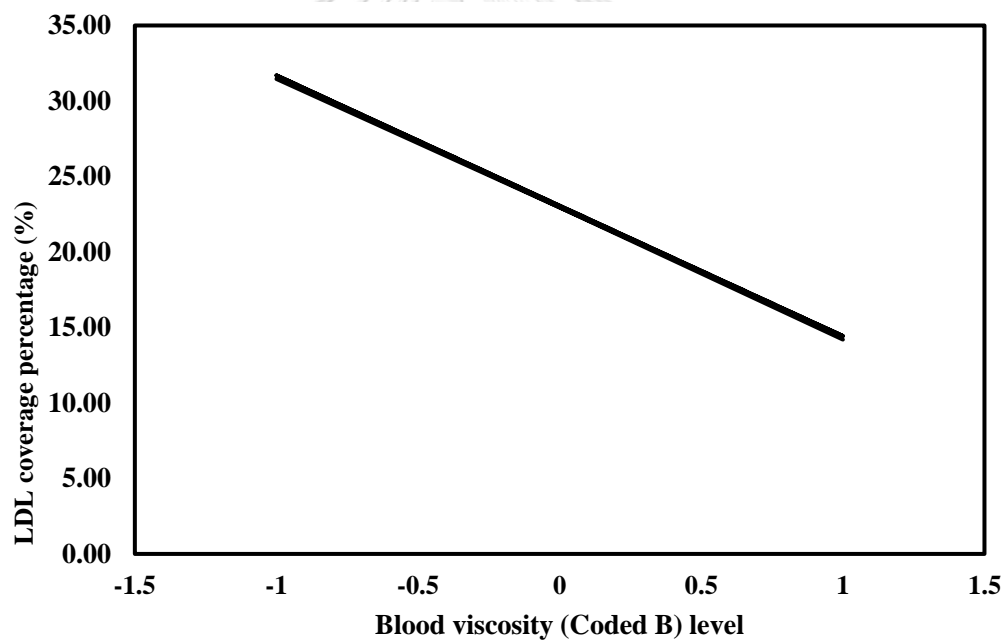
Figure 5.16 *The effect plot of blood viscosity on the LDL coverage percentage.*

Table 5.4 shows the analysis of variance (ANOVA). It further confirmed that the factor B (blood viscosity) had significant effect on the LDL coverage area with the p-value less than 0.0001. The main effect plot of blood viscosity on the LDL coverage area is shown in Figure 5.16. The blood viscosity was inverse proportions to the LDL coverage area. In short, the higher of the blood viscosity gave the lower of the LDL covering the intima surface. The low level of viscosity, 2.5×10^{-3} Pa-s, resulted in the LDL coverage area of 1.751×10^{-2} m^2. In comparison, the high level of viscosity, 4.5×10^{-3} Pa-s, resulted in the LDL coverage area of 7.914×10^{-3} m^2. Physically, the increase of blood viscosity caused the higher flow resistance through the endothelium layer (R_{end}). This will lower the filtration velocity comparing with the other cases with lower blood viscosity. From the statistical analysis, the results suggested that the high blood viscosity level could reduce the LDL coverage area on the endothelium-lumen interface. Run 9 and Run 13 gave the lowest average LDL concentration in the intima zone. Both cases had high level of blood viscosity and low blood LDL concentration. Run 9 also had the lowest LDL coverage area. Low intima average LDL concentration and low LDL coverage area are preferable conditions for this study. The interpretation of this statistical data serves as a guideline for additional analysis in this study field. According to the model, it also suggests that decreasing the LDL concentration and increasing the blood viscosity can potentially reduce the risk of having atherosclerotic plaque. These blood parameters are thus likely to be controlled by medical treatment or changing living pattern.

Conclusion

Three-zone artery model was proposed to investigate blood flow and LDL transportation in a coronary artery using computational fluid dynamics technique. The three-zone artery model which split the domain into lumen zone, endothelium zone, and intima zone was implemented and simulated in ANSYS Fluent. Based on Olgac et al's axisymmetric artery geometry [20], the model results was validated and compared to ensure the model validity. The model was further extended to statistically study the effect of blood flow factors on the intima average LDL concentration and

LDL coverage area. Five typical blood factors included in this study were blood density, blood viscosity, plasma density, plasma viscosity, and LDL concentration level. To identify the significant of the parameters that led to the atherosclerotic lesion growth, 2^k factorial experimental design method was appointed and the outcomes of the study could be concluded as:

- Blood viscosity and LDL concentration level were identified as influential blood factors affecting the atherosclerotic lesion growth.
- Blood viscosity had negative effect on the intima average LDL concentration as it was decreased the flow to penetrate into arterial wall.
- In opposite, the luminal LDL concentration level had a positive effect on the intima average LDL concentration. With the higher of the luminal LDL concentration, the higher LDL concentration within the intima was observed.
- The interaction effect between these two blood factors showed a small mutual effect within the study range.
- The LDL coverage area on the endothelium interface was strongly depended on blood viscosity. The LDL coverage area were decreased with the increasing of blood viscosity. The viscosity then played an important role in the flow resistance due to the shear force.

In summary, the statistical study based on numerical simulation of the three-zone artery computational fluid dynamics model was developed to serve as a guideline for the investigation of atherosclerotic lesion growth. The two identified influential factors could provide beneficial advices for medical treatment to lower the risk of having atherosclerotic lesion. Nonetheless, the simulation was done based on a simplified artery geometry with might be the limitation of the study. A further improvement of the future study is to implement the model into the real patient-specific artery geometry. In addition, more detail on the species transport must be included for quantitively prediction.

CHAPTER VI

CFD APPLICATION IN CIRCULATORY SYSTEM:

Biochemical interaction in the early stage formation of
atherosclerotic lesion in arterial wall

Blood flow within the cardiovascular system is driven by regular contractions and relaxations of the heart which generate periodic blood flow manner. The modeling of cardiovascular system is denoted as long-term processes which the time-scale of the processes is significantly longer than those of the normal flow in other systems [93]. To process the result with different size of respective time-scales, the explicit resolution of all parameters may become computational expensive [94,95]. Thus, to remove the time-scale associated with the periodic blood flow, the computational results are instead represented with their period-average equivalent.

For the modeling of atherosclerotic lesion formation, the transient flow structure further away from the boundaries may cause the period-average results to deviate from their steady-equivalent [96,97]. These flow structures are mainly identified to be influenced by the flow oscillation and geometric irregularities such as curves and bifurcation of the blood vessel [98,99]. The change in flow structure will also recognize as physiologic influence on the endothelial cells which is referred as flow disturbances [100].

The morphologic changes in endothelial cells are associated with the local flow disturbances such as near-wall flow field. It is reported that the endothelial cells are elongated primarily unidirectional to the flow direction. The endothelial cell forms a tight barrier to the particulate species such as lipoprotein (LDL). However, the shape of the endothelial cells becomes polygonal and their arrangements are less organized when the flow is under disturbances. This leads to the behavioral changes in the permeability of the local endothelial layer [101,102].

In this chapter, the improvement of the three-zone model from previous chapter has been studied. The three-dimensional patient-specific artery geometry is used instead of idealized axisymmetric geometry. In addition, species transport equations and biochemical interaction are also included in the model for better understanding of the

flow phenomena. The shear-rate depended viscosity model, Carreau's model, is utilized to represent the viscosity of blood. The species concentration of foam cell inside the intima layer is examined and proposed as a sign of the early stage development of the plaque. The objective of this study is to develop the mathematical model of atherosclerotic lesion growth with biochemical interaction and to study the compromise locations where the accumulation of the plaque occurs which makes significant buildup of the excessive cholesterol.

The mathematical model
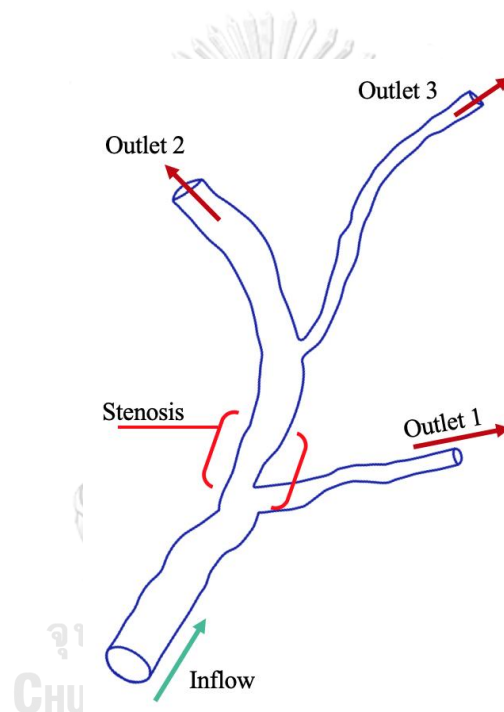
Figure 6.1 The 3-D illustration of the computation domain
representing flow boundary

The simulation was carried out using 3D computational fluid dynamics model. The coronary artery geometry was derived from the computed tomography of stenosed patient as shown on Figure 6.1. The bifurcations were renowned for the inducing of the localized flow structures that generated flow disturbances [98]. The model physically had one velocity inlet and three pressure outlets with mild stenosis right after the bifurcation. The flow region, lumen zone, was bounded by the wall layer. The three-zone artery model was included, to extend the wall layer into three considered zones: lumen zone, endothelium zone, and intima zone. First, blood which was the primary

fluid flowing inside the lumen zone was consisted of two species: low-density lipoproteins (LDL) and monocytes. The blood was assumed to be incompressible fluid, which the density was defined as a constant value. The second zone, the endothelium zone, was a thin layer acts as a membrane controlling the blood volume flux and biochemical species from entering the intima layer. As the endothelial cell thickness was thin compared with other layers, the variations of the flow and species within endothelium zone were neglected. The endothelium zone was given a thickness of 1 micron which then split into 2 psedo-interfaces, the lumen-endothelium interface and the endothelium-intima interface. These interfaces controlled the specie fluxes using custom user-defined functions. Once these species permeated themselves through this layer, they degraded and formed other species: oxidized low-density lipoproteins (oxLDL) and macrophages, respectively, in the intima zone as shown in the diagram of Figure 6.2.
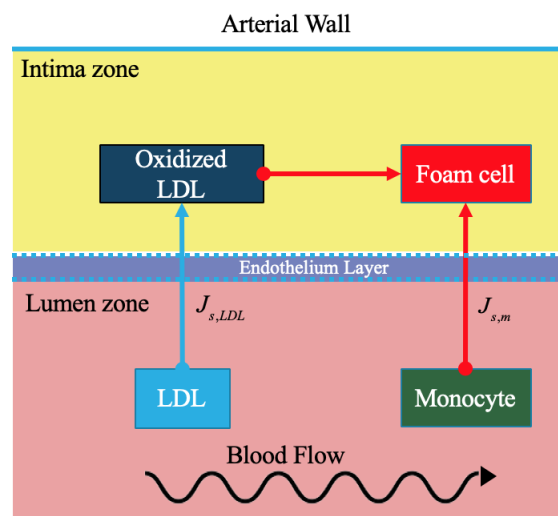
Figure 6.2 *The flow diagram representing the luminal wall layers and its transportation of the species*

The hemodynamics within lumen zone was governed by continuity and unsteady state Navier-Stroke equations (Eq. 6.1-6.2). Blood was assumed to have constant density of $\rho = 1,050$ kg/m^3 and a strain-rate dependent viscosity (μ) was expressed by Carreau's model (Eq. 6.3).

$$\frac{\partial \rho}{\partial t} + \nabla \cdot (\rho \vec{u}) = 0 \qquad (6.1)$$

$$\rho\left(\frac{\partial u_l}{\partial t} + (u_l \cdot \nabla)u_l\right) - \mu\Delta^2 u_l + \nabla p_l = 0 \tag{6.2}$$

$$\mu(\dot{\gamma}) = \mu_\infty + (\mu_o - \mu_\infty)[1 + (\lambda\dot{\gamma})^2]^{(n-1)/2} \tag{6.3}$$

where u_l is blood velocity in the lumen zone, and p_l is luminal pressure. $\dot{\gamma}$ is the strain rate obtained locally from the local flow domain. The parameters in Carreau's model were defined as λ = 3.313 s, and n = 0.3568. The zero and infinite strain-rate limit viscosities were defined μ_0 = 0.056 kg/m-s and μ_∞ = 0.00345 kg/m-s, respectively.

The coupling of the flow dynamics between lumen and intima zone were regulated by Three-pore model which was originated from Olgac et al [20]. Three-pore model expressed the total volume flux (J_v) as a combination of its three pathways including vesicular pathway ($J_{v,v}$), normal endothelial junction pathway ($J_{v,nj}$), and leaky junction pathway ($J_{v,lj}$).

$$J_v = J_{v,v} + J_{v,nj} + J_{v,lj} \tag{6.4}$$

The volume flux primarily flew through normal junction pathway and leaky junction pathway. Therefore, $J_{v,v}$= 0. Others are expressed as:

$$J_{v,nj} = L_{p,nj}\Delta p \tag{6.5}$$

$$J_{v,lj} = L_{p,lj}\Delta p \tag{6.6}$$

where, Δp is endothelial pressure drop. The hydraulic conductivity for the normal junction, $L_{p,nj}$ was reported as 1.16 ×10^{-9} m/(s·mmHg) [84]. The hydraulic conductivity for the leaky junction ($L_{p,lj}$) is defined as:

$$L_{p,lj} = \frac{A_p}{S} L_{p,slj} \tag{6.7}$$

where $\frac{A_p}{S} = 4w_l/R_{cell}\phi_{lj}$. R_{cell} is the endothelial cell radius, w_l is the half-width of a leaky junction which was 20 nm as reported by Weinbaum et al. [103]. ϕ_{lj} is ratio of the leaky cell to the area of all the cells. It is defined as:

$$\phi = \frac{LC \times \pi R_{cell}^2}{\text{unit area}} \tag{6.8}$$

where the unit area was considered to be 0.64 mm^2 [20]. The ratio is depended on shape of the cell which correlated to the shear stress acting on the cell. The shape index is defined as:

$$SI = 0.380e^{-0.790WSS} + 0.225e^{-0.043WSS} \tag{6.9}$$

The number of leaky cells (LC) is the correlation between number of mitotic cells (MC) and shape index are defined as:

$$LC = 0.307 + 0.805(MC) \tag{6.10}$$

$$MC = 0.003797e^{14.75 \cdot SI} \tag{6.11}$$

The hydraulic conductivity of a single leaky junction is given by:

$$L_{p,slj} = \frac{w^2}{3\mu_p l_{lj}} \tag{6.12}$$

where w is the half-width of the leaky junction, l_{lj} is the length of the leaky junction, and μ_p is plasma viscosity. The specie transport of LDL is modeled by convection-diffusion equation with additional reaction term:

$$\frac{dC_{LDL}}{dt} = D_{LDL}\Delta C_{LDL} - u_w \cdot \nabla C_{LDL} - k_{LDL}C_{LDL} \tag{6.13}$$

where C_{LDL} is the concentration of LDL (mol/m^3) and D_{LDL} is the diffusion coefficient of the LDL. k_{LDL} is the degradation rate of LDL. The flow velocity (u_w) in this region is governed by Darcy's law which is calculated from

$$u_w = \frac{\kappa_p}{\mu_p}\nabla p_w \tag{6.14}$$

where p_w and κ_p are pressure inside the intima layer and permeability of the intima layer, respectively. The viscosity (μ_p) and density (ρ_p) of the plasma medium in this layer were set as 0.0035 Pa.s and 1000 kg/m^3. The degradation of the LDL particles was represented with k_{LDL} as the reaction rate constant. The LDL penetration flux ($J_{s,LDL}$) was controlled by the equation given as:

$$J_{s,LDL} = P_{app}C_{LDL}^{endo} \tag{6.15}$$

where C_{LDL}^{endo} is the local concentration of the LDL in the endothelium layer and the total apparent permeability (P_{app}) is determined by the combination of permeability of endothelium according to its pathway: vesicular pathway (P_v), normal junction pathway ($P_{app,nj}$) and leaky junction pathway ($P_{app,lj}$).

$$P_{app} = P_v + P_{app,nj} + P_{app,lj} \qquad (6.16)$$

According to the size of the LDL particle, the normal junction permeability can be neglected due to its size comparing with the size of the physical passageway. The values of P_v and $P_{app,lj}$ were 1.9×10^{-10} m/s and 1.92×10^{-11} m/s, respectively, as reported by Olgac et al [88]. Later, the degraded LDL, or oxidized LDL, was formed inside the intima zone. It is an unpleasant specie which consequently causing the monocyte to migrate in. In this model, oxidized LDL acts as an intermediate species for controlling monocyte penetration flux and determining the growth of latter problematic species, foam cell. The specie transport equations for monocytes and macrophages are defined as:

$$\frac{dC_m}{dt} = D_m \Delta C_m \qquad (6.17)$$

$$\frac{dC_M}{dt} = D_m \Delta C_M - k_m L_{ox} C_M \qquad (6.18)$$

where C_m and C_M is the concentration of monocytes and macrophages, respectively. D_m is diffusive coefficients of monocytes/macrophages. k_m and L_{ox} are apoptosis rate constant from macrophages to foam cell and the quantity of LDL degrading inside the intima zone, respectively. Monocytes were continuously fed in at the inlet of the lumen zone which governed by diffusion equation in Eq. 6.16. The penetration flux of monocytes into intima zone was modeled as described by Bulelzai & Dubbeldam [104] in Eq 6.19. The monocyte flux ($J_{s,m}$) is depended on the shear rate of the flow along the endothelium.

$$J_{s,m} = \frac{m_r}{1+(WSS/WSS_0)} C_{oxLDL} C_{m,l} \qquad (6.19)$$

The monocyte was regulated by the concentration of the intermediate species, oxidized LDL (C_{oxLDL}). The flux was zero when the oxidized LDL was completely consumed

by the reaction. The concentration of monocyte in the lumen zone ($C_{m,l}$) was also the driving force of the flux. The constant m_r which controlled the rate of monocyte flux entering the intima zone was set to 5.5×10^{-4} m³ mol⁻¹ day⁻¹ as fitted according to the experiment which explained in Cilla et al [72]. Once the monocyte was inside the intima zone, it was assumed that all the monocytes would transform into macrophages.

The formation of foam cell (C_F) is governed by

$$\frac{dC_F}{dt} = k_m L_{ox} C_m \tag{6.20}$$

where, C_F is the concentration of foam cell and k_m is kinetic constant for foam cell formation. Foam cell was considered as initial indication of plaque formation. For this study, the location where foam cell forms, is the significant interest for further medical prognosis of the disease.

Computational implementation

The mathematical models were implemented into the finite-volume solver ANSYS Fluent v19.2 with various customization of in-house functions to evaluate the volumetric flow through the endothelium interface, and boundary conditions. Computations were made with double-precision solver. The three-dimensional patient-specific stenosed coronary artery geometry was discretized with a hybrid mesh. The inflated polyhedral computational grid was constructed in the lumen zone and the tetrahedral element for the endothelium zone and the intima zone. The mesh reconstruction was done using ANSYS Fluent Mesher v19.2. The mesh independence of the flow field was conducted, a converged mesh of 5.29×10^6 elements was employed for the further study.

The SIMPLE algorithm was used to solve the pressure-velocity coupling of the Navier-Stokes equations. Second-order scheme was used to discretized flow variables for spatial and time continuum.
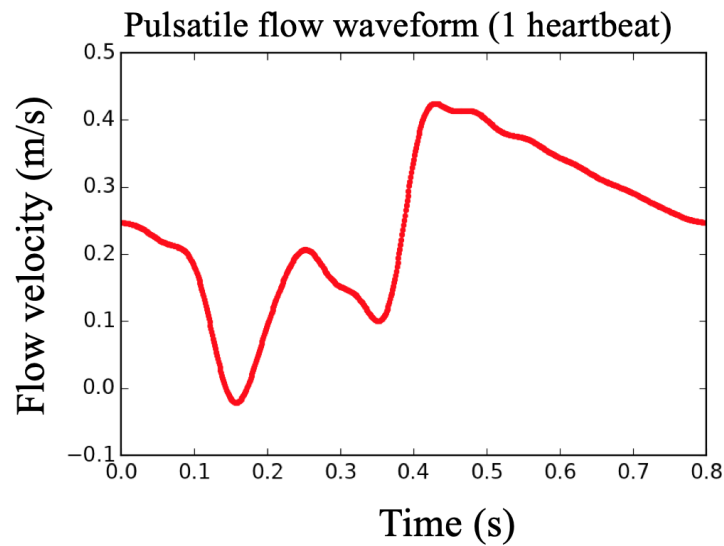
Figure 6.3 *The pulsatile flow waveform of the coronary artery*

The pulsatile waveform velocity profile was applied at the inlet as shown in Figure 6.3. A constant pressure boundary condition was set to each outlet with value matching with the period-averaged mass flow rate from experimental data. The media-adventitia layer (outer side of the wall) was assumed to have a constant pressure at 2,333 Pa.

The endothelium layer was handled with the special treatment using user-defined functions. The shear stress was prior determined at the wall of the luminal side.

$$\tau = -\mu \frac{\partial v}{\partial x} \tag{6.21}$$

The velocity gradient ($\frac{\partial v}{\partial x}$) was obtained from the data stored in the adjacent cell of the endothelium interface. The distance (∂x) was the first layer cell height which was tested to be independent from its size at 1 micrometer. The chosen cell height was also reported from previous studies that the appropriate size must be smaller than the size of endothelium cell in order to capture the intermediate behavior of the flow.

The filtration velocity (J_v) and the solute flux (J_s) were then calculated using the previously obtained wall shear stress (WSS). The values of calculated filtration velocity and solute flux were stored within the modified cell of endothelium layer as a user-defined memory (UDM). The values were set as Dirichlet boundary conditions using custom fixed-value cell zone condition in ANSYS Fluent solver.

The boundary condition at the pseudo-interface is defined as:

$$J_s = (1 - \sigma_f)J_v C - D_e \frac{\partial C}{\partial x} \tag{6.22}$$

Where J_s is an arbitrary flux value, σ_f is osmotic reflection coefficient which was set as $\sigma_f = 0.8514$. D_e is the diffusion coefficient of the arbitrary specie and C is local concentration of that specie. The inter-layer boundary condition was assumed to have constant solute flux from the lumen zone to the intima zone, therefore, the inter-layer boundary condition can be written as;

$$\left[(1 - \sigma_f)J_v C - D_e \frac{\partial C}{\partial x}\right]_- = \left[(1 - \sigma_f)J_v C - D_e \frac{\partial C}{\partial x}\right]_+ \tag{6.23}$$

The simulation was started from the steady-state of the constant inflow. The steady-state solution was used as the initial conditions for the pulsatile flow. The steady-state equivalent velocity was also investigated for contrastive study which caused by the variation of the flow pulsation.

The turbulent theory Reynolds decomposition technique was introduced to compare the calculation results with their steady-equivalent. The flow indices and specie indices were employed with period-averaging to extract meaningful data from their fluctuations.

$$\phi(x, y, z, t) = \overline{\phi(x, y, z, t)} + \phi'(x, y, z, t) \tag{6.24}$$

$$\overline{\phi(x, y, z, t)} = \frac{1}{T} \int_T \phi(x, y, z, t) \, dt \tag{6.25}$$

where ϕ denotes the flow and specie indices, $\bar{\phi}$ denotes the steady component of scalar ϕ, and ϕ' is the fluctuation of the scalar ϕ. T is the integration length of the time t.

By applying Eq. 6.23 and 6.24 to the specie concentration C_i, it can be decomposed into its period-average and transient components, for instance:

$$\overline{C_i(x, y, z, t)} = C_i(x, y, z, t) - C'_i(x, y, z, t) \tag{6.26}$$

Similarly, the technique was also applied to the solute flux and volume flux of the LDL and monocyte transport.

Results and discussion

The pulsatile flow within the coronary artery was computed up to 60th period of oscillation. The model was successfully implemented to the commercial CFD solver, Ansys Fluent. The three-pore model was previously validated against Olgac el al. which already reported in previous chapter. The model was further validated against the experimental results from the Biofluid Mechanics Lab, Charité University of Medicine, Berlin, Germany. The period-averaged mass flow ratio for all three outlets were compared. For the outlet 1, outlet 2, and outlet 3, the average mass flow ratios were 0.4595, 0.5019, and 0.0385, respectively, which the corresponded pressure value for each outlet were 6,985, 9,335, and 9,213 Pa.
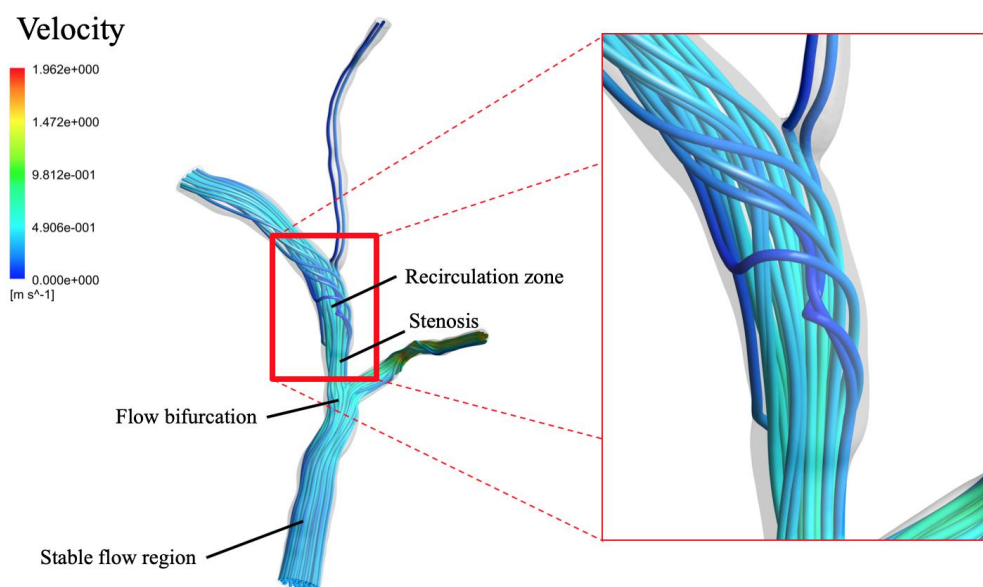
Figure 6.4 *The instantaneous flow velocity streamline at a certain time*

Figure 6.4 shows the instantaneous flow velocity streamline from the model. Refer to the streamlines, blood flow within the coronary artery was transported along the artery toward the bifurcation. The geometry wall was smooth which showed only minor changes of the vessel diameter. Before it reached the coronary bifurcation, the flow velocity increased as the diameter of the vessel decreased. Then, the flow encountered the topologic change in its transport spaces at the bifurcation. The flow adapted to the changes in direction and the variations of the cross-sectional area. Further, the sudden

expansion of the vessel right after the stenosis promoted the flow stream to separate from the main flow stream. The separated flow was moving at relatively lower velocity comparing to that of the main flow. Afterward, the flow then reattached to the main flow. The formation of the recirculation zone was found right after the flow was disturbed by the decreasing of the cross-sectional area similarly to the two-dimensional cases from previous chapter.

(a) (b)
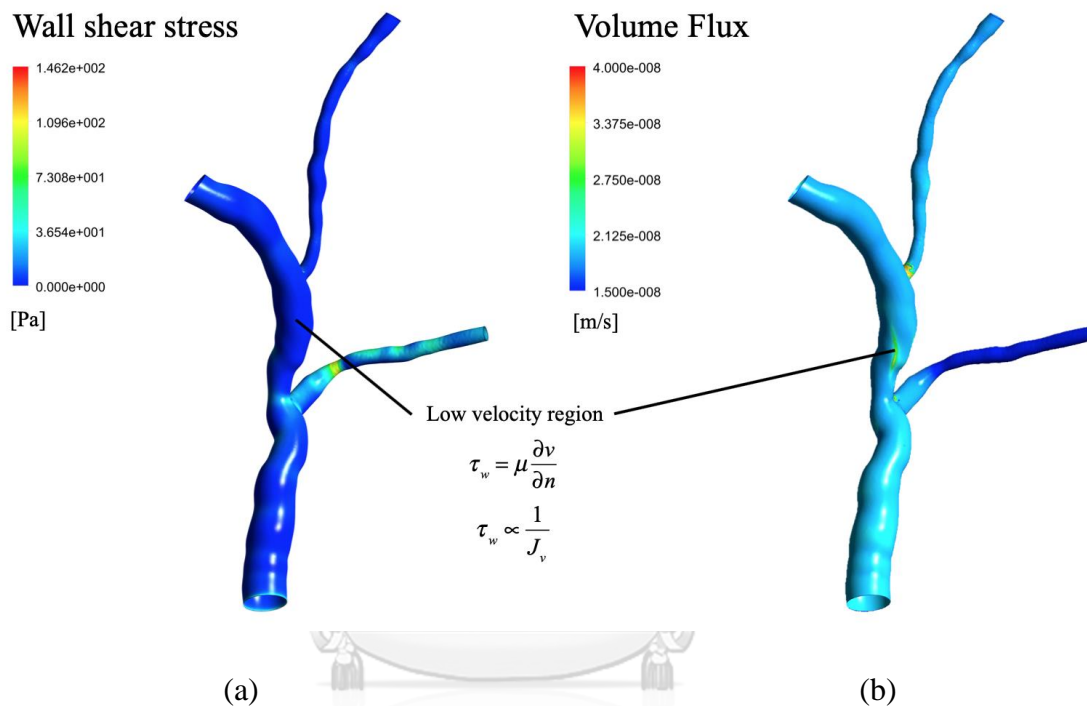
Figure 6.5 *(a) Wall shear stress and (b) volume flux (J_v) contours*

Figure 6.5 (a) shows the wall shear stress contour from the simulation result. At the recirculation region, the flow velocity was low resulting in low value of wall shear stress. From Eq. 6.9, the shape index of the endothelial cell is depended on the wall shear stress. The total volume flux (J_v) was determined which highly depended on the local wall shear stress value expressed in Eqs. 6.7-6.11. The volume flux of the blood which governed the flow through the endothelium interface is showed in contour in Figure 6.5 (b). It was clearly shown that the volume flux was in reverse relationship with the local wall shear stress. The volume flux was high where the recirculation region was formed. For further analysis of the study, data processing within the space

was made on the circumference of the circle in the area of interest (Figure 6.6) which was behind the stenosis where the volume flux showed the highest value.
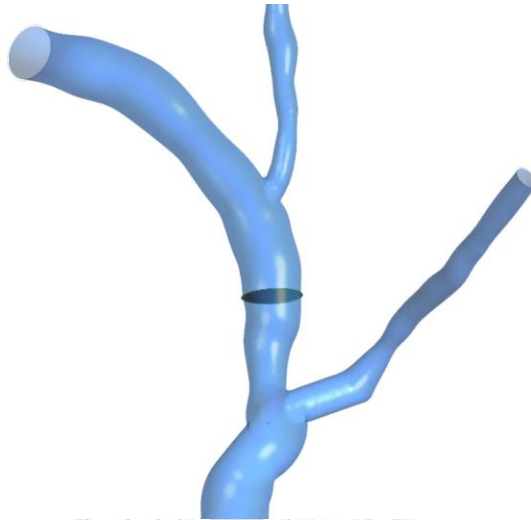
Figure 6.6 *Area of interest where LDL concentration and volume flux were significantly higher than that of the other regions.*
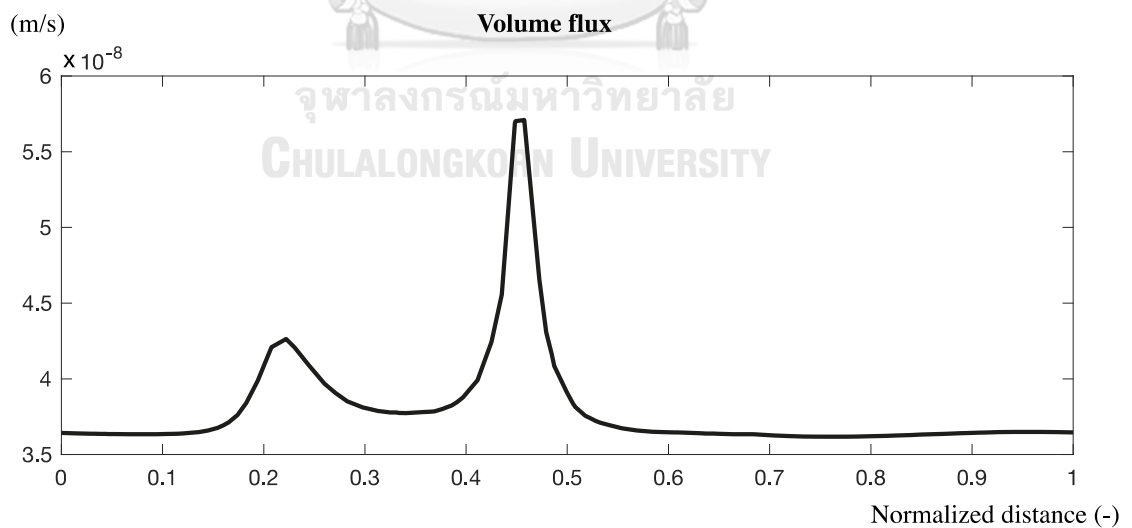
Figure 6.7 *Period-average volume flux along the length-normalized distance on the endothelium interface*
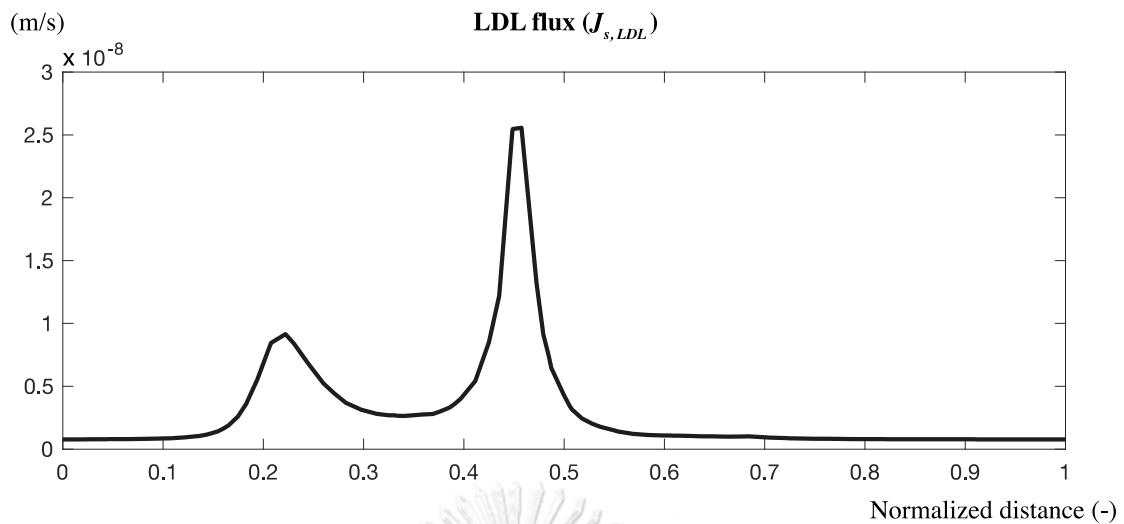
Figure 6.8 *Period-average LDL flux ($J_{s,LDL}$) along the length-normalized distance on the endothelium interface*
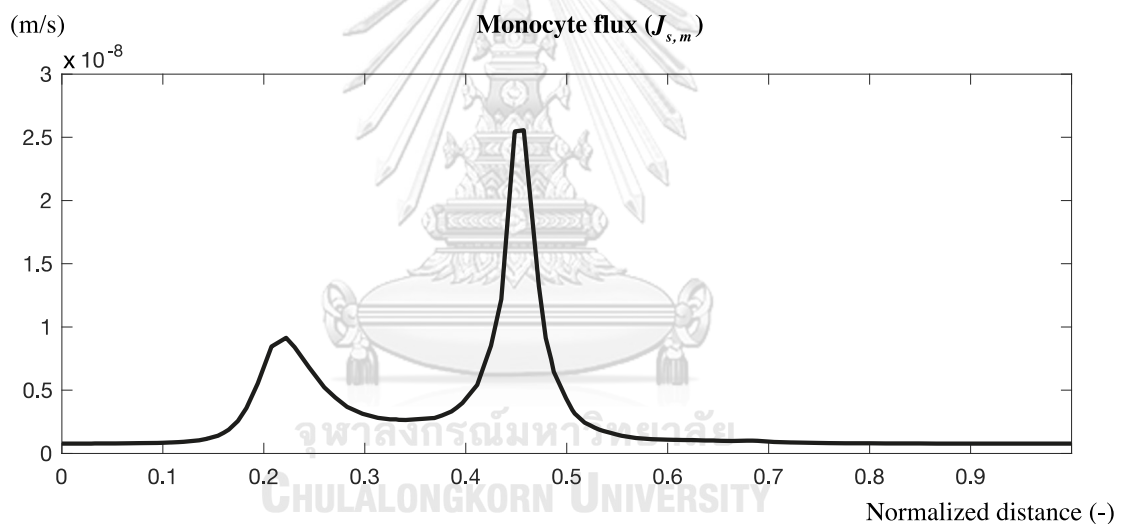
Figure 6.9 *Period-average monocyte flux ($J_{s,m}$) along the length-normalized distance on the endothelium interface*

The Reynolds decomposition technique was applied to the volume flux, LDL flux, and monocyte flux results using Eq 6.24 and 6.25 to represent their period-average solutions. Figure 6.7 shows the period-average volume flux of blood ($\bar{J}_v$) which permeated into the intima zone in the normal direction of the arterial wall. The peak of the plot revealed the location with the highest volume flux. It was corresponded with the high value of the contour plot in Figure 6.5 (b). For the blood-borne particulate, LDL and monocytes, the local flux profiles are shown in Figure 6.8 and Figure 6.9. The

plots showed similar profile for both species which was caused by the change of the total apparent permeability of the endothelial cell as shown in Eq 6.16. Both LDL flux and monocyte flux were expressed by the local shear stress. It was denoted from the plot that the peak location had a significant higher concentration value than that of the area around it.
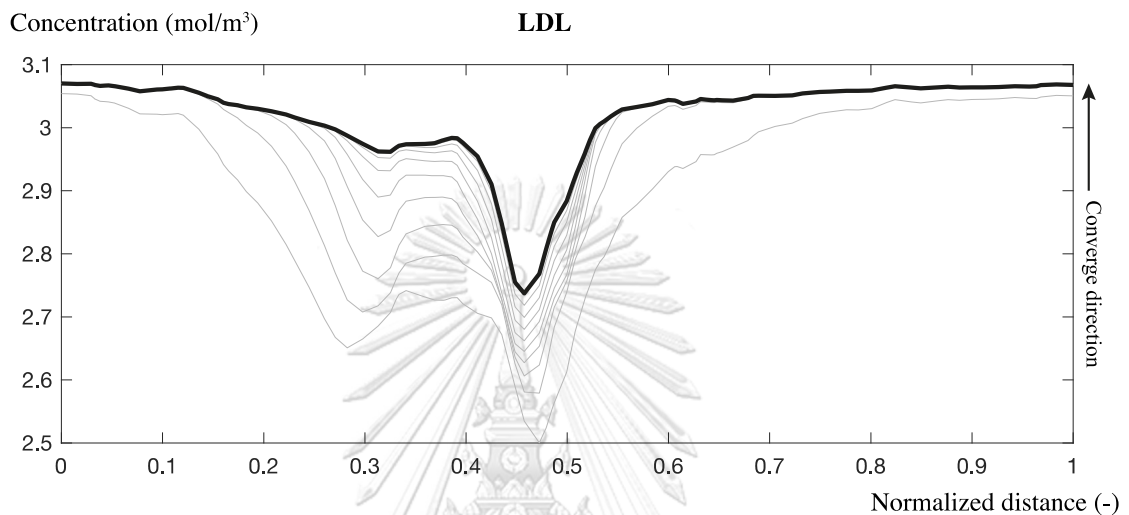
Figure 6.10 *Period-average LDL concentration along the length-normalized distance on the endothelium interface*

The flow pulsatility was investigated to compare the results with their steady-equivalent. The plot in Figure 6.10 depicts the LDL concentration for each flow period with each successive period. Each line represented the period-average LDL concentration of each period starting the first flow period at the bottom line. The concentration profiles for the LDL specie initially evolved in large changes, then gradually slowed down as they approached their respective steady-periodic states. Then, the result remains relatively unchanged with their successive period. It is also noted that by the end of the 60th flow period, the LDL concentration profiles were sufficiently converged to their quasi-steady state. This was corresponded with the results obtained from Gabriel et al [26]. Figure 6.11 shows the period-average LDL concentration and oxidized LDL concentration contour. The lowest concentration of LDL was found at the location where the LDL flux was the highest (see Figure 6.8 and Figure 6.10). However, the oxidized LDL concentration was high which expressed by the LDL specie conservation equation in Eq. 6.13. The LDL degrading term on the

right-hand side of the equation, $(-k_{LDL}C_{LDL})$, induced the reduction of LDL and promoted the formation of oxidized LDL. Mathematically, the LDL concentration (C_{LDL}) was a main driving force for the degradation of the specie. The location of these two incidents were correlated with each other as shown in the contours (Figure 6.11). The period-average concentration contours of macrophages and foam cell are shown in Figure 6.12. The assumption was made that all the monocytes that were permeated into the intima zone were fully differentiate themselves into macrophages. The contour represented the elevated macrophages concentration was occurred in the same way as other species. At the recirculation zone behind the stenosis showed the highest macrophages concentration. The unwanted specie, foam cell, was found where there were the present of both macrophages and oxidized LDL. The foam cell concentration contour is shown in Figure 6.12.
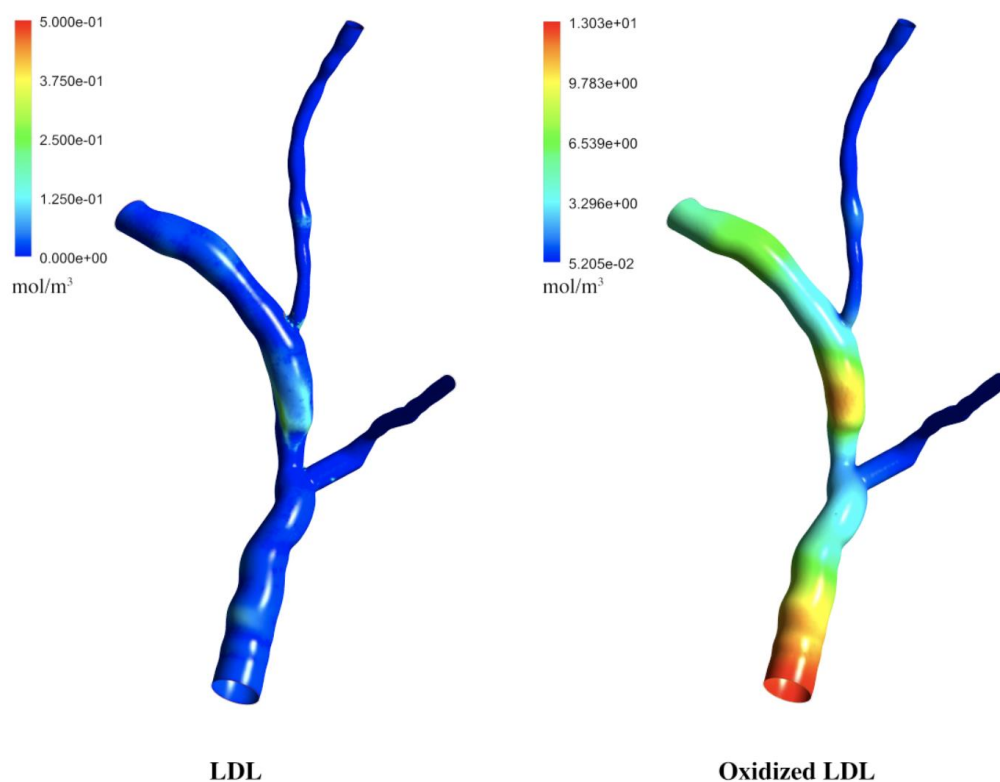
LDL　　　　　　　　**Oxidized LDL**

Figure 6.11 *Concentration contour of LDL on the lumen-endothelium interface and Oxidized LDL on the endothelium-intima interface after 60th flow period*

Macrophages **Foam cell**

Figure 6.12 *Concentration contour of macrophages and foam cell on the endothelium-intima interface after 60th flow period*
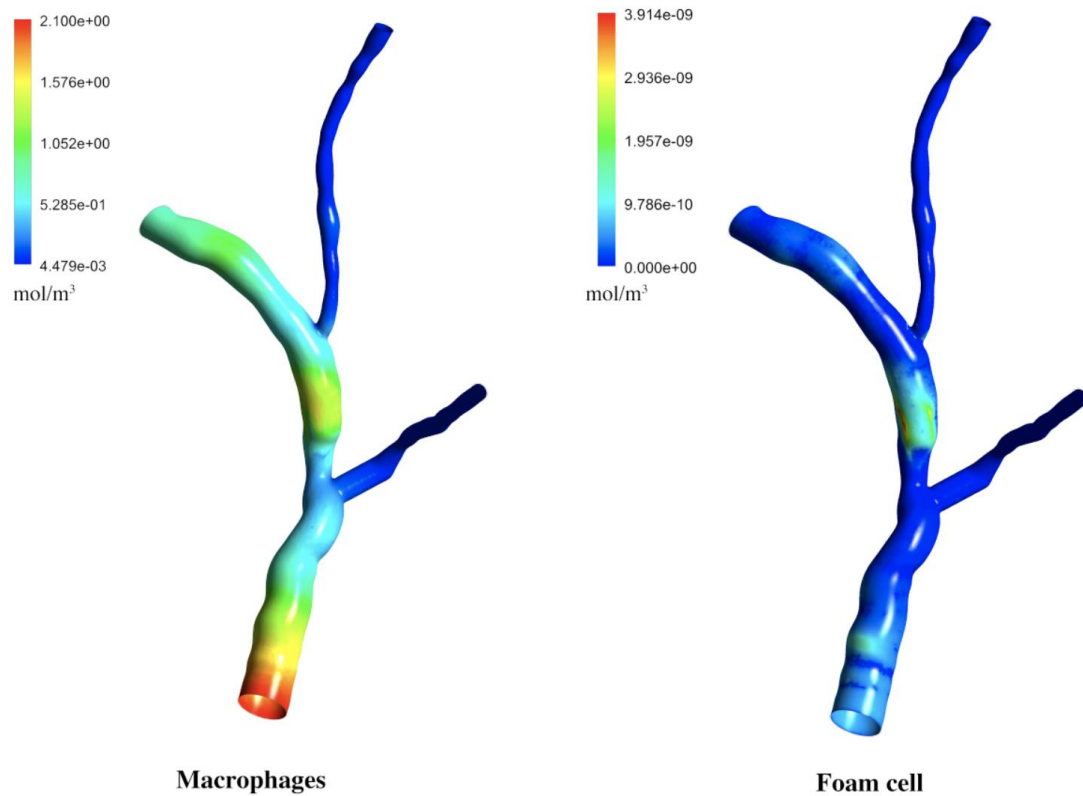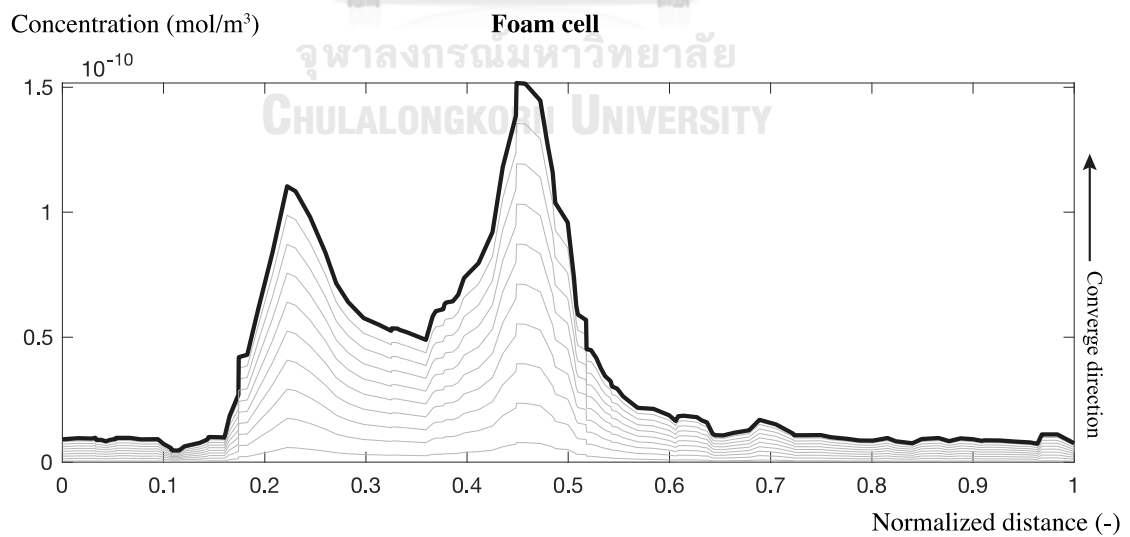

Figure 6.13 *Period-average foam cell concentration along the length-normalized distance on the endothelium interface*

Foam cells were formed according to the model given in Eq. 6.20. The foam cell formally were fat-laden macrophages which filled with LDL [105]. The transport equation of foam cell only involved the source term which did not have neither convection nor diffusion terms. Numerically, in order for the foam cell to form, the oxidized LDL and macrophages must be presented at the same site. The results showed promising prediction of location where the foam cell might form. Figure 6.12 showed significant build-up of the foam cell at the site where the flow structure was disturbed by the recirculation. The period-average concentration profile of foam cell is shown in Figure 6.13. The bottom line represented the period-average foam cell concentration of the first flow period. It was nearly flat at the early period then the profiles gradually increased proportionally. This suggested that the foam cell will continuously grow with the persistent permeation of incoming LDL and monocytes.

Conclusion

The improvement of three-zone artery model was proposed to investigate the atherosclerosis plaque formation in its initial stage (also known as fatty streak formation). The model was successfully developed and demonstrated that the model could be successfully implemented to the patient-specific coronary artery. The three-zone artery model including lumen zone, endothelium zone, and intima zone was well represented platform for future numerical investigation of the plaque formation which including the following features:

- The transportations of the LDL and monocytes from lumen into artery wall through the endothelium layer of the artery was controlled with three-pore model originated from Olgac et al [20].
- The shear-rate depended viscosity model, Carreau's model, was utilized to represent blood viscosity.
- Pulsatile periodic inflow waveform with period-average model for steady-equivalent was used to study the long time-scale investigation.
- The arterial wall was considered as porous zone which regulated by Darcy's law.

- LDL, oxidized LDL, monocyte, macrophages, and foam cell were the species included in the model for initial stage of plaque development

- The LDL concentration was elevated as the accumulation progress over time. Foam cells which was the critical cause of this phenomena were also significantly buildup as it was the deposition of the excessive cholesterol which was formed according to the oxidized LDL, monocyte, and macrophage.

The modeling of the biochemical interactions that included the transfer of the LDL, oxidized LDL, monocytes, macrophages, and foam cells provided the insight of where and how the foam cells were aggregated due to blood flow disturbances. Despite this, there are still many segments of the mathematical model that can be improved. The arterial wall needs to be fully coupled with the fluid flow structure in order to make arterial wall flexible. The variation in arterial wall thickness also needs to be included as its plays important roles in the permeability of the endothelial. This will result in a comprehensive integrated model of atherosclerotic plaque formation.

CHAPTER VII
CONCLUSION

In the present research study, the computational fluid dynamics of fluid transport and deposition of particle under unsteady flow in human fluid system was investigated. The study utilized the CFD techniques to simulate and visualize the behavior of the fluid flow in both human respiratory system and human recirculating system. This chapter summarized the novel findings of the study in all parts and also included the recommendations for future studies. The studies of the human respiratory system were divided into 2 parts which represented in Chapter III and Chapter IV:

Part I: Computational fluid dynamics simulation of full breathing cycle for aerosol deposition in trachea: Effect of breathing frequency.

Part II: The statistical study of the effect of aerosol properties on the deposition in idealized trachea.

Part I: The effect of breathing frequency on aerosol deposition

In this part, the computational fluid dynamics model of patient-specific trachea derived from computed tomography scan was developed. The model was based on Euler-Euler approach and included the electrostatic model for better representation of the segregation and agglomeration of the inhaled aerosol particles. The study was conducted in three different breathing frequencies, 10, 15 and 20 BPM, respectively. The simulation was done in complete breathing cycle including inhalation phase and exhalation phase. The result suggested that the agglomeration behavior of the aerosol was affected by the breathing frequency. While the flow patterns of each breathing frequency were similar, the high frequency with shorter flow time had the maximum deposition of particle at the upper part of the trachea. In opposite, the low frequency with longer flow time, the particle had time to flow further to the deeper location of the trachea. To observe the deposition region of the aerosol, the WSS, OFVI, granular temperature, and skin friction were introduced to indicate the deposition trend.

Part II: The effect of aerosol properties on the aerosol escaped percentage and the aerosol deposition percentage.

The statistical study of aerosol properties was investigated using the results from the Euler-Lagrangien CFD model. The particle trajectories were tracked from the beginning of G0 of respiratory tree until they collided to the wall or left the considered domain at the G4. The trachea model was reconstructed from idealized Weibel model. The effect of aerosol properties (aerosol diameter, aerosol density, and aerosol shape) on the escaped aerosol percentage and the aerosol deposition percentage were statistically studied using 3k factorial experimental design method. The analysis of variances suggested that aerosol diameter, aerosol density, aerosol sphericity, the interaction between aerosol diameter and aerosol density, the interaction between aerosol diameter and aerosol sphericity, and the quadratic effect of the aerosol diameter were identified as the factors affecting the escaped aerosol percentage and deposition percentage. The high aerosol escaped percentages implied that the particles were able to penetrate deeper to the generation after G4. The aerosol diameter and aerosol density had negative effect on the escaped aerosol percentage while the aerosol sphericity had positive effect. Within the range of study, the escaped particle percentage was lowest when both aerosol diameter and aerosol density were high and low sphericity which correlated with the force due to gravity resulting in low escaped aerosol percentage. For the deposition percentage, both aerosol diameter and aerosol density had positive effect on the particle deposition percentage while the aerosol sphericity had negative effect.

The cardiovascular system study was presented in Chapter V and Chapter VI. The blood transport with biochemical species was modeled. The studies of this section were divided into 2 parts:

Part III: Effect of transport parameters on atherosclerotic lesion growth: statistical experimental design analysis.

Part IV: Biochemical interaction the early stage formation of atherosclerotic lesion in arterial wall.

Part III: Effect of transport parameters on atherosclerotic lesion growth

The effect of transport parameters on the atherosclerotic lesion growth was investigated in axisymmetric coronary artery model. The computational fluid dynamics model was developed, and the three-zone artery model was proposed to represent the flow in arterial wall. The three-zone model was split into 3 represented zones, the lumen zone, the endothelium zone, and the intima zone. The model was successfully implemented in ANSYS Fluent. To ensure the validity of the model, it was compared and validated with Olgac el al [20]. The model was then used to simulate the results for the statistical analysis of the transport parameters. Five typical blood factors included in this study were blood density, blood viscosity, plasma density, plasma viscosity, and LDL concentration level. The 2^k factorial experimental design method was utilized. Blood viscosity and LDL concentration level were identified as influential blood factors affecting the atherosclerotic lesion growth. The LDL coverage area on the endothelium interface was strongly depended on blood viscosity.

Part IV: The early stage formation of atherosclerotic lesion in arterial wall

The three-zone artery model was improved to take into account for the biochemical interaction of the initial stage of atherosclerotic lesion formation. The three-dimensional patient-specific coronary artery was successfully implemented. The modeling of the biochemical interactions that included the transfer of the LDL, oxidized LDL, monocytes, macrophages, and foam cells were included in the model. The transport of the species was governed by three-pore model. The Carreau's model was utilized to represent blood viscosity which depended in the localized shear-rate. The period-average model was introduced in the study to represent the steady-equivalent result of the long time-scale study. The outcome of the model was able to predict the elevation of LDL concentration in the arterial wall as the accumulation progress over time. Foam cells were significantly buildup which was formed according to the oxidized LDL, monocyte, and macrophage. The simulation was giving the insight of where the form cells were aggregated due to the flow disturbances in coronary artery of mild stenosed patient.

Research outcome and novel contribution

- The following indices, WSS, OFVI, granular temperature, skin friction coefficient can be implemented into the mathematical model to use as a preliminary prediction of the aerosol deposition location.

- The understanding of the effect of aerosol properties is served as a guideline for the aerosol drug design industries. The identified factors can provide valuable guidance to the pharmacist to increase an efficiency of the aerosol drug design in targeted treatment specified to the patient as a part of precision medicine.

- The three-zone model was proposed to represent the species transport in arterial wall which will serve as a platform for the investigation of atherosclerotic lesion growth.

- The identified influential factors can provide beneficial advices for medical treatment to lower the risk of having atherosclerotic lesion.

Recommendations for future studies

- The study was mostly investigated using idealized model in Part I and Part III. For better representation of the flow behavior, the three-dimensional patient-specific model is suggested.

- The additional forces and interaction models can be added to the model in Part II to represent real world phenomena.

- The additional species transport must be included for quantitively prediction of the model in Part III and Part IV.

- The arterial wall needs to be fully coupled with the fluid flow structure in order to make arterial wall flexible.

- The variation in arterial wall thickness also needs to be included to represent the permeability of the endothelial cell.

REFERENCES

[1]   N.R. Labiris, M.B. Dolovich, Pulmonary drug delivery. Part I: physiological factors affecting therapeutic effectiveness of aerosolized medications., Br. J. Clin. Pharmacol. (2003).

[2]   A.H.L. Chow, H.H.Y. Tong, P. Chattopadhyay, B.Y. Shekunov, Particle engineering for pulmonary drug delivery, Pharm. Res. (2007). doi:10.1007/s11095-006-9174-3.

[3]   R.G. Rokkam, R.O. Fox, M.E. Muhle, Computational fluid dynamics and electrostatic modeling of polymerization fluidized-bed reactors, Powder Technol. (2010). doi:10.1016/j.powtec.2010.04.002.

[4]   R.B. Bird, W.E. Stewart, E.N. Lightfoot, Transport phenomena, second edition, 2012. doi:10.1002/aic.690070245.

[5]   G.K. Batchelor, An Introduction to Fluid Dynamics, 2000. doi:10.1017/CBO9780511800955.

[6]   I. SAS IP, Wall Boundaries, (n.d.). https://www.sharcnet.ca/Software/Ansys/16.2.3/en-us/help/cfx_mod/i1308399.html (accessed May 26, 2019).

[7]   K. Tamm, C. J. F. Böttcher and P. Bordewijk: Theory of Electric Polarization, Vol. II: Dielectrics in time-dependent fields. Verlag Elsevier, Amsterdam, Oxford, New York 1978. 561 Seiten, Preis: US $ 121,50, Dfl. 292,-., Berichte Der Bunsengesellschaft Für Phys. Chemie. (2012). doi:10.1002/bbpc.19800841128.

[8]   C. Chen, Q. Dai, H. Qi, Improvement of EMMS drag model for heterogeneous gas-solid flows based on cluster modeling, Chem. Eng. Sci. (2016). doi:10.1016/j.ces.2015.10.025.

[9]   W. Wei, S. wei Huang, L. hua Chen, Y. Qi, Y. min Qiu, S. tong Li, Airflow behavior changes in upper airway caused by different head and neck positions: Comparison by computational fluid dynamics, J. Biomech. (2017). doi:10.1016/j.jbiomech.2016.12.032.

[10]   A. Naseri, S. Shaghaghian, O. Abouali, G. Ahmadi, Numerical investigation of transient transport and deposition of microparticles under unsteady inspiratory flow in human upper airways, Respir. Physiol. Neurobiol. (2017). doi:10.1016/j.resp.2017.06.005.

[11]   A. Kerekes, M. Veres, L. Himics, S. Tóth, A. Czitrovszky, D. Oszetzky, A. Horváth, S. Kugler, M. Koós, A. Nagy, Determination of the deposited amount of inhalation drugs in realistic human airways by Raman and infrared spectroscopy, Meas. J. Int. Meas. Confed. (2017). doi:10.1016/j.measurement.2017.03.029.

[12]   P.G. Koullapis, S.C. Kassinos, M.P. Bivolarova, A.K. Melikov, Particle deposition in a realistic geometry of the human conducting airways: Effects of inlet velocity profile, inhalation flowrate and electrostatic charge, J. Biomech. (2016).

doi:10.1016/j.jbiomech.2015.11.029.

[13]   A.F. Miguel, Penetration of inhaled aerosols in the bronchial tree, Med. Eng. Phys. (2017). doi:10.1016/j.medengphy.2017.03.004.

[14]   N.L. Phuong, K. Ito, Investigation of flow pattern in upper human airway including oral and nasal inhalation by PIV and CFD, Build. Environ. (2015). doi:10.1016/j.buildenv.2015.10.002.

[15]   O. Pourmehran, M. Rahimi-Gorji, M. Gorji-Bandpy, T.B. Gorji, Simulation of magnetic drug targeting through tracheobronchial airways in the presence of an external non-uniform magnetic field using Lagrangian magnetic particle tracking, J. Magn. Magn. Mater. (2015). doi:10.1016/j.jmmm.2015.05.086.

[16]   M. Rahiminejad, A. Haghighi, A. Dastan, O. Abouali, M. Farid, G. Ahmadi, Computer simulations of pressure and velocity fields in a human upper airway during sneezing, Comput. Biol. Med. (2016). doi:10.1016/j.compbiomed.2016.01.022.

[17]   K.A. Ahmad, M. Zubair, M.Z. Abdullah, R. Ismail, I.L. Shuaib, S. Abdul Hamid, Review: A critical overview of limitations CFD Modeling in nasal airflow., J. Med. Biol. Eng. (2012).

[18]   X.Y. Xu, S.J. Ni, M. Fu, X. Zheng, N. Luo, W.G. Weng, Numerical investigation of airflow, heat transfer and particle deposition for oral breathing in a realistic human upper airway model, J. Therm. Biol. (2017). doi:10.1016/j.jtherbio.2017.05.003.

[19]   J. Huang, R.W. Lyczkowski, D. Gidaspow, Pulsatile flow in a coronary artery using multiphase kinetic theory, J. Biomech. (2009). doi:10.1016/j.jbiomech.2009.01.038.

[20]   U. Olgac, Computational modeling of coupled blood-wall mass transport of LDL: effects of local wall shear stress., Am. J. Physiol. Heart Circ. Physiol. (2008). doi:10.1152/ajpheart.01082.2007.

[21]   G. Di Tomaso, V. Daz-Zuccarini, C. Pichardo-Almarza, A multiscale model of atherosclerotic plaque formation at its early stage, IEEE Trans. Biomed. Eng. (2011). doi:10.1109/TBME.2011.2165066.

[22]   N. Yang, K. Vafai, Modeling of low-density lipoprotein (LDL) transport in the artery-effects of hypertension, Int. J. Heat Mass Transf. (2006). doi:10.1016/j.ijheatmasstransfer.2005.09.019.

[23]   S. Kenjereš, A. De Loor, Modelling and simulation of low-density lipoprotein transport through multi-layered wall of an anatomically realistic carotid artery bifurcation, J. R. Soc. Interface. 11 (2014) 20130941. doi:10.1098/rsif.2013.0941.

[24]   S.A. Gabriel, Y. Ding, Y. Feng, Quantifying the influence of oscillatory flow disturbances on blood flow, J. Theor. Biol. (2017). doi:10.1016/j.jtbi.2017.07.008.

[25]   S.A. Gabriel, Y. Ding, Y. Feng, J.A. Gear, Comparative analysis of pulsatile and steady flow on arterial mass transport, in: 19th Australas. Fluid Mech. Conf., 2014.

[26] S.A. Gabriel, Y. Ding, Y. Feng, Modelling the period-average transport of species within pulsatile blood flow, J. Theor. Biol. (2018). doi:10.1016/j.jtbi.2018.07.006.

[27] A.B. Ozturk, E. Damadoglu, G. Karakaya, A.F. Kalyoncu, Does nasal hair (Vibrissae) density affect the risk of developing asthma in patients with seasonal rhinitis?, Int. Arch. Allergy Immunol. (2011). doi:10.1159/000321912.

[28] M. Goldberg, A Systematic Review of the Relation Between Long-term Exposure to Ambient Air Pollution and Chronic Diseases, Rev. Environ. Health. (2011). doi:10.1515/reveh.2008.23.4.243.

[29] M. Rahimi-Gorji, O. Pourmehran, M. Gorji-Bandpy, T.B. Gorji, CFD simulation of airflow behavior and particle transport and deposition in different breathing conditions through the realistic model of human airways, J. Mol. Liq. (2015). doi:10.1016/j.molliq.2015.05.031.

[30] X. Chen, W. Zhong, X. Zhou, B. Jin, B. Sun, CFD-DEM simulation of particle transport and deposition in pulmonary airway, Powder Technol. (2012). doi:10.1016/j.powtec.2012.05.041.

[31] X. Chen, Y. Feng, W. Zhong, B. Sun, F. Tao, Numerical investigation of particle deposition in a triple bifurcation airway due to gravitational sedimentation and inertial impaction, Powder Technol. (2018). doi:10.1016/j.powtec.2017.09.050.

[32] P.R. Byron, M. Hindle, C.F. Lange, P.W. Longest, D. McRobbie, M.J. Oldham, B. Olsson, C.G. Thiel, H. Wachtel, W.H. Finlay, In Vivo–In Vitro Correlations: Predicting Pulmonary Drug Deposition from Pharmaceutical Aerosols , J. Aerosol Med. Pulm. Drug Deliv. (2010). doi:10.1089/jamp.2010.0846.

[33] Y.S. Cheng, Mechanisms of Pharmaceutical Aerosol Deposition in the Respiratory Tract, AAPS PharmSciTech. (2014). doi:10.1208/s12249-014-0092-0.

[34] J. Wong, H.K. Chan, P.C.L. Kwok, Electrostatics in pharmaceutical aerosols for inhalation, Ther. Deliv. (2013). doi:10.4155/tde.13.70.

[35] K.E. Barrett, H.L. Brooks, S. Boitano, S.M. Barman, Ganong's Review of Medical Physiology, 2010.

[36] L. Warliah, A.S. Rohman, P.H. Rusmin, Model Development of Air Volume and Breathing Frequency in Human Respiratory System Simulation, Procedia - Soc. Behav. Sci. (2013). doi:10.1016/j.sbspro.2012.11.328.

[37] L.L.X. Augusto, G.C. Lopes, J.A.S. Gonçalves, A cfd study of deposition of pharmaceutical aerosols under different respiratory conditions, Brazilian J. Chem. Eng. (2016). doi:10.1590/0104-6632.20160333s20150100.

[38] N. V. Brilliantov, T. Pöschel, N. V. Brilliantov, T. Pöschel, Kinetic Coefficients for Granular Gases of Viscoelastic Particles, in: Kinet. Theory Granul. Gases, 2010. doi:10.1093/acprof:oso/9780198530381.003.0021.

[39] Y. Imai, T. Miki, T. Ishikawa, T. Aoki, T. Yamaguchi, Deposition of micrometer particles in pulmonary airways during inhalation and breath holding, J. Biomech. (2012). doi:10.1016/j.jbiomech.2012.04.017.

[40] L.T. Holbrook, P.W. Longest, Validating CFD predictions of highly localized aerosol deposition in airway models: In vitro data and effects of surface properties, J. Aerosol Sci. (2013). doi:10.1016/j.jaerosci.2013.01.008.

[41] D. Gidaspow, J. Huang, Kinetic theory based model for blood flow and its viscosity, Ann. Biomed. Eng. (2009). doi:10.1007/s10439-009-9720-3.

[42] A. Jaworek, A. Marchewicz, A.T. Sobczyk, A. Krupa, T. Czech, Two-stage electrostatic precipitators for the reduction of PM2.5 particle emission, Prog. Energy Combust. Sci. (2018). doi:10.1016/j.pecs.2018.03.003.

[43] R.G. Rokkam, A. Sowinski, R.O. Fox, P. Mehrani, M.E. Muhle, Computational and experimental study of electrostatics in gas-solid polymerization fluidized beds, Chem. Eng. Sci. (2013). doi:10.1016/j.ces.2013.01.023.

[44] D.A.G. Bruggeman, Berechnung verschiedener physikalischer Konstanten von heterogenen Substanzen. I. Dielektrizitätskonstanten und Leitfähigkeiten der Mischkörper aus isotropen Substanzen, Ann. Phys. (1935). doi:10.1002/andp.19354160705.

[45] E. Aasgrav, S.G. Johnsen, A.J. Simonsen, B. Müller, CFD simulations of turbulent flow in the human upper airways, ArXiv Prepr. ArXiv1706.02565. (2017).

[46] L.T. Choi, J.Y. Tu, H.F. Li, F. Thien, Flow and particle deposition patterns in a realistic human double bifurcation airway model, Inhal. Toxicol. (2007). doi:10.1080/08958370601051719.

[47] Q. Deng, C. Ou, J. Chen, Y. Xiang, Particle deposition in tracheobronchial airways of an infant, child and adult, Sci. Total Environ. (2018). doi:10.1016/j.scitotenv.2017.08.240.

[48] B. Soni, S. Aliabadi, Large-scale CFD simulations of airflow and particle deposition in lung airway, Comput. Fluids. (2013). doi:10.1016/j.compfluid.2013.06.015.

[49] B. Sul, A. Wallqvist, M.J. Morris, J. Reifman, V. Rakesh, A computational study of the respiratory airflow characteristics in normal and obstructed human airways, Comput. Biol. Med. (2014). doi:10.1016/j.compbiomed.2014.06.008.

[50] S. Khonsary, Guyton and Hall: Textbook of Medical Physiology, Surg. Neurol. Int. (2017). doi:10.4103/sni.sni_327_17.

[51] S.W. Clarke, Editorial : Therapeutic aerosols 1-Physical and practical considerations, Thorax. (1983). doi:10.1136/thx.38.12.881.

[52] A. Moskal, T.R. Sosnowski, Computational fluid dynamics (CFD) and direct visualization studies of aerosol release from two cyclohaler-type dry powder inhalers, J. Drug Deliv. Sci. Technol. (2012). doi:10.1016/S1773-2247(12)50021-3.

[53] P.C.L. Kwok, W. Glover, H.K. Chan, Electrostatic charge characteristics of aerosols produced from metered dose inhalers, J. Pharm. Sci. (2005). doi:10.1002/jps.20395.

[54] D. Katritsis, L. Kaiktsis, A. Chaniotis, J. Pantos, E.P. Efstathopoulos, V. Marmarelis, Wall Shear Stress: Theoretical Considerations and Methods of Measurement, Prog. Cardiovasc. Dis. (2007). doi:10.1016/j.pcad.2006.11.001.

[55] P.A. Clingan, M.H. Friedman, The Effect of Celiac and Renal Artery Outflows on Near-Wall Velocities in the Porcine Iliac Arteries, Ann. Biomed. Eng. (2000). doi:10.1114/1.269.

[56] K. Kadota, A. Imanaka, M. Shimazaki, T. Takemiya, K. Kubo, H. Uchiyama, Y. Tozuka, Effects of inhalation procedure on particle behavior and deposition in the airways analyzed by numerical simulation, J. Taiwan Inst. Chem. Eng. (2018). doi:10.1016/j.jtice.2017.11.008.

[57] B. Ma, K.R. Lutchen, CFD simulation of aerosol deposition in an anatomically based human large-medium airway model, Ann. Biomed. Eng. (2009). doi:10.1007/s10439-008-9620-y.

[58] J. Xi, X. Si, W. Longest, Electrostatic charge effects on pharmaceutical aerosol deposition in human nasal-laryngeal airways, Pharmaceutics. (2014). doi:10.3390/pharmaceutics6010026.

[59] M. Ali, R.N. Reddy, M.K. Mazumder, Electrostatic charge effect on respirable aerosol particle deposition in a cadaver based throat cast replica, J. Electrostat. (2008). doi:10.1016/j.elstat.2008.02.005.

[60] B. Chalermsinsuwan, D. Gidaspow, P. Piumsomboon, Two- and three-dimensional CFD modeling of Geldart A particles in a thin bubbling fluidized bed: Comparison of turbulence and dispersion coefficients, Chem. Eng. J. (2011). doi:10.1016/j.cej.2011.04.007.

[61] W. Polashenski, J.C. Chen, Measurement of particle phase stresses in fast fluidized beds, Ind. Eng. Chem. Res. (1999). doi:10.1021/ie980354n.

[62] A. Miller, D. Gidaspow, Dense, vertical gas-solid flow in a pipe, AIChE J. (1992). doi:10.1002/aic.690381111.

[63] D. Gidaspow, R. Mostofi, Maximum carrying capacity and granular temperature of A, B and C particles, AIChE J. (2003). doi:10.1002/aic.690490404.

[64] J.S. Patton, P.R. Byron, Inhaling medicines: Delivering drugs to the body through the lungs, Nat. Rev. Drug Discov. (2007). doi:10.1038/nrd2153.

[65] E.R. Weibel, Chapter VI - Geometry and Dimensions of Airways of the Respiratory Zone, in: E.R.B.T.-M. of the H.L. Weibel (Ed.), Academic Press, 1963: pp. 56–73. doi:https://doi.org/10.1016/B978-1-4832-0076-7.50011-9.

[66] S. Ren, M. Cai, Y. Shi, W. Xu, X.D. Zhang, Influence of bronchial diameter change on the airflow dynamics based on a pressure-controlled ventilation system, Int. j. Numer. Method. Biomed. Eng. (2018). doi:10.1002/cnm.2929.

[67] D. Lloyd-Jones, R. Adams, M. Carnethon, G. De Simone, T.B. Ferguson, K. Flegal, E. Ford, K. Furie, A. Go, K. Greenlund, N. Haase, S. Hailpern, M. Ho, V. Howard, B. Kissela, S. Kittner, D. Lackland, L. Lisabeth, A. Marelli, M. McDermott, J. Meigs, D. Mozaffarian, G. Nichol, C. O'Donnell, V. Roger, W.

Rosamond, R. Sacco, P. Sorlie, R. Stafford, J. Steinberger, T. Thom, S. Wasserthiel-Smoller, N. Wong, J. Wylie-Rosett, Y. Hong, Heart Disease and Stroke Statistics—2009 Update, Circulation. 119 (2009). doi:10.1161/circulationaha.108.191259.

[68] et al. Go AS, Mozaffarian D, Roger VL, Heart Disease and Stroke Statistics—2014 Update, Circulation. (2014). doi:10.1161/CIR.0000000000000350.

[69] E.J. Benjamin, S.S. Virani, C.W. Callaway, A.M. Chamberlain, A.R. Chang, S. Cheng, S.E. Chiuve, M. Cushman, F.N. Delling, R. Deo, S.D. de Ferranti, J.F. Ferguson, M. Fornage, C. Gillespie, C.R. Isasi, M.C. Jiménez, L.C. Jordan, S.E. Judd, D. Lackland, J.H. Lichtman, L. Lisabeth, S. Liu, C.T. Longenecker, P.L. Lutsey, J.S. Mackey, D.B. Matchar, K. Matsushita, M.E. Mussolino, K. Nasir, M. O'Flaherty, L.P. Palaniappan, A. Pandey, D.K. Pandey, M.J. Reeves, M.D. Ritchey, C.J. Rodriguez, G.A. Roth, W.D. Rosamond, U.K.A. Sampson, G.M. Satou, S.H. Shah, N.L. Spartano, D.L. Tirschwell, C.W. Tsao, J.H. Voeks, J.Z. Willey, J.T. Wilkins, J.H.Y. Wu, H.M. Alger, S.S. Wong, P. Muntner, Heart Disease and Stroke Statistics—2018 Update: A Report From the American Heart Association, Circulation. 137 (2018). doi:10.1161/CIR.0000000000000558.

[70] P. Libby, Inflammation in atherosclerosis, Nature. 32 (2002) 2045–2051. doi:10.1161/ATVBAHA.108.179705.

[71] W.B. Kannel, Overview of atherosclerosis, Clin. Ther. 20 (1998) B2–B17. doi:10.1016/S0149-2918(98)80027-1.

[72] M. Cilla, E. Pena, M.A. Martinez, E. Peña, M.A. Martínez, Mathematical modelling of atheroma plaque formation and development in coronary arteries, J. R. Soc. Interface. 11 (2014) 20130866–20130866. doi:10.1098/rsif.2013.0866.

[73] S. Chung, K. Vafai, Effect of the fluid-structure interactions on low-density lipoprotein transport within a multi-layered arterial wall, J. Biomech. 45 (2012) 371–381. doi:10.1016/j.jbiomech.2011.10.002.

[74] F. Gijsen, A. van der Giessen, A. van der Steen, J. Wentzel, Shear stress and advanced atherosclerosis in human coronary arteries, J. Biomech. 46 (2013) 240–247. doi:10.1016/j.jbiomech.2012.11.006.

[75] A.M. Malek, S.L. Alper, S. Izumo, Hemodynamic Shear Stress and Its Role in Atherosclerosis, J. Am. Med. Assoc. 282 (1999) 2035. doi:10.1001/jama.282.21.2035.

[76] S. Chien, Effects of disturbed flow on endothelial cells, Ann. Biomed. Eng. 36 (2008) 554–562. doi:10.1007/s10439-007-9426-3.

[77] P.W.F.F. Wilson, R.B. D'Agostino, D. Levy, A.M. Belanger, H.H.H. Silbershatz, W.B. Kannel, R.B. D'Agostino, D. Levy, A.M. Belanger, H.H.H. Silbershatz, W.B. Kannel, Prediction of coronary heart disease using risk factor categories, Circulation. 97 (1998) 1837–1847. doi:10.1161/01.CIR.97.18.1837.

[78] T.G.W. Speel, I. Bleumer, W.L. Diemont, M.C. Van der Maas, H. Wijkstra, E.J. Meuleman, Effect of fluid shear stress on the permeability of the arterial

endothelium, Ann. Biomed. Eng. (2002). doi:10.1114/1.1467924.

[79] H.W. Sill, Y.S. Chang, J.R. Artman, J.A. Frangos, T.M. Hollis, J.M. Tarbell, Shear stress increases hydraulic conductivity of cultured endothelial monolayers., Am. J. Physiol. 268 (1995) H535–H543. doi:10.1152/ajpheart.1995.268.2.H535.

[80] N. Sun, N.B. Wood, A.D. Hughes, S.A.M. Thom, X. Yun Xu, Effects of transmural pressure and wall shear stress on LDL accumulation in the arterial wall: a numerical study using a multilayered model, AJP Hear. Circ. Physiol. (2007). doi:10.1152/ajpheart.01281.2006.

[81] M. Prosi, P. Zunino, K. Perktold, A. Quarteroni, Mathematical and numerical models for transfer of low-density lipoproteins through the arterial walls: A new methodology for the model set up with applications to the study of disturbed lumenal flow, J. Biomech. (2005). doi:10.1016/j.jbiomech.2004.04.024.

[82] F. Yuan, S. Chien, S. Weinbaum, A New View of Convective-Diffusive Transport Processes in the Arterial Intima, J. Biomech. Eng. (1991). doi:10.1115/1.2894890.

[83] C.B. Vargas, F.F. Vargas, J.G. Pribyl, P.L. Blackshear, Hydraulic conductivity of the endothelial and outer layers of the rabbit aorta, Am J Physiol. (1979). doi:10.1152/ajpheart.1979.236.1.h53.

[84] A. Tedgui, M.J. Lever, Filtration through damaged and undamaged rabbit thoracic aorta, Am. J. Physiol. (2017). doi:10.1152/ajpheart.1984.247.5.H784.

[85] S. Iliceto, V. Marangelli, C. Memmola, P. Rizzon, Transesophageal Doppler echocardiography evaluation of coronary blood flow velocity in baseline conditions and during dipyridamole-induced coronary vasodilation, Circulation. (1991). doi:10.1161/01.CIR.83.1.61.

[86] D.C. Montgomery, Design and Analysis of Experiments, 2012. doi:10.1198/tech.2006.s372.

[87] J. Antony, Design of Experiments for Engineers and Scientists, 2014. doi:10.1016/B978-0-7506-4709-0.X5000-5.

[88] U. Olgac, D. Poulikakos, S.C. Saur, H. Alkadhi, V. Kurtcuoglu, Patient-specific three-dimensional simulation of LDL accumulation in a human left coronary artery in its healthy and atherosclerotic states, AJP Hear. Circ. Physiol. (2009). doi:10.1152/ajpheart.01182.2008.

[89] U. Olgac, J. Knight, D. Poulikakos, S.C. Saur, H. Alkadhi, L.M. Desbiolles, P.C. Cattin, V. Kurtcuoglu, Computed high concentrations of low-density lipoprotein correlate with plaque locations in human coronary arteries, J. Biomech. (2011). doi:10.1016/j.jbiomech.2011.06.022.

[90] Ö. Smedby, Do plaques grow upstream or downstream?: An angiographic study in the femoral artery, Arterioscler. Thromb. Vasc. Biol. (1997). doi:10.1161/01.ATV.17.5.912.

[91] M.F. Linton, P.G. Yancey, S.S. Davies, W.G. Jerome, E.F. Linton, K.C. Vickers, The role of lipids and lipoproteins in atherosclerosis, 2015. doi:15403115.

[92] N. Sakamoto, T. Ohashi, M. Sato, Effect of shear stress on permeability of vascular endothelial monolayer cocultured with smooth muscle cells, JSME Int. J. Ser. C Mech. Syst. Mach. Elem. Manuf. 47 (2004) 992–999.

[93] S.L. Waters, J. Alastruey, D.A. Beard, P.H.M. Bovendeerd, P.F. Davies, G. Jayaraman, O.E. Jensen, J. Lee, K.H. Parker, A.S. Popel, T.W. Secomb, M. Siebes, S.J. Sherwin, R.J. Shipley, N.P. Smith, F.N. van de Vosse, Theoretical models for coronary vascular biomechanics: Progress & challenges, Prog. Biophys. Mol. Biol. (2011). doi:10.1016/j.pbiomolbio.2010.10.001.

[94] C.C. O'Brien, V.B. Kolachalama, T.J. Barber, A. Simmons, E.R. Edelman, Impact of flow pulsatility on arterial drug distribution in stent-based therapy, J. Control. Release. (2013). doi:10.1016/j.jconrel.2013.03.014.

[95] N. Sun, N.B. Wood, A.D. Hughes, S.A.M. Thom, X.Y. Xu, Influence of pulsatile flow on LDL transport in the arterial wall, Ann. Biomed. Eng. (2007). doi:10.1007/s10439-007-9347-1.

[96] X. Liu, Y. Fan, X. Deng, F. Zhan, Effect of non-Newtonian and pulsatile blood flow on mass transport in the human aorta, J. Biomech. (2011). doi:10.1016/j.jbiomech.2011.01.024.

[97] A.D. Caballero, S. Laín, Numerical simulation of non-Newtonian blood flow dynamics in human thoracic aorta, Comput. Methods Biomech. Biomed. Engin. (2015). doi:10.1080/10255842.2014.887698.

[98] S.S. Dhawan, R.P.A. Nanjundappa, J.R. Branch, W.R. Taylor, A.A. Quyyumi, H. Jo, M.C. McDaniel, J. Suo, D. Giddens, H. Samady, Shear stress and plaque development, Expert Rev. Cardiovasc. Ther. (2010). doi:10.1586/erc.10.28.

[99] J.J. Wentzel, Y.S. Chatzizisis, F.J.H. Gijsen, G.D. Giannoglou, C.L. Feldman, P.H. Stone, Endothelial shear stress in the evolution of coronary atherosclerotic plaque and vascular remodelling: Current understanding and remaining questions, Cardiovasc. Res. (2012). doi:10.1093/cvr/cvs217.

[100] E. Cecchi, C. Giglioli, S. Valente, C. Lazzeri, G.F. Gensini, R. Abbate, L. Mannini, Role of hemodynamic shear stress in cardiovascular disease, Atherosclerosis. (2011). doi:10.1016/j.atherosclerosis.2010.09.008.

[101] J.-J. Chiu, S. Chien, Effects of Disturbed Flow on Vascular Endothelium: Pathophysiological Basis and Clinical Perspectives, Physiol. Rev. (2011). doi:10.1152/physrev.00047.2009.

[102] P.F. Davies, Hemodynamic shear stress and the endothelium in cardiovascular pathophysiology, Nat. Clin. Pract. Cardiovasc. Med. (2009). doi:10.1038/ncpcardio1397.

[103] S. Weinbaum, G. Tzeghai, P. Ganatos, R. Pfeffer, S. Chien, Effect of cell turnover and leaky junctions on arterial macromolecular transport., Am. J. Physiol. (1985). doi:10.1152/ajpheart.1985.248.6.H945.

[104] M.A.K. Bulelzai, J.L.A. Dubbeldam, Long time evolution of atherosclerotic plaques, J. Theor. Biol. (2012). doi:10.1016/j.jtbi.2011.11.023.

[105] A. Volobueva, D. Zhang, A. V. Grechko, A.N. Orekhov, Foam cell formation and cholesterol trafficking and metabolism disturbances in atherosclerosis, Cor Vasa. (2018). doi:10.1016/J.CRVASA.2018.06.006.

VITA

NAME   Ratchanon Piemjaiswang

DATE OF BIRTH   11 December 1991

PLACE OF BIRTH   Samut Prakan

INSTITUTIONS   Chulalongkorn University
ATTENDED   Silpakorn University

HOME ADDRESS   38 Tessaban 12 Rd. Paknam, Muang Samut Prakan 10270

PUBLICATION   Buasri, A., Buranasing, G., Piemjaiswang, R., Yousatit, S., & Loryuenyong, V. (2014). Effect of titanium dioxide nanoparticles on mechanical and thermal properties of poly (lactic acid) and poly (butylene succinate) blends. In Advances in Science and Technology (Vol. 96, pp. 33-38). Trans Tech Publications.

Piemjaiswang, R., Ratanathammapan, K., Kunchonthara, P., Piumsomboon, P., & Chalermsinsuwan, B. (2016). CFD study of cyclone performance: effect of inlet section angle and particle size distribution. Jurnal Teknologi, 78(6-4).

Jongartklang, N., Piemjaiswang, R., Piumsomboon, P., & Chalermsinsuwan, B. (2016). CO2 sorption using Na2CO3/Al2O3 sorbent with various flow patterns of fixed/fluidized bed reactors. Jurnal Teknologi, 78(6-4).

Piemjaiswang, R., Shiratori, S., Chaiwatanarat, T., Piumsomboon, P., & Chalermsinsuwan, B. (2019). Computational fluid dynamics simulation of full breathing cycle for aerosol deposition in trachea: Effect of breathing frequency. Journal of the Taiwan Institute of Chemical Engineers, 97, 66-79.

Tritippayanon, R., Piemjaiswang, R., Piumsomboon, P., & Chalermsinsuwan, B. (2019). Computational fluid dynamics of sulfur dioxide and carbon dioxide capture using mixed feeding of calcium carbonate/calcium oxide in an industrial scale circulating fluidized bed boiler. Applied Energy, 250, 493-502.